

Title	Enhanced shortcuts to adiabaticity
Authors	Whitty, Chris
Publication date	2022
Original Citation	Whitty, C. 2022. Enhanced shortcuts to adiabaticity. PhD Thesis, University College Cork.
Type of publication	Doctoral thesis
Rights	© 2022, Chris Whitty. - https://creativecommons.org/licenses/by-nc-nd/4.0/
Download date	2024-11-12 21:48:57
Item downloaded from	https://hdl.handle.net/10468/14470



UCC

University College Cork, Ireland
Coláiste na hOllscoile Corcaigh

UNIVERSITY COLLEGE CORK



Enhanced Shortcuts to Adiabaticity

Author:

Chris WHITTY

Supervisor:

Dr. Andreas RUSCHHAUPT

*A thesis submitted in partial fulfillment of the requirements
for the degree of Doctor of Philosophy*

Quantum Control via Shortcuts to Adiabaticity Group

Department of Physics

Head of Department:

Prof. John McInerney

2023

Declaration of Authorship

This is to certify that the work I am submitting is my own and has not been submitted for another degree, either at University College Cork or elsewhere. All external references and sources are clearly acknowledged and identified within the contents. I have read and understood the regulations of University College Cork concerning plagiarism and intellectual property.

Signed: *Chris Whitty*

Date: 18/12/2022

External Examiner: Prof. Daniel Alonso – University of La Laguna, Spain

Internal Examiner: Dr. Stefan Schulz – University College Cork, Ireland

Abstract

Dynamical control of quantum systems is a fundamental requirement for designing and engineering quantum technologies. Adiabatic control methods are used extensively to control quantum systems in many settings. However, adiabatic control methods require long operation times. To address this issue, a collection of techniques called “shortcuts to adiabaticity” (STA) have been developed. STA have been applied in many settings, and they can offer significant improvement over adiabatic schemes.

However, a major limitation of STA is that fully analytic STA schemes are known only for several specific families of quantum systems. Motivated to overcome this restriction, in this thesis we derive an analytic method called “enhanced shortcuts to adiabaticity” (eSTA) that extends STA techniques to systems that do not admit STA methods exactly. We first derive the eSTA formalism and demonstrate its utility in designing control schemes for several practical quantum control settings. We then investigate the robustness of eSTA against several types of systematic error and environmental noise, using the setting of neutral atom lattice transport. We also derive an alternative eSTA technique that naturally includes higher order terms, at the expense of further calculation. Both the alternative and original eSTA schemes are applied to fast anharmonic trap expansion. Finally, transport of two ions with Coulomb interaction in an anharmonic trap is considered and eSTA is shown to be robust against the effect of amplitude noise in this setting.

Acknowledgements

I would like to thank my supervisor Dr. Andreas Ruschhaupt for his patience, guidance, and unwavering support throughout my studies. His technical ability and deep understanding of the field was instrumental in every aspect of this thesis. This project would not have been possible without him.

I would also like to thank Dr. Anthony Kiely for his help and invaluable advice and suggestions throughout the duration of this project. I am grateful to the members of the Quantum Control via Shortcuts to Adiabaticity Group for their support and assistance; Dave, Jing, Manuel, Tom and Guido. I would like to thank Manuel, Jing and Tom for the many engaging conversations and culinary explorations we have enjoyed over lunch. I am very grateful to Dave for his proof reading and discerning commentary, and his unquenchable thirst for epistemological delights that he enthusiastically shares with the group over a scone and an array of home grown specialties.

List of Publications

- C. Whitty, A. Kiely and A. Ruschhaupt
Enhanced shortcuts to adiabaticity
Phys. Rev. Research 2, 023360 (2020)
- C. Whitty, A. Kiely and A. Ruschhaupt
Robustness of enhanced shortcuts to adiabaticity in lattice transport
Phys. Rev. A 105, 013311 (2022)
- C. Whitty, A. Kiely and A. Ruschhaupt
Improved anharmonic trap expansion through enhanced shortcuts to adiabaticity
J. Phys. B: At. Mol. Opt. Phys. (2022)

Contents

Declaration of Authorship	i
Abstract	ii
Acknowledgements	iii
List of Publications	iv
1 Introduction	1
2 Background Theory	5
2.1 The Adiabatic Theorem	5
2.2 Shortcuts to Adiabaticity	13
2.2.1 Counterdiabatic driving	15
2.2.2 The Streamlined Fast Forward approach	17
2.2.3 Invariant-based inverse engineering	22
Fast harmonic trap expansion using L.R. invariants	26
Fast harmonic trap transport via L.R. invariants	29
2-level population inversion using L.R. invariants	33
2.3 Numerical Methods	36
2.3.1 Operator splitting	37
2.3.2 Imaginary time evolution	40
2.3.3 The GRAPE algorithm	42
3 Quantum control via enhanced shortcuts to adiabaticity	46
3.1 Overview	46
3.2 Introduction	47
3.3 Formalism of eSTA	48
3.4 Population inversion without the Rotating-Wave-Approximation	53
3.5 Single Particle Transport	55
3.6 Transport of two ions including Coulomb interaction	57
3.7 Conclusion	59
3.8 Appendix	60

3.8.1	Approximation of $F(\mu, \vec{\lambda}_0)$	61
3.8.2	Approximation of $\nabla F(\mu, \vec{\lambda}_0)$	63
4	Robustness of eSTA in lattice transport	66
4.1	Overview	66
4.2	Introduction	67
4.3	eSTA Formalism	68
4.3.1	Construction of eSTA control scheme	69
4.3.2	Expected stabilities of eSTA and STA	72
4.4	Physical Model	73
4.4.1	STA control functions	74
4.4.2	Derivation of eSTA control functions	79
4.4.3	Fidelities for STA and eSTA schemes	81
4.5	eSTA Control Function Deviation	83
4.6	Robustness to Systematic Errors	86
4.6.1	Systematic Error Sensitivity	88
4.6.2	Systematic Error bound	91
4.7	Robustness of eSTA to noise	93
4.7.1	Position noise	95
4.7.2	Amplitude noise	96
4.8	Conclusion	98
4.9	Appendix	99
4.9.1	Derivation of \mathcal{C}_Q	99
4.9.2	Derivation of S_N	100
5	Improved anharmonic trap expansion through eSTA	103
5.1	Overview	103
5.2	Introduction	104
5.3	Generalised eSTA formalism	105
5.3.1	eSTA construction	106
5.3.2	Perturbative approximations for eSTA control	109
5.4	Anharmonic trap expansion	113
5.4.1	Trap potentials	113
5.4.2	STA system and eSTA parametrisation	114
5.4.3	Fidelity Results: Accordion Lattice Expansion	117
5.4.4	Fidelity Results: Gaussian Trap Expansion	118
5.4.5	ESTA Sensitivity	119
5.5	Conclusion	123

6	Lattice transport of two ions via eSTA	124
6.1	Introduction	124
6.2	System Hamiltonian	125
6.3	Approximate STA Hamiltonian	126
6.4	Calculation of eSTA correction	129
6.5	Robustness of eSTA to systematic errors	131
6.6	Classical comparison	136
6.7	Conclusion	138
7	Summary and Outlook	139
7.1	Summary	139
7.2	Outlook	141
	Bibliography	144

List of Abbreviations

eSTA	enhanced Shortcuts To Adiabaticity
FAQUAD	FAst QUasiADIabatic
FFT	Fast Fourier Transform
GPU	Graphics Processing Unit
GRAPE	Gradient Ascent Pulse Engineering
IBIE	Invariant-Based Inverse Engineering
L.R.	Lewis-Riesenfeld
NMR	Nuclear Magnetic Resonance
RAP	Rapid Adiabatic Passage
RWA	Rotating Wave Approximation
SFF	Streamlined Fast Forward
STA	Shortcuts To Adiabaticity
STIRAP	STImulated Raman Adiabatic Passage

Chapter 1

Introduction

At its heart, physics tries to explain the fundamental constituents and processes of our universe. Physics contains many different fields, each concerned with different aspects of matter, energy and the interaction between them. Within physics, quantum mechanics is the physical theory that seeks to describe and predict the dynamics of objects at the smallest scales. While many of the consequences of quantum mechanics can be unintuitive and surprising, there is enormous potential to use quantum mechanics to design new devices that push the boundaries of what is technologically possible. Currently, a second quantum revolution is ongoing [1], where new quantum technologies are emerging such as quantum computing, quantum metrology and quantum sensing [2, 3]. These potentially disruptive technologies go beyond what is even possible using their classical counterparts.

However, there are many challenges in designing practical quantum devices. At the fundamental level, quantum systems are sensitive to decoherence and the effect of the environment. Furthermore, there are practical limits on how well a quantum system can be isolated from the environment. Any theoretical design scheme needs to address this practical consideration, and one way to prevent decoherence is to employ fast control schemes that have a straightforward physical implementation. Within any realistic quantum device there will be constraints on the level of control that can be realised, and robust quantum

control techniques are needed that allow quantum devices to operate successfully even when the control is imperfect. Thus fast and robust quantum control is a critical prerequisite for any practical quantum technology.

Many practical quantum control techniques began with designing laser pulse shapes for specific applications. For example, chemical reactions can be controlled using laser pulses [4] and the structure of molecules can be determined using NMR spectroscopy, where the nuclei-spin of molecules in a magnetic field are manipulated using coherent light [5]. The interaction of laser light and matter is one of the cornerstones of modern quantum technologies, with quantum effects even being observable macroscopically as is the case with Bose-Einstein condensates (BECs). BECs are states of matter typical made from many particles, which mostly occupy a single quantum state. Quantum control techniques can be applied to the manipulation of BECs, and experimentally wavepacket interferometry has already been achieved in this setting [6]. This kind of interferometry has the potential to give rise to new classes of quantum sensors, that can out perform their classical counterparts at a fundamental level [3, 7].

As the development of lasers and other quantum technology platforms has progressed, the question of how to design optimal control schemes has become a critical roadblock to constructing practical quantum devices. There are many techniques that can be used to design control schemes for a given quantum system [7], but choosing an optimal design method depends heavily on the system under consideration. While numerical methods are often used in practical settings, they often do not scale well with system size and can require significant resources to implement. Analytic control methods have several major advantages over numerical methods: they are less computationally expensive, they can offer physical insight into the control process (e.g. reveal symmetries) and they can be chosen so that they are intrinsically robust against error. These

properties are particularly relevant to the current generation of noisy intermediate scale quantum (NISQ) devices [8]. Within the framework of analytical control techniques, adiabatic control schemes have been used extensively in experimental settings, for example STIRAP [9]. STIRAP has found many practical applications as it enables population transfer between two quantum states by following a dark state, meaning that population transfer can be achieved using coherent light and an intermediate state that is never populated during the process. However, there are many settings where adiabatic schemes require large timescales relative to the system coherence time, which make them susceptible to decoherence. These long timescales are also a problem for quantum technologies such as quantum computing or quantum sensing, where many different operations need to be repeated or concatenated together in sequence.

Shortcuts to adiabaticity (STA) are mostly analytic techniques that produce the same state transfer achieved by an adiabatic process, but in a much faster operation time that prevents decoherence [10, 11]. There is a plethora of STA techniques, with different techniques having advantages and disadvantages in different settings. For systems that admit analytical STA techniques, there are several methods to design control schemes with intrinsic robustness against errors and noise [11]. However, a limitation of all STA methods is that they work perfectly only for a limited number of quantum systems.

In this thesis we develop a general framework for extending existing STA techniques to systems which do not readily admit a STA solution. This general framework is called enhanced shortcuts to adiabaticity (eSTA) and uses the fact that many systems we would like to control can be approximated by systems where STA techniques can be easily applied. Using a perturbative approach, corrections to an existing STA technique can be calculated using eSTA, allowing control of systems beyond the current scope of STA alone. Several advantages of eSTA are consequences of how it is constructed as an extension of STA; eSTA is analytic and can take advantage of the useful properties of STA schemes, there

is significant freedom in choosing how one chooses the parameterisation of an eSTA scheme, and by construction eSTA is expected to give improved robustness against errors. There have already been applications of eSTA outside of this thesis, to single-atom transport in optical conveyor belts and double-well optical lattices [12, 13].

In the next chapter we review background information relevant to this thesis, starting with a review of the adiabatic theorem and a discussion of several STA techniques. We then introduce numerical techniques used throughout the thesis. In Chapter 3 the eSTA formalism is developed and applied in several key quantum control settings; population inversion in two-level systems without the rotating wave approximation and transport of one and two particles (with Coulomb interaction) in a Gaussian trap. It is shown that high fidelity control is achieved but the question of robustness is not addressed. In Chapter 4 the robustness of eSTA to different types of noise is investigated using the example of single atom transport in an optical lattice. It is shown that eSTA can improve the fidelity and robustness of transport simultaneously, for several different types of noise. This makes eSTA a very useful candidate for possible future experimental implementation. In Chapter 5 an alternative derivation of eSTA is presented that takes advantage of higher order terms in the eSTA formalism. At the expense of calculating a Hessian term, one assumption of the original eSTA derivation can be removed. Both the original and alternative eSTA schemes are applied to anharmonic trap expansion and shown to give high fidelity and exhibit improved robustness against noise. In Chapter 6, eSTA is used to transport two masses in a lattice potential with Coulomb interaction. Again eSTA produces higher fidelities and robustness against systemic noise. The thesis concludes with a summary and an outlook on future applications of eSTA.

Chapter 2

Background Theory

In this chapter we review material relevant to this thesis. We start with a review of the adiabatic theorem (Section 2.1), then introduce STA and discuss several applications of STA (Section 2.2). We conclude by introducing numerical techniques used throughout the thesis (Section 2.3).

2.1 The Adiabatic Theorem

The word “adiabatic” is derived from the Greek “*adiabatos*”, meaning “impassable” or “not passing through”. It was first introduced in 1858 by W.J.M. Rankine in reference to a thermodynamic process in which there is no heat transfer [14]. Modern thermodynamics uses “adiabatic” to refer to a thermodynamic process in which no heat or mass is transferred between the thermodynamic system and the environment [15]. Starting with Boltzmann, “adiabatic” began to also be used when describing processes for which the action E/ν (where ν is a frequency associated with the dynamics) remains constant. Later work by Einstein, Rayleigh and Ehrenfest led to “adiabatic invariance” being used to describe the constancy of E/ν , specifically when varying parameters of a (classical or quantum) system in an “infinitely slowly way”.

Unfortunately this has led to confusion. Adiabatic processes in classical thermodynamics are usually taken to mean that heat and mass is not transferred during the process. Note that classical adiabatic processes can be quasi-static

(at thermodynamic equilibrium during the process) or non-quasi-static. In contrast, modern quantum mechanics uses “adiabatic” to describe the dynamical evolution of a quantum system for which the system remains in an instantaneous energy eigenstate of the Hamiltonian during the time evolution. This means that a quantum adiabatic process is more akin to a classical quasi-static process, but we stress that the use of the word adiabatic is specific to the context in which it is used. The quantum idea of adiabaticity is made precise through the adiabatic theorem, first rigorously demonstrated for a closed quantum system with a discrete-spectrum Hamiltonian by Born and Fock in 1928 [16]. It was extended to non-discrete spectrum Hamiltonians by Kato in 1950 [17], and has since been further extended to degenerate spectrum cases [18], recast in the form of a geometrical holonomy evolution [19, 20] and to open quantum systems [21].

It is important to note that there is not one single unique adiabatic theorem. The proof of an adiabatic theorem depends on the physical setting and the assumed properties of the system Hamiltonian. However, each adiabatic theorem proof will follow a similar structure. We outline this structure by following the proof of the adiabatic theorem in [22], which essentially follows a streamlined form of Kato’s proof restricted to the discrete spectrum case [17, 23]. In the following we outline the main structure of the proof for closed quantum systems and further details can be found in [22].

We start with a closed quantum system with Hamiltonian $H(t)$, with the state of the system at time t given by $|\Psi(t)\rangle$. The Schrödinger equation describes the time-evolution of the system and is given by

$$i\hbar\frac{\partial}{\partial t}|\Psi(t)\rangle = H(t)|\Psi(t)\rangle. \quad (2.1)$$

We can describe this equivalently in terms of a time-evolution operator $U(t, 0)$, defined by $|\Psi(t)\rangle = U(t, 0)|\Psi(0)\rangle$, which satisfies

$$i\hbar \frac{d}{dt} U(t) = H(t)U(t). \quad (2.2)$$

We now introduce a parameter T , and define the dimensionless variable $s = t/T$, giving

$$i\hbar \frac{d}{ds} U_T(s) = T \tilde{H}(s)U_T(s), \quad (2.3)$$

where $s \in [0, 1]$, $\tilde{H}(s) = H(sT)$ and $U_T(s) = U(sT)$. We assume a discrete spectrum for $\tilde{H}(s)$ with eigenvalues $E_j(s)$ and corresponding projection operators $P_j(s)$. We further assume that the eigenvalues are piecewise differentiable and that there are no level crossings during the time evolution, i.e. $E_i(s) \neq E_j(s)$ for $i \neq j$ and $s \in [0, 1]$. The Hamiltonian can be written as $\tilde{H}(s) = \sum_j E_j(s)P_j(s)$.

The outline of the proof is to write U_T as a product of three unitary operators,

$$U_T(s, 0) = A(s)S_T(s)W_T(s, 0), \quad (2.4)$$

where $A(s)$ is used to move to a picture that diagonalises \tilde{H} , S_T allows us to eliminate an integrable contribution and W_T can be written in terms of another operator that eventually shows that $W_T(s, 0) = \mathbb{1} + \mathcal{O}(1/T)$.

We first consider a unitary transformation $A(s)$ that can diagonalise $\tilde{H}(s)$ (i.e. $A^\dagger(s)\tilde{H}(s)A(s)$ is diagonal), while simultaneously transfer a given $P_j(0)$ to $P_j(s)$. We assume $A(s)$ to satisfy

$$P_j(s) = A(s)P_j(0)A^\dagger(s), \quad (2.5)$$

with $A(0) = \mathbb{1}$. Note that A has a number of equivalent interpretations; as an

operator that diagonalises \tilde{H} , as a map taking Eq. (2.3) to a frame rotating with the instantaneous eigenvectors of \tilde{H} or as a mapping of Eq. (2.3) to a frame where the projection operators are constant in time. The Hamiltonian will then split into diagonal terms and other contributions, which we will eventually use to show that the full time evolution operator differs from the identity by terms $\mathcal{O}(1/T)$.

We assume $A(s)$ satisfies

$$i\hbar \frac{d}{ds} A(s) = K(s)A(s), \quad (2.6)$$

with $A(0) = \mathbf{1}$ and $K(s)$ is a Hermitian operator. We choose

$$K(s) = i\hbar \sum_j \frac{d}{ds} P_j(s) P_j(s) \quad (2.7)$$

which guarantees that in the $A(s)$ picture the projection operators are constant $P_j^{(A)}(s) = P_j(0)$ with

$$\tilde{H}^{(A)}(s) = \sum_j E_j(s) P_j(0). \quad (2.8)$$

Now we can write the Schrödinger equation in the $A(s)$ picture, as

$$i\hbar \frac{d}{ds} U^{(A)}(s) = T \left[\tilde{H}^{(A)}(s) - \frac{1}{T} K^{(A)}(s) \right] U^{(A)}(s), \quad (2.9)$$

where $U^{(A)}(0) = \mathbf{1}$ and $K^{(A)}(s) = A^\dagger(s)K(s)A(s)$. Note that $\tilde{H}^{(A)}(s)$ and $K^{(A)}(s)$ are independent of T so it is to be expected that in the limit $T \rightarrow \infty$ the first term on the right hand side should dominate. We define

$$i\hbar \frac{d}{ds} S_T(s) = T \tilde{H}^{(A)}(s) S_T(s), \quad (2.10)$$

with $S_T(0) = \mathbb{1}$. This is integrable and can be solved to give

$$S_T(s) = \sum_j \exp \left[-\frac{iT}{\hbar} \int_0^s du E_j(u) \right] P_j(0). \quad (2.11)$$

To complete the proof a second transformation is made using an operator $W_T(s)$ in a similar manner to the $A(s)$ definition. This ultimately allows the original time evolution operator for $T \rightarrow \infty$, to be written as

$$U_T(s) = A(s)S_T(s) \left[\mathbb{1} + \mathcal{O} \left(\frac{1}{T} \right) \right]. \quad (2.12)$$

By Eq. (2.11), $S_T(s)$ and $P_j(0)$ commute, thus

$$A(s)S_T(s)P_j(0) = P_j(s)A(s)S_T(s). \quad (2.13)$$

Hence in the limit $T \rightarrow \infty$ the time evolution follows the adiabatic picture represented by $A(s)S_T(s)$ exactly and the system remains in the initial eigenstate it started in, up to a phase factor. Again, the details of the proof can be found in [22].

We now consider the specific case where the initial state $|\psi(0)\rangle$ is an eigenstate $|\phi_m(0)\rangle$ of the Hamiltonian $\tilde{H}(0)$, and consider the action of the time evolution in Eq. (2.12). Following again the details in [22], we obtain

$$\begin{aligned} |\psi(s)\rangle &= U_T(s, 0)|\psi(0)\rangle \approx A(s)S_T(s)|\phi_m(0)\rangle \\ &\approx A(s)|\phi_m(0)\rangle \exp \left[-\frac{iT}{\hbar} \int_0^s du E_m(u) \right] \\ &= |\phi_m(s)\rangle \exp \left[-\frac{iT}{\hbar} \int_0^s du E_m(u) \right]. \end{aligned} \quad (2.14)$$

Hence the system remains in the initial instantaneous eigenstate up to a phase term. If we consider the probability that the system is in a different eigenstate

at time s ,

$$P(s) = \sum_{j \neq m} |\langle \phi_j(s) | U_T(s, 0) | \phi_m(0) \rangle|^2, \quad (2.15)$$

and use time-dependent perturbation theory, we obtain the adiabatic approximation [22]

$$P(s) \approx \sum_{j \neq m} \left| \int_0^s du \exp \left\{ \frac{iT}{\hbar} \int_0^u dv [E_j(v) - E_m(v)] \right\} \langle \phi_j(u) | \frac{d}{du} \phi_m(u) \rangle \right|^2 \lll 1. \quad (2.16)$$

If we consider E_j, E_m and $\langle \phi_j | d/ds \phi_m \rangle$ independent of s , we can derive a rough estimate for the adiabatic approximation

$$\begin{aligned} P(s) &\approx \sum_{j \neq m} \frac{1}{T} \left| \frac{\langle \phi_j | \frac{d}{ds} \phi_m \rangle}{(E_j - E_m)/\hbar} \right|^2 \left| 1 - \exp \left[\frac{iTs}{\hbar} (E_j - E_m) \right] \right|^2 \\ &\leq \sum_{j \neq m} \frac{4}{T} \left| \frac{\langle \phi_j | \frac{d}{ds} \phi_m \rangle}{(E_j - E_m)/\hbar} \right|^2, \end{aligned} \quad (2.17)$$

and assuming $P(s) \lll 1$ we have

$$\sum_{j \neq m} \left| \frac{\langle \phi_j | \frac{d}{ds} \phi_m \rangle}{(E_j - E_m)/\hbar} \right|^2 \lll \frac{T}{4}. \quad (2.18)$$

If we assume E_j, E_m and $\langle \phi_j | d/ds \phi_m \rangle$ are varying sufficiently smoothly in s [22, 24], we have a rough condition for the adiabatic approximation

$$\sum_{j \neq m} \max_{0 \leq s \leq 1} \left| \frac{\langle \phi_j(s) | \frac{d}{ds} \phi_m(s) \rangle}{(E_j(s) - E_m(s))/\hbar} \right|^2 \lll T. \quad (2.19)$$

Tighter bounds and more general bounds can be found by considering further terms in the time-dependent perturbation expansion, but their utility will depend on the form of the system Hamiltonian [24]. Also worth noting is that

the conditions in Eq. (2.18) and Eq. (2.19) are not in general sufficient or necessary to ensure adiabatic evolution. However, for many applications they do guarantee adiabaticity and they have been used in many practical settings, for example in Landau-Zener models, rapid adiabatic passage (RAP) and stimulated Raman adiabatic passage (STIRAP). A common application is the design of a control pulse, where state transfer can be accomplished using a linear ramp over a large enough time to ensure adiabaticity [25].

As noted in [26], there is a straightforward way that the adiabatic limit $T \rightarrow \infty$ can be achieved in finite time for bounded Hamiltonians. We set $\tilde{H}_{\max} = \max |\tilde{H}(s)|$, then rescale with $h(s) = \tilde{H}/\tilde{H}_{\max}$. Eq. (2.3) has Hamiltonian $T\tilde{H}_{\max}h(s)$, and $h(s)$ and $\tilde{H}(s)$ will produce the same $A(s)$ and $K(s)$. In this case the adiabatic limit can be reached by fixing T and letting $\tilde{H}_{\max} \rightarrow \infty$. This gives an intuition as to why adiabatic population transfer in experimental settings can often require strong control fields. However, in practical settings there are constraints on implementing a given Hamiltonian, for example limited laser intensity or finite magnetic field strength. This has motivated the development of shortcuts to adiabaticity, which will be discussed in Section 1.2.

The adiabatic approximation can be derived in alternative manner using the approach taken by Berry in [19, 27, 28]. In this case we make the same assumptions about the Hamiltonian as we did before, but we consider the unscaled Hamiltonian $H(t)$ and make an ansatz for the wavefunction

$$|\psi(t)\rangle = \sum_n c_n(t) e^{i\theta_n(t)} |\phi_n(t)\rangle, \quad (2.20)$$

where $H(t)|\phi_n(t)\rangle = E_n|\phi_n(t)\rangle$, $\sum_n |c_n(t)|^2 = 1$ and the dynamical phase is

$$\theta_n(t) = -\frac{1}{\hbar} \int_0^t ds E_n(s). \quad (2.21)$$

Substituting Eq. (2.20) into the time-dependent Schrödinger equation, and simplifying we obtain

$$\sum_n \dot{c}_n |\phi_n\rangle = - \sum_n c_n |\dot{\phi}_n\rangle. \quad (2.22)$$

We now apply $\langle \phi_m |$ and get

$$\dot{c}_m = -c_m \langle \phi_m | \dot{\phi}_m \rangle - \sum_{n \neq m} c_n \langle \phi_m | \dot{\phi}_n \rangle e^{i(\theta_n - \theta_m)}. \quad (2.23)$$

Note that differentiating $H(t)|\phi_n(t)\rangle = E_n(t)|\phi_n(t)\rangle$ and applying $\langle \phi_m |$ one gets that

$$\langle \phi_m | \dot{\phi}_n \rangle = \frac{\langle \phi_m | \dot{H} | \phi_n \rangle}{E_n - E_m}, \quad (2.24)$$

thus Eq. (2.23) becomes

$$\dot{c}_m = -c_m \langle \phi_m | \dot{\phi}_m \rangle - \sum_{n \neq m} c_n \frac{\langle \phi_m | \dot{H} | \phi_n \rangle}{E_n - E_m} e^{i(\theta_n - \theta_m)}. \quad (2.25)$$

We now make the adiabatic approximation, whereby we assume that the Hamiltonian is changing slowly enough in time such that $\langle \phi_m | \dot{H} | \phi_n \rangle \ll E_n - E_m$. Hence,

$$\dot{c}_m = -c_m \langle \phi_m | \dot{\phi}_m \rangle, \quad (2.26)$$

which has solution

$$c_m(t) = c_m(0) e^{i\gamma_m(t)}, \quad (2.27)$$

with the geometric phase defined as $\gamma_m(t) = i \int_0^t ds \langle \phi_m(s) | d/ds \phi_m(s) \rangle$. Note here that $\langle \phi_m | \phi_m \rangle = 1$ thus $\langle \phi_m(s) | d/ds \phi_m(s) \rangle$ is purely imaginary, and so $\gamma_m(t)$ is strictly real valued. If we consider an initial state in the instantaneous energy

eigenbasis $|\psi(0)\rangle = \sum_n c_n(0)|\phi_n(0)\rangle$, the state will evolve in the adiabatic limit to

$$|\psi(t)\rangle \approx \sum_n c_n(0) e^{i\theta_n(t)} e^{i\gamma_n(t)} |\phi_n(t)\rangle. \quad (2.28)$$

As found before in the previous approach, the state remains in the initial instantaneous eigenstate but acquires a dynamical phase $\theta_n(t)$ and a geometric phase $\gamma_n(t)$. The important distinction between these phases is that the dynamical phase depends on the rate of change of the instantaneous energy eigenvalues of the system and the total evolution time, whereas the geometric phase depends on the structure or geometry of the eigenstates and not on the total time. This can be seen by considering the dependence of the Hamiltonian on a vector parameter $\vec{v}(t)$, i.e. $H[\vec{v}(t)]$. Then the eigenstates will also depend on $\vec{v}(t)$, i.e. $|\phi_n[\vec{v}(t)]\rangle$ and after using the chain rule we have that

$$\gamma_n(t) = i \int_0^t ds \langle \phi_n(s) | d/ds \phi_n(s) \rangle = i \int_{\vec{v}(0)}^{\vec{v}(t)} d\vec{v} \cdot \langle \phi_n(\vec{v}) | \nabla_{\vec{v}} \phi_n(\vec{v}) \rangle, \quad (2.29)$$

thus the geometric phase depends on the geometry of parameter space, but not on the speed at which the path is traversed in parameter space.

In summary, the adiabatic theorem is an important theoretical and practical tool for control of quantum systems in a variety of contexts. While adiabatic control is useful in certain systems, it requires long control times which allows decoherence to degrade the performance of the control scheme. Shortcuts to adiabaticity (STA) are a collection of techniques that can address these issues, and we discuss them further in the next section.

2.2 Shortcuts to Adiabaticity

A natural question arises as a consequence of the adiabatic theorem; can we design a control scheme that allows the same adiabatic transfer of an initial

state to a chosen target state, but in a chosen operation time? This is the central idea behind shortcuts to adiabaticity (STA), which are a collection of mostly analytic techniques that allow adiabatic population transfer but on much shorter time-scales.

There are many techniques within the STA framework; inverse engineering via Lewis-Riesenfeld invariants, the fast-forward approach, counterdiabatic driving, variational methods and approximate methods such as FAQUAD and STA in combination with optimal control theory [10, 11]. The diversity of STA techniques available has allowed them to be applied in many different settings, for example, suppression of pair production in driven Dirac dynamics [29], fast dynamical exchange cooling with trapped ions [30], transport of BECs in harmonic traps [31] and compression of solitons [32]. STA has also been applied to the control of classical systems, for example STA based crane control [33, 34].

An important consideration for any quantum control protocol is how robust it is against noise. The inherent freedom within STA allows control protocols to be designed from the start with robustness against noise in mind, while simultaneously achieving the desired state transfer. Robustness of STA against noise has been considered in several settings, for example the fast transport of atoms [35], the transport of two ions under slow spring-constant drifts [36] and noisy population inversion [37]. Analytical STA control schemes can offer physical insight into the control problem, and certain properties can be used to simplify or enhance physical implementation of the protocol e.g. symmetries in the control scheme.

These advantages of STA make them very useful for practical implementation. STA have been applied experimentally to a number of systems, for example; trapped ion transport [38], fast ion separation in segmented Paul traps [39], optical transfer [40], STA enhanced STIRAP [41], decompression and displacement of Bose-Einstein condensates and ultra-cold gases [25, 42].

In the next sections we introduce several STA techniques; counterdiabatic

driving, the fast forward approach and inverse engineering using Lewis-Riesenfeld invariants.

2.2.1 Counterdiabatic driving

The goal of counterdiabatic driving is to control a quantum system with Hamiltonian H_0 . We assume we know the instantaneous energy eigenstates of H_0 and that H_0 has a non-degenerate spectrum. We then construct a counterdiabatic Hamiltonian H_{CD} , such that the full system with Hamiltonian $H = H_0 + H_{CD}$ follows the instantaneous energy eigenstates of H_0 but in a shorter times. Note that the instantaneous energy eigenstates of H are irrelevant in this discussion, and that counterdiabatic driving allows the same adiabatic population transfer of the system with Hamiltonian H_0 alone, to be implemented on the system with Hamiltonian H . Counterdiabatic driving was first introduced by Demirplak and Rice [43], and independently derived via transitionless quantum driving by Berry [27].

In the language of the proof of the adiabatic theorem from Section 2.1, counterdiabatic driving amounts to adding a Hamiltonian term in Eq. (2.9) such that the non-adiabatic terms are eliminated, i.e.

$$i\hbar \frac{d}{dt} U^{(A)}(t) = \left[H^{(A)}(t) + H_{CD}^{(A)}(t) - K^{(A)}(t) \right] U^{(A)}(t), \quad (2.30)$$

where A is used to transform to the adiabatic frame and we choose $H_{CD}^{(A)}(t)$ such that it cancels $K^{(A)}(t)$. This can be achieved using

$$H_{CD}(t) = i\hbar \sum_n \frac{d}{dt} P_n(t) P_n(t), \quad (2.31)$$

where $P_n(t) = |\phi_n(t)\rangle\langle\phi_n(t)|$.

The counterdiabatic term can be derived in a number of ways, and here we follow the formalism developed by Berry [27]. We consider a closed quantum

system with Hamiltonian $H_0(t)$, whose instantaneous eigenvectors are $|\phi_n(t)\rangle$ with eigenvalues $E_n(t)$. We assume that the system is initially in an eigenstate $|\phi_n(0)\rangle$ of $H_0(0)$, and in the adiabatic approximation (Eq. (2.28)) we have

$$|\psi_n(t)\rangle = e^{i\zeta_n(t)}|\phi_n(t)\rangle, \quad (2.32)$$

where $\zeta_n(t) = \theta_n(t) + \gamma_n(t)$ and the dynamic phase $\theta_n(t)$ and geometric phase $\gamma_n(t)$ are defined by Eq. (2.21) and Eq. (2.29) respectively. The goal of counterdiabatic driving is to find a Hamiltonian $H(t)$ such that $|\psi_n(t)\rangle$ are exact evolving states with

$$i\hbar \frac{\partial}{\partial t} |\psi_n(t)\rangle = H(t) |\psi_n(t)\rangle. \quad (2.33)$$

We assume

$$U(t) = \sum_n e^{i\zeta_n(t)} |\phi_n(t)\rangle \langle \phi_n(0)|, \quad (2.34)$$

and using $H(t) = i\hbar \dot{U}U^\dagger$, we have that

$$\begin{aligned} H(t) &= i\hbar \sum_n \left[i\dot{\zeta}_n |\phi_n(t)\rangle \langle \phi_n(t)| + |\dot{\phi}_n(t)\rangle \langle \phi_n(t)| \right], \\ &= H_0(t) + H_{CD}(t), \end{aligned} \quad (2.35)$$

which can be simplified using the definitions of the dynamical and geometric phases from Eq. (2.21) and Eq. (2.29), giving

$$\begin{aligned} H_0(t) &= \sum_n E_n(t) |\phi_n(t)\rangle \langle \phi_n(t)|, \\ H_{CD}(t) &= i\hbar \sum_n (|\partial_t \phi_n\rangle \langle \phi_n| - \langle \phi_n | \partial_t \phi_n \rangle |\phi_n\rangle \langle \phi_n|), \end{aligned} \quad (2.36)$$

which is equivalent to Eq. (2.31) using $P_n(t) = |\phi_n(t)\rangle \langle \phi_n(t)|$. Note that if we

specify the eigenstates $|\phi_n(t)\rangle$ rather than $H_0(t)$, we have freedom to choose $E_n(t)$. This illustrates that many Hamiltonians can generate the dynamics of a given $|\phi_n(t)\rangle$, and they are defined by the choice of phases. For example, choosing $E_n(t) = 0$ gives $U(t) = \sum_n |\phi_n(t)\rangle\langle\phi_n(0)|$ with $H(t) = i\hbar \sum_n |\partial_t \phi_n\rangle\langle\phi_n|$ [27]. In this example $H_0(t)$ is only relevant through the eigenvectors $|\phi_n(t)\rangle$.

Counterdiabatic driving has been applied to many settings, for example expansion of a harmonic trap [44], many body systems [45, 46] and open quantum systems [47]. One problem that can arise with counterdiabatic driving is whether the additional H_{CD} Hamiltonian can be implemented experimentally. For example, direct calculation of H_{CD} for harmonic trap expansion takes the form of a non-local operator [44]. One way to resolve this issue is to move to a suitable interaction picture where H_{CD} takes a physically implementable form [48]. Another strategy is to combine counterdiabatic driving with a variational approach that allows one to find the best approximate scheme given constraints on the type of control available [49]. This approach is particularly useful for many body systems where calculating the full spectrum of the Hamiltonian is not feasible [50]. This approach has also been extended to an open system context [51]. Another strategy is to use counterdiabatic driving in conjunction with optimal control theory, which has been experimentally implemented in control of a QED superconducting circuit [52].

Counterdiabatic driving has also found applications outside of quantum control, for example, controlling the speed and trajectory of biological evolution [53] and control of classical systems [54].

2.2.2 The Streamlined Fast Forward approach

The fast forward approach was first introduced by Masuda and Nakamura [55]. This method was streamlined in [56], and shown to be essentially a method for inverting the Schrödinger equation. The streamlined fast forward method has

been applied to eigenstate transfer by trap deformation in [57]. We will follow this approach, and demonstrate the example of harmonic trap expansion.

We start with the one dimensional time-dependent Schrödinger equation

$$i\hbar \frac{\partial}{\partial t} \Psi(x, t) = \left[-\frac{\hbar^2}{2m} \frac{\partial^2}{\partial x^2} + V(x, t) \right] \Psi(x, t). \quad (2.37)$$

Given the time-dependent potential $V(x, t)$, our goal is to evolve an initial energy eigenstate $\Psi(x, 0) = \psi_0(x)$ to a final energy eigenstate $\Psi(x, t_f) = \psi_f(x)$. We invert the Eq. (2.37) for the potential,

$$V(x, t) = \frac{1}{\Psi(x, t)} \left[i\hbar \frac{\partial \Psi(x, t)}{\partial t} + \frac{\hbar^2}{2m} \frac{\partial^2 \Psi(x, t)}{\partial x^2} \right]. \quad (2.38)$$

We use the modulus-phase form of the wave function,

$$\Psi(x, t) = \rho(x, t) \exp^{i\phi(x, t)}, \quad (2.39)$$

and by imposing that the potential is real, i.e. $\text{Im}[V(x, t)] = 0$, we obtain

$$\frac{1}{\rho} \frac{\partial \rho}{\partial t} + \frac{\hbar}{2m} \left(\frac{2}{\rho} \frac{\partial \phi}{\partial x} \frac{\partial \rho}{\partial x} + \frac{\partial^2 \phi}{\partial x^2} \right) = 0. \quad (2.40)$$

Rewriting this and multiplying across by ρ^2 , we get

$$\rho \frac{\partial \rho}{\partial t} = -\frac{\hbar}{2m} \left(2\rho \frac{\partial \phi}{\partial x} \frac{\partial \rho}{\partial x} + \rho^2 \frac{\partial^2 \phi}{\partial x^2} \right) = -\frac{\hbar}{2m} \frac{\partial}{\partial x} \left(\frac{\partial \phi}{\partial x} \rho^2 \right). \quad (2.41)$$

We define

$$\frac{\partial \phi}{\partial x} = -\frac{m}{\hbar} u(x, t). \quad (2.42)$$

Using $\frac{\partial \rho^2}{\partial t} = 2\rho \frac{\partial \rho}{\partial t}$, Eq. (2.41) becomes

$$\frac{\partial}{\partial t} \rho^2 = \frac{\partial}{\partial x} (u \rho^2). \quad (2.43)$$

Then we have

$$u(x, t) = \frac{1}{\rho^2(x, t)} \frac{\partial}{\partial t} \left[\int_0^x \rho^2(x', t) dx' \right]. \quad (2.44)$$

Using

$$\rho \operatorname{Re} [V(x, t)] = \frac{\hbar^2}{2m} \left[\frac{\partial^2 \rho}{\partial x^2} - \left(\frac{\partial \Phi}{\partial x} \right)^2 \rho \right] - \hbar \rho \frac{\partial \Phi}{\partial t}, \quad (2.45)$$

and Eq. (2.42), Eq. (2.43) and Eq. (2.44), we obtain

$$\begin{aligned} V(x, t) &= m \frac{\partial}{\partial t} \left[\int_0^x \rho^2(x', t) dx' \right] + \frac{\hbar^2}{2m} \frac{1}{\rho(x, t)} \frac{\partial^2 \rho(x, t)}{\partial x^2} \\ &\quad - \frac{1}{2} u^2(x, t) - \hbar \frac{\partial \Phi(x, t)}{\partial t}. \end{aligned} \quad (2.46)$$

The advantage of this approach is that now $V(x, t)$ is written solely in terms of $\rho(x, t)$ (via Eq. (2.42) and Eq. (2.44)), making the required potential easier to calculate.

We now use this technique to design a control scheme that takes the ground-state of a harmonic trap with initial frequency ω_0 , to the groundstate of the harmonic trap with final trap frequency ω_f , in a given expansion time t_f . For convenience we move to dimensionless variables, using ω_0^{-1} and $\sqrt{\hbar/m\omega_0}$ as units of time and distance respectively. We set $\alpha = \omega_f/\omega_0$ and the initial and final wave functions, potentials and energies are given by

$$\psi_0(x) = \left(\frac{1}{\pi} \right)^{\frac{1}{4}} e^{-\frac{x^2}{2}}, \quad V(x, 0) = \frac{1}{2} x^2, \quad E_0 = \frac{1}{2}, \quad (2.47)$$

$$\psi_f(x) = \left(\frac{\alpha}{\pi} \right)^{\frac{1}{4}} e^{-\frac{(\sqrt{\alpha}x)^2}{2}}, \quad V(x, t_f) = \frac{1}{2} \alpha^2 x^2, \quad E_f = \frac{\alpha}{2}. \quad (2.48)$$

This transformation is an expansion of the initial trap when $0 < \alpha < 1$, and a compression when $\alpha > 1$.

We now consider

$$\rho(x, t) = \left(\frac{1}{\pi}\right)^{\frac{1}{4}} \sqrt{\alpha^{\frac{\eta(t)}{2}}} e^{-\frac{1}{2}(\alpha^{\frac{\eta(t)}{2}} x)^2}, \quad (2.49)$$

where we assume

$$\begin{aligned} \eta(0) &= 0, & \eta(t_f) &= 1, \\ \dot{\eta}(0) &= \dot{\eta}(t_f) = 0, & \ddot{\eta}(0) &= \ddot{\eta}(t_f) = 0, \end{aligned} \quad (2.50)$$

and where we have ensured (see [57] for details)

$$\rho(x, 0) = \psi_i(x) \quad \text{and} \quad \rho(x, t_f) = \psi_f(x), \quad (2.51)$$

with $\dot{\rho}(x, t') = \ddot{\rho}(x, t') = 0$ for $t' = 0, t_f$. Using Eq. (2.46), we can then write the potential fully analytically as

$$\begin{aligned} V(x, t) &= \frac{1}{2} x^2 \left[\alpha^{4\eta(t)} + \log(\alpha) \left(\eta''(t) - \log(\alpha) \eta'(t)^2 \right) \right] \\ &\quad - \frac{1}{2} \left(\alpha^{2\eta(t)} + 2\dot{\phi}(0, t) \right), \end{aligned} \quad (2.52)$$

where we have chosen polynomial interpolations for $\eta(t)$ and $\phi(0, t)$ that satisfy the appropriate boundary conditions,

$$\phi(0, t) = \frac{t}{t_f} \left(1 - \frac{t}{t_f}\right) \left[\frac{(E_i + E_f)t - E_i t_f}{\hbar} \right], \quad (2.53)$$

$$\eta(t) = \frac{t^3}{t_f^3} \left[1 + 3 \left(1 - \frac{t}{t_f}\right) + 6 \left(1 - \frac{t}{t_f}\right)^2 \right]. \quad (2.54)$$

In Fig. 2.1 we plot an example of the time evolution of this trap expansion.

Note that calculating the potential using Eq. (2.46) could result in potentials that are difficult to implement experimentally. Another issue arises when evolving from an even to odd parity state, as problems of divergence emerge in

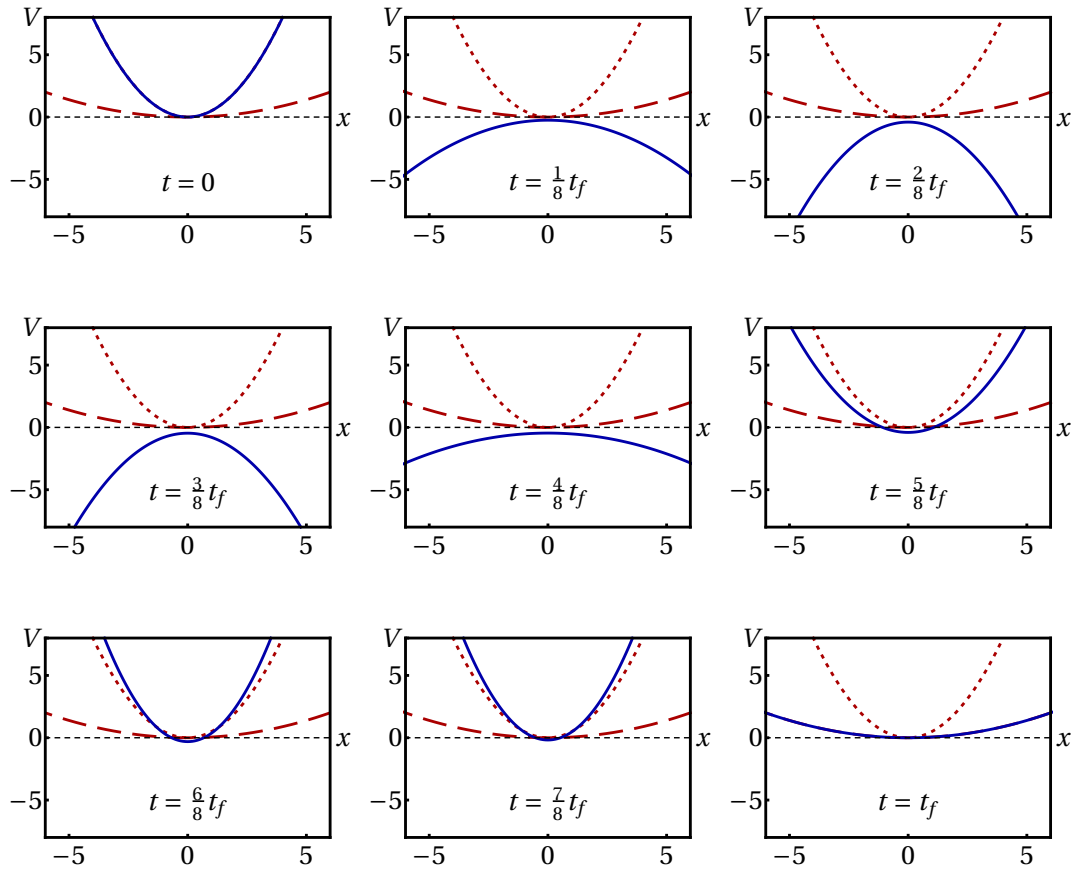


FIGURE 2.1: The figure is read left to right, and then descended row by row. The sequence of images illustrates the time evolution of $V(x, t)$ due to $\rho(x, t)$, evaluated at $t_f/8$ intervals, shown as the blue solid line. The dotted-red line is a harmonic trap with angular frequency ω_0 , and the dashed-red line is the final harmonic potential with $\omega_f = 1/3 \omega_0$.

the inversion process. While there has been progress to counteract divergences [58], it is still a nontrivial task to implement these kinds of state transfers.

In the next section we introduce a STA method called Lewis-Riesenfeld (L.R.) invariant-based inverse engineering. This technique can be considered special case of the fast forward approach [56], but offers a simpler design procedure specifically when considering potentials of the Lewis-Leach type [59].

2.2.3 Invariant-based inverse engineering

We consider the time-dependent Schrödinger equation,

$$i\hbar \frac{\partial}{\partial t} |\Psi(t)\rangle = H(t) |\Psi(t)\rangle, \quad (2.55)$$

where $|\Psi(t)\rangle$ is an arbitrary solution. A Lewis-Riesenfeld invariant for the Hamiltonian $H(t)$ is a Hermitian operator $I(t)$ that satisfies

$$\langle \Psi(t) | I(t) | \Psi(t) \rangle = c, \quad (2.56)$$

where c is a constant. We now take the time-derivative of Eq. (2.56) and using Eq. (2.55), together with the fact that $I(t) |\Psi(t)\rangle$ is also a solution of the Schrödinger equation, Eq. (2.56) becomes

$$\frac{dI(t)}{dt} = \frac{\partial I(t)}{\partial t} + \frac{i}{\hbar} [H(t), I(t)] = 0. \quad (2.57)$$

An operator $I(t)$ satisfying Eq. (2.57) is also called a dynamical invariant or a constant of motion, since the eigenvalues of $I(t)$ are time independent [10, 11]. If we assume a discrete non-degenerate spectrum for the invariant $I(t)$, an arbitrary solution $|\Psi(t)\rangle$ of the Schrödinger equation can be written in terms of the instantaneous eigenstates $\{|\phi_n(t)\rangle\}_n$ of $I(t)$ up to a phase factor,

$$|\Psi(t)\rangle = \sum_{n=0}^{\infty} c_n e^{i\alpha_n(t)} |\phi_n(t)\rangle, \quad (2.58)$$

where

$$\alpha_n(t) = \frac{1}{\hbar} \int_0^t \langle \phi_n(t') | i\hbar \frac{\partial}{\partial t'} - H(t') | \phi_n(t') \rangle dt', \quad (2.59)$$

is the Lewis-Riesenfeld phase (see [60] for further details) and the c_n are time independent.

Lewis-Riesenfeld invariants were first introduced in [60], where they were used to solve for the state driven by a given time-dependent Hamiltonian. They were further generalised in [59] and [61], and they have found numerous applications in quantum physics, from the transport of Bose Einstein condensates [62], to applications with non-Hermitian Hamiltonians [63]. There are many possible invariants for a given Hamiltonian, a simple example is $|\Psi(t)\rangle\langle\Psi(t)|$, where $\Psi(t)$ is a solution of the Schrödinger equation. Finding invariants for a given Hamiltonian is in general non-trivial, but L.R. invariants are known for Hamiltonians linear and quadratic in momentum as well as 2,3 and 4 level systems [11].

Invariant-based inverse engineering uses the existence of an invariant and given initial and final states, to engineer the Hamiltonian - the reverse process of the original application of invariants in [60]. To be precise, assume the system is initially in state $|\Psi(0)\rangle$ at $t = 0$, with Hamiltonian $H(0)$. The goal is to evolve the system to a final state $|\Psi(t_f)\rangle$ in a given total time $t = t_f$, with Hamiltonian $H(t_f)$. The key idea that during the time interval $[0, t_f]$ the system follows the instantaneous eigenstates of $I(t)$ (up to a time-dependent phase), rather than the instantaneous energy eigenstates of $H(t)$. Given $I(t)$, we can formally assume a time evolution operator of the form

$$U = \sum_n e^{i\alpha_n(t)} |\phi_n(t)\rangle\langle\phi_n(0)|, \quad (2.60)$$

which implies that $H(t) = i\hbar\dot{U}U^\dagger$. Thus knowledge of an invariant $I(t)$ allows us to reverse engineer the required $H(t)$ for a given state transfer during $[0, t_f]$. Note that the populations of each n^{th} eigenstate of $I(t)$ will remain constant [11]. We can enforce that the eigenstates of $I(t)$ and $H(t)$ are the same at $t = 0$ and $t = t_f$ by setting

$$[H(0), I(0)] = [H(t_f), I(t_f)] = 0. \quad (2.61)$$

Now we can take advantage of freedom in the invariant to design schemes that need to be consistent only with Eq. (2.57) and Eq. (2.61) to ensure the desired state transfer.

Invariant-based engineering allows perfect control of an important class of potentials, the Lewis-Leach type potentials [59],

$$V(x, t) = \frac{1}{2}m\omega^2(t)x^2 - F(t)x + \frac{1}{\rho^2(t)}U\left[\frac{x - q_c(t)}{\rho(t)}\right] + f(t), \quad (2.62)$$

where the Hamiltonian of the system is $H(t) = p^2/2m + V(x, t)$ and $\rho(t)$ is a time-dependent function. This family of Hamiltonians has known quadratic in momentum invariants

$$I = \frac{1}{2m}[\rho(p - m\dot{q}_c) - m\dot{\rho}(x - q_c)]^2 + \frac{1}{2}m\omega_0^2\left(\frac{x - q_c}{\rho}\right)^2 + U\left(\frac{x - q_c}{\rho}\right), \quad (2.63)$$

where the functions ρ, q_c, ω and F must satisfy the auxiliary equations

$$\ddot{\rho} + \omega^2(t)\rho = \frac{\omega_0^2}{\rho^3} \quad (2.64)$$

$$\ddot{q}_c + \omega^2(t)q_c = \frac{F(t)}{m}, \quad (2.65)$$

and ω_0 is a constant (often chosen for convenience to be $\omega(t = 0)$). These equations are found by using Eq. (2.63) in Eq. (2.57). Eq. (2.64) is known as the Ermakov equation [64, 65] and Eq. (2.65) is the Newton equation of motion for a forced harmonic oscillator. The Lewis-Riesenfeld phase is given by

$$\alpha_n(t) = -\frac{1}{\hbar} \int_0^t dt' \left\{ \frac{\lambda_n}{\rho^2} + \frac{m}{2\rho^2} [(\dot{q}_c\rho - q_c\dot{\rho})^2 - (\omega_0 q_c/\rho)^2] + f \right\} \quad (2.66)$$

and the invariant eigenvectors

$$\phi_n(x, t) = \exp \left\{ \frac{im}{\hbar} \left[\frac{\dot{\rho}}{2\rho} x^2 + \frac{x}{\rho} (\dot{q}_c \rho - q_c \dot{\rho}) \right] \right\} \rho^{1/2} \Phi_n(\sigma), \quad (2.67)$$

where $\sigma = (x - q_c)/\rho$, and $\Phi_n(\sigma)$ is a solution of the stationary Schrödinger equation

$$\left[-\frac{\hbar^2}{2m} \frac{\partial^2}{\partial \sigma^2} + \frac{1}{2} m \omega_0^2 \sigma^2 + U(\sigma) \right] \Phi_n = \lambda_n \Phi_n. \quad (2.68)$$

The function $\rho(t)$ describes the wave function width while $q_c(t)$ corresponds with a classical particle trajectory. By choosing an ansatz for $\rho(t)$ and $q_c(t)$ that satisfy appropriate appropriate boundary conditions that are found using Eq. (2.61), we can then calculate $F(t)$ and $\omega(t)$ using Eq. (2.65) and Eq. (2.64) respectively, as we will demonstrate in later examples.

Note that the Lewis-Leach family of potentials has many applications in experimental settings, since near the minimum x_0 of any one dimensional trapping potential $V(x)$ we can approximate the potential using a Taylor series [66],

$$V(x) = V(x_0) + V'(x_0)(x - x_0) + \frac{V''(x_0)}{2}(x - x_0)^2 + \mathcal{O}(x^3). \quad (2.69)$$

Quantum information experiments have been conducted using trapped ions for several decades, where the potentials are often approximated harmonically when designing control schemes [67–69]. More recently, shuttling trapped ions has been theoretically explored and experimentally demonstrated to provide a possible architecture for future large scale quantum computing [39, 66, 70, 71].

Finally, in comparison to the previous streamlined fast-forward approach the invariant-based inverse engineering approach is a much simpler way to calculate the required control functions for Lewis-Leach potentials. In the next subsections we consider several examples of invariant-based inverse engineering; trap expansion, trap transport and two-level population inversion.

Fast harmonic trap expansion using Lewis-Riesenfeld invariants

We now consider transferring the ground state of a harmonic trap with frequency $\omega(0) = \omega_0$ to the ground state of a harmonic trap with frequency $\omega(t_f) = \omega_f$. This problem has been studied in detail in [72]. The Hamiltonian for this system has a Lewis-Leach type potential, given by

$$H(t) = \frac{p^2}{2m} + \frac{1}{2}m\omega^2(t)x^2. \quad (2.70)$$

The associated L.R. invariant Eq. (2.63) simplifies to

$$I = \frac{1}{2m} [\rho p - m\dot{\rho}x]^2 + \frac{1}{2}m\omega_0^2 \left(\frac{x}{\rho} \right)^2, \quad (2.71)$$

where in Eq. (2.63) we have set $U = 0$ and $q_c = F = 0$. Note that in principle ω_0 is arbitrary in I , but for this example it is convenient to define $\omega(0) = \omega_0$.

To design ρ , we first find the boundary conditions by considering the commutator $[H(t), I(t)]$ at $t = 0$ and $t = t_f$. For $t = 0$,

$$[H(0), I(0)] = \left[\frac{p^2}{2m} + \frac{1}{2}m\omega^2(0)x^2, \frac{1}{2m} [\rho(0)p - m\dot{\rho}(0)x]^2 + \frac{1}{2}m\omega_0^2 \left(\frac{x}{\rho(0)} \right)^2 \right]. \quad (2.72)$$

If we choose $\rho(0) = 1$, we obtain

$$[H(0), I(0)] = \left[\frac{p^2}{2m} + \frac{1}{2}m\omega_0^2 x^2, \frac{1}{2m} [p - m\dot{\rho}(0)x]^2 + \frac{1}{2}m\omega_0^2 x^2 \right], \quad (2.73)$$

and choosing $\dot{\rho}(0) = 0$ gives $[H(0), I(0)] = 0$. From Eq. (2.64) it follows that $\ddot{\rho}(0) = 0$. In summary, for $t = 0$ we have

$$\rho(0) = 1, \quad \dot{\rho}(0) = 0, \quad \ddot{\rho}(0) = 0. \quad (2.74)$$

In a similar manner we obtain the boundary conditions for $t = t_f$,

$$\rho(t_f) = \gamma = \sqrt{\frac{\omega_0}{\omega_f}}, \quad \dot{\rho}(t_f) = 0, \quad \ddot{\rho}(t_f) = 0. \quad (2.75)$$

Note that for this example the time-dependent average energy can be calculated analytically, and the boundary conditions derived here are equivalent to minimising the time-dependent average energy [72].

We are now free to choose any ansatz for $\rho(t)$ that satisfies the boundary conditions in Eq. (2.74) and Eq. (2.75). We will use a polynomial ansatz from [72],

$$\rho(t) = 6(\gamma - 1)s^5 - 15(\gamma - 1)s^4 + 10(\gamma - 1)s^3 + 1, \quad (2.76)$$

where $s = t/t_f$. Then using Eq. (2.64) we obtain

$$\omega^2(t) = \frac{\omega_0^2}{\rho^4} - \frac{\ddot{\rho}}{\rho}. \quad (2.77)$$

In Fig. 2.2, $\omega^2(t)/\omega_0^2$ is shown for several different final times t_f , using experimentally realistic parameters from [72]. We now compare the performance of the invariant-based inverse engineered (IBIE) $\omega(t)$ to an adiabatic protocol given by

$$\omega_a(t) = \omega_0 + (\omega_f - \omega_0) \frac{t}{t_f}. \quad (2.78)$$

For both the adiabatic and IBIE protocols we evaluate the fidelity

$$F = |\langle \psi_T | U(t_f, 0) \psi_0 \rangle|^2, \quad (2.79)$$

where $U(t_f, 0)$ is the time evolution operator, $|\psi_0\rangle$ is the initial state (the groundstate of a harmonic trap with angular frequency ω_0) and $|\psi_T\rangle$ is the

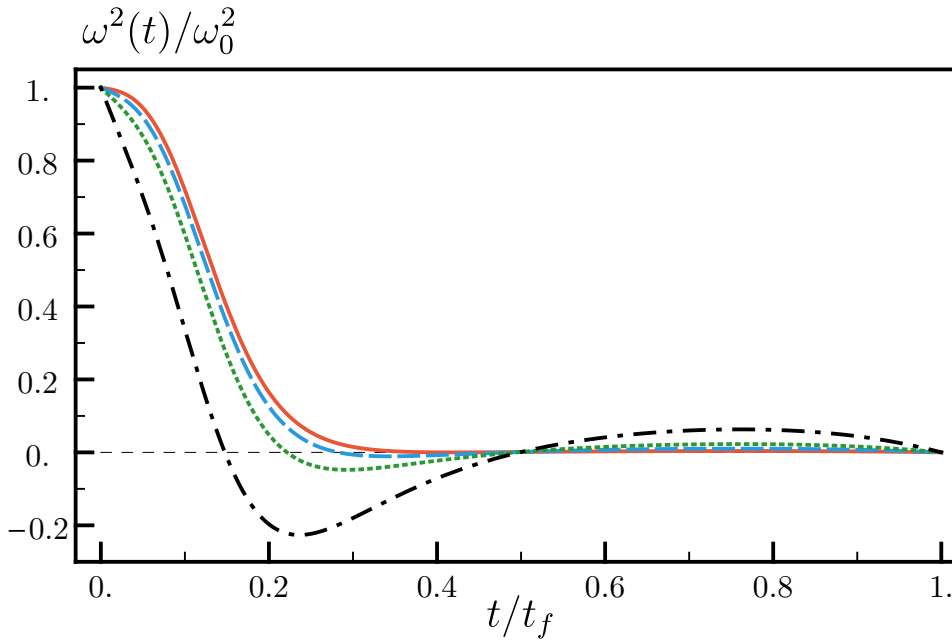


FIGURE 2.2: Examples of $\omega^2(t)/\omega_0^2$ using $\omega_0 = 250 \times 2\pi$ Hz, $\omega_f = 2.5 \times 2\pi$ Hz, $\gamma = 10$, with final times t_f : $t_f = 25$ ms (solid-red line), $t_f = 15$ ms (dashed-blue line), $t_f = 10$ ms (dotted-green line), $t_f = 6$ ms (dash-dotted black line).

target state (the groundstate of a harmonic trap with angular frequency ω_f). We set $\omega_0 = 250 \times 2\pi$ Hz and $\omega_f = 2.5 \times 2\pi$ Hz, which gives $\gamma = 10$. These values have been used in cold atom clock experiments [72, 73]. The results for different expansion times t_f are shown in Fig. 2.3, where the IBIE protocol (solid blue) gives perfect fidelity while the adiabatic scheme (dashed red) only achieves high fidelity for larger expansion times. To achieve a fidelity of $F = 0.99$, the adiabatic protocol requires $t_f > 9$ s, while in principle the IBIE scheme can give perfect fidelity for an arbitrary t_f . In practice a given experimental configuration will have constraints, for example limited available laser power. For very fast expansion times with $t_f < 2.5$ ms, the invariant-base STA schemes considered in Eq. (2.77) produces a potential that is repulsive over a portion of the expansion time. This is not a major obstacle, as in many practical settings repulsive potentials can be implemented [72].

Fast expansion and compression using the invariant-based inverse engineering approach outlined here has also been experimentally demonstrated using a

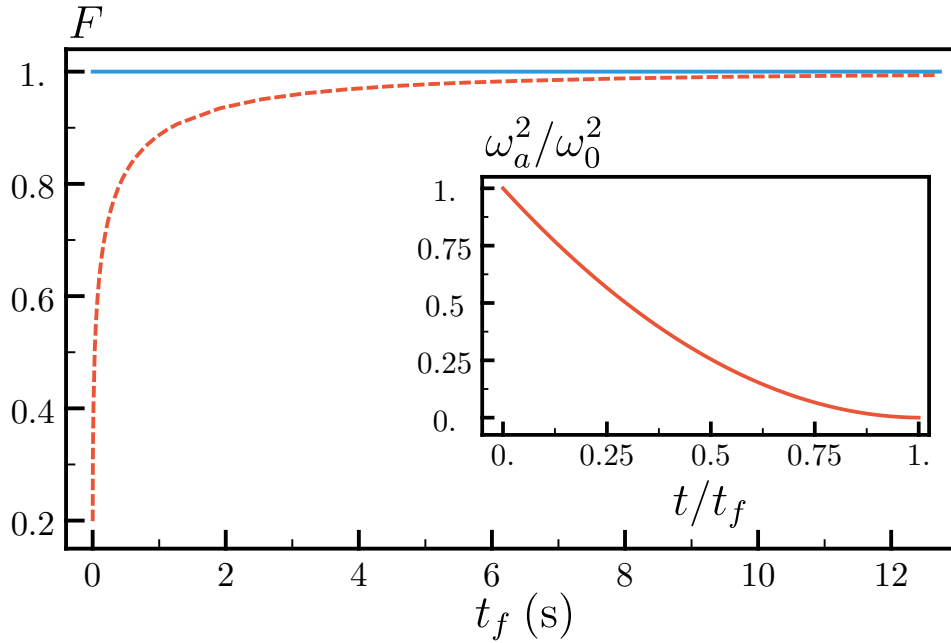


FIGURE 2.3: Fidelity versus expansion time t_f (in seconds), using the STA scheme from Eq. (2.77) (solid blue) and adiabatic scheme from Eq. (2.78) (dashed-red). Inset: Example of the adiabatic scheme from Eq. (2.78).

one dimensional Bose gas [74] and a Fermi gas [75].

Fast harmonic trap transport via Lewis-Riesenfeld invariants

We now consider harmonic trap transport, with Hamiltonian

$$H = \frac{p^2}{2m} + \frac{1}{2}m\omega_0^2 [x - q_0(t)]^2, \quad (2.80)$$

where ω_0 is the angular frequency of the harmonic trap, m is the mass of the particle and $q_0(t)$ is the transport trajectory of the potential minimum. We assume a transport distance of length d , giving boundary conditions for the trajectory $q_0(0) = 0$ and $q_0(t_f) = d$. This potential is in the Lewis-Leach family

(Eq. (2.62)), and we set $\rho = 1$, $f(t) = \frac{1}{2}m\omega_0^2q_0(t)^2$ and $F(t) = m\omega_0^2q_0(t)$ giving

$$\begin{aligned} V(x, t) &= \frac{1}{2}m\omega_0^2x^2 - m\omega_0^2q_0(t)x + \frac{1}{2}m\omega_0^2q_0(t)^2, \\ &= \frac{1}{2}m\omega_0^2[x - q_0(t)]^2. \end{aligned} \quad (2.81)$$

Note that the purely time-dependent term $f(t)$ is physically irrelevant, since it only contributes a global phase to the dynamics.

As $\rho = 1$, we need only consider the auxiliary equation Eq. (2.65),

$$\frac{\ddot{q}_c}{\omega_0^2} + q_c = q_0(t). \quad (2.82)$$

To determine boundary conditions on $q_c(t)$, we again consider $[H(t), I(t)]$ at $t = 0$ and $t = t_f$. For $t = 0$,

$$\begin{aligned} [H(0), I(0)] &= \frac{1}{2} \left[\frac{p^2}{m} + m\omega_0^2 [x - q_0(0)]^2, \frac{1}{m} [p - m\dot{q}_c(0)]^2 + m\omega_0^2 [x - mq_c(0)]^2 \right] \\ &= \frac{1}{2} \left[\frac{p^2}{m} + m\omega_0^2x^2, \frac{1}{m} [p - m\dot{q}_c(0)]^2 + m\omega_0^2 [x - mq_c(0)]^2 \right], \end{aligned} \quad (2.83)$$

hence $q_c(0) = \dot{q}_c(0) = 0$. Then from Eq. (2.65) we must have that $\ddot{q}_c(0) = 0$. In a similar manner we obtain the boundary conditions for $t = t_f$. We also enforce that the trap is at rest at $t' = 0, t_f$ by setting $\dot{q}_0(t') = \ddot{q}_0(t') = 0$, and by using Eq. (2.65) we therefore have that $q_c^{(3)}(t') = q_c^{(4)}(t') = 0$. In summary $q_c(t)$ must satisfy $q_c^{(3)}(t') = q_c^{(4)}(t') = 0$ for $t' = 0, t_f$.

Now we can choose any $q_c(t)$ that satisfies these boundary conditions and inverse engineer the trap trajectory $q_0(t)$ using Eq. (2.65), i.e. we solve

$$\ddot{q}_c(t) + \omega_0^2q_c(t) = \frac{\ddot{q}_0(t)}{m}, \quad (2.84)$$

for $q_0(t)$. This again highlights the great freedom that inverse engineering using

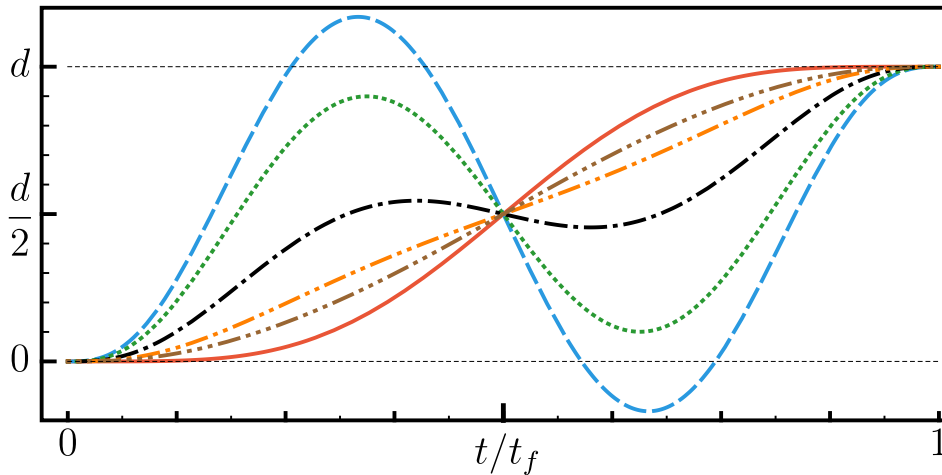


FIGURE 2.4: Example of $q_c(t)$ (solid blue line). Examples of $q_0(t)$; $t_f = 3.0\omega_0$ (dot-dashed black), $t_f = 3.5\omega_0$ (double dot-dashed purple), $t_f = 5.0\omega_0$ (triple dot-dashed brown), $t_f = 7.5\omega_0$ (4 dot-dashed green), $t_f = 10.0\omega_0$ (5 dot-dashed red), $t_f = 15.0\omega_0$ (6 dot-dashed orange). As t_f increases, q_0 approaches q_c .

L.R. invariants allows when designing control protocols. We choose a polynomial ansatz for $q_c(t)$,

$$q_c(t) = ds^5 (70s^4 - 315s^3 + 540s^2 - 420s + 126), \quad (2.85)$$

with $s = t/t_f$. Examples of $q_c(t)$ and $q_0(t)$ are shown in Fig. 2.4. Note that for $t_f \lesssim 3.2\omega_0$, $q_0(t)$ may move the trap beyond the transport distance d during transport. There are strategies to design $q_0(t)$ that satisfy more restraints, for example minimisation of time-averaged energy or bounded maximal distance during transport [72].

As an example, we compare the IBIE derived $q_0(t)$ with an adiabatic linear-ramp trajectory given by

$$q_{0,a}(t) = d \frac{t}{t_f}, \quad (2.86)$$

where d is the transport distance. We use numerical values from an atom

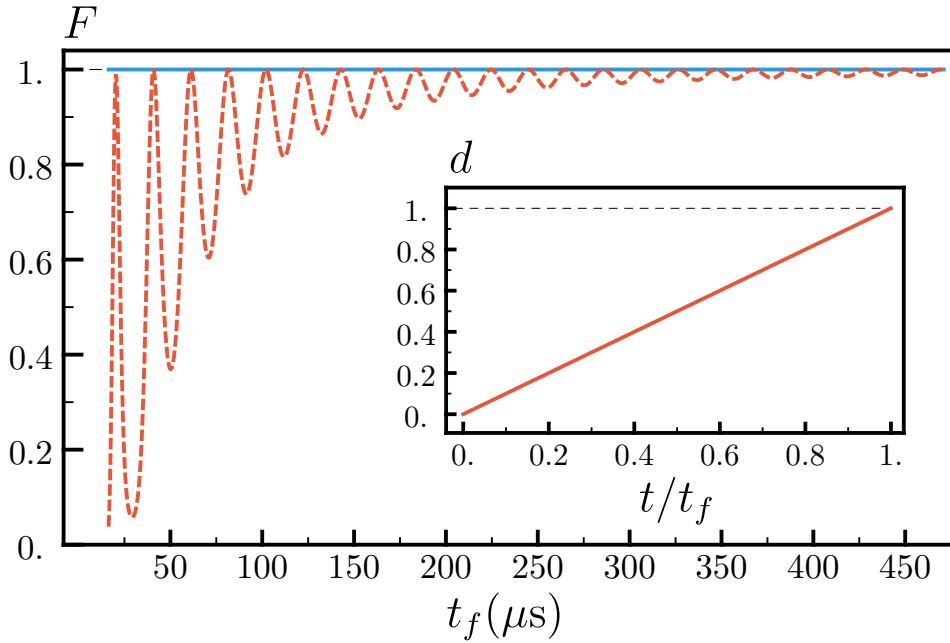


FIGURE 2.5: Fidelity vs. transport time t_f for an adiabatic scheme $q_{0,a}(t)$ and IBIE scheme q_0 . Inset: Adiabatic linear ramp transport scheme $q_{0,a}(t)$.

transport experiment using an optical lattice [76], where a ^{133}Cs atom was transported over a distance of one lattice site. This corresponds with a transport distance of $d = 10.9944\sigma$, where $\sigma = \sqrt{\hbar/m\omega_0}$, $\omega_0 = 0.3$ Mhz and m is the mass of a ^{133}Cs atom. The fidelity using the IBIE scheme (solid blue) and adiabatic ramp (dashed-red line) is shown in Fig. 2.5. The fidelity for the adiabatic ramp is perfect for times that are multiples of $2\pi/\omega_0$, and are the result of the wavepacket motion within the potential producing the correct transport. While the fidelity at these times is high, this protocol is inherently sensitive to noise since it requires precise transport times to achieve perfect fidelity. In contrast, the IBIE scheme produces perfect fidelity for all transport times and can be further optimised against anharmonicities and with different experimental constraints [77, 78].

2-level population inversion using Lewis-Riesenfeld invariants

The two-level system is one of the simplest quantum models and has applications throughout quantum physics; from a spin half particle in a magnetic field to the semi-classical coupling of two atomic levels with a laser. We now use invariant-based inverse engineering to achieve population inversion in a two-level system, where we transfer an initial state $|\Psi(0)\rangle$ to a target state $|\Psi(t_f)\rangle$ in a given time t_f , with

$$|\Psi(0)\rangle = \begin{pmatrix} 1 \\ 0 \end{pmatrix} = |1\rangle, \quad |\Psi(t_f)\rangle = \begin{pmatrix} 0 \\ 1 \end{pmatrix} = |2\rangle. \quad (2.87)$$

We consider the Hamiltonian

$$H_0(t) = \frac{\hbar}{2} \begin{pmatrix} -\Delta(t) & \Omega_R - i\Omega_I(t) \\ \Omega_R + i\Omega_I(t) & \Delta(t) \end{pmatrix}. \quad (2.88)$$

This Hamiltonian can model a two-level system in coherent laser light [22], where in the laser-adapted interaction picture, $\Omega(t) = \Omega_R - i\Omega_I(t)$ is the complex Rabi frequency where Ω_R, Ω_I are the real and imaginary parts respectively and $\Delta(t)$ is the time-dependent detuning between the laser and transition frequencies.

There is a known invariant for H_0 given by [79],

$$I(t) = \frac{\hbar}{2}\mu \begin{pmatrix} \cos[\Theta(t)] & e^{-i\alpha(t)} \sin[\Theta(t)] \\ e^{i\alpha(t)} \sin[\Theta(t)] - & \cos[\Theta(t)] \end{pmatrix}, \quad (2.89)$$

where μ is an arbitrary constant with units of frequency (since $I(t)$ must have units of energy), and

$$\dot{\Theta} = \Omega_I \cos(\alpha) - \Omega_R \sin(\alpha), \quad (2.90)$$

$$\dot{\alpha} = -\Delta - \cot(\Theta) [\Omega_R \cos(\alpha) + \Omega_I \sin(\alpha)]. \quad (2.91)$$

The eigenvectors of $I(t)$ (Eq. (2.89)) are

$$|\phi_+(t)\rangle = \begin{pmatrix} \cos(\Theta/2) e^{-i\alpha(t)/2} \\ \sin(\Theta/2) e^{i\alpha(t)/2} \end{pmatrix}, |\phi_-(t)\rangle = \begin{pmatrix} \sin(\Theta/2) e^{-i\alpha(t)/2} \\ -\cos(\Theta/2) e^{i\alpha(t)/2} \end{pmatrix}, \quad (2.92)$$

with eigenvalues $\pm\hbar\mu/2$. A general solution of the Schrödinger equation $|\Psi(t)\rangle$ can then be written as a linear combination,

$$|\Psi(t)\rangle = c_+ e^{i\kappa_+(t)} |\phi_+(t)\rangle + c_- e^{i\kappa_-(t)} |\phi_-(t)\rangle, \quad (2.93)$$

where c_{\pm} are constants and κ_{\pm} are the Lewis-Riesenfeld phases satisfying

$$\dot{\kappa}_{\pm} = \frac{1}{\hbar} \langle \phi_{\pm} | i\hbar \frac{\partial}{\partial t} - H_0 | \phi_{\pm} \rangle. \quad (2.94)$$

Particular solutions are

$$|\Psi(t)\rangle = |\phi_+(t)\rangle e^{-i\gamma(t)/2} = e^{-i\gamma/2} \begin{pmatrix} \cos[\Theta/2] e^{-i\alpha/2} \\ \sin[\Theta/2] e^{i\alpha/2} \end{pmatrix}, \quad (2.95)$$

and the orthogonal solution that satisfies $\langle \Psi_{\perp} | \Psi \rangle = 0$,

$$|\Psi_{\perp}(t)\rangle = |\phi_-(t)\rangle e^{i\gamma(t)/2} = e^{i\gamma/2} \begin{pmatrix} \sin[\Theta/2] e^{-i\alpha/2} \\ -\cos[\Theta/2] e^{i\alpha/2} \end{pmatrix}, \quad (2.96)$$

with $\gamma = 2\kappa_{\pm}$. From Eq. (2.94) we obtain

$$\dot{\gamma} = \frac{1}{\sin(\Theta)} [\Omega_R \cos(\alpha) + \Omega_I \sin(\alpha)]. \quad (2.97)$$

To transfer the population from $|\Psi(0)\rangle = |1\rangle$ to $|\Psi(t_f)\rangle = |2\rangle$, we require $\Theta(0) = 0$ and $\Theta(t_f) = \pi$ which gives

$$|\Psi(0)\rangle = e^{i\gamma(0)/2} \begin{pmatrix} e^{-i\alpha(0)/2} \\ 0 \end{pmatrix}, \quad |\Psi(t_f)\rangle = e^{i\gamma(t_f)/2} \begin{pmatrix} 0 \\ e^{-i\alpha(t_f)/2} \end{pmatrix}, \quad (2.98)$$

where the populations are unaffected by global phase terms. We now assume that $\alpha(t)$, $\gamma(t)$ and $\Theta(t)$ are given (they must satisfy Eq. (2.90), and Eq. (2.97)).

Then by inverting Eq. (2.90) and Eq. (2.97), we obtain

$$\begin{aligned} \Omega_R &= \cos(\alpha) \sin(\Theta) \dot{\gamma} - \sin(\alpha) \dot{\Theta}, \\ \Omega_I &= \sin(\alpha) \sin(\Theta) \dot{\gamma} + \cos(\alpha) \dot{\Theta}, \\ \Delta &= -\cos(\Theta) \dot{\gamma} - \dot{\alpha}. \end{aligned} \quad (2.99)$$

Thus if α , γ and Θ are chosen with appropriate boundary conditions, perfect population inversion can be engineered for a given time t_f using the potentials described by Eq. (2.99). There is considerable freedom in choosing these functions, and in the following example we choose a real Rabi frequency ($\Omega_I = 0$) and the following functions also minimise systematic error in the Rabi frequency [79]

$$\begin{aligned} \theta(t) &= \pi \frac{t}{t_f}, \\ \alpha(t) &= -\text{ArcCot} [4 \sin(\theta^3)], \\ \gamma(t) &= 2\theta(t) - \sin(2\theta). \end{aligned} \quad (2.100)$$

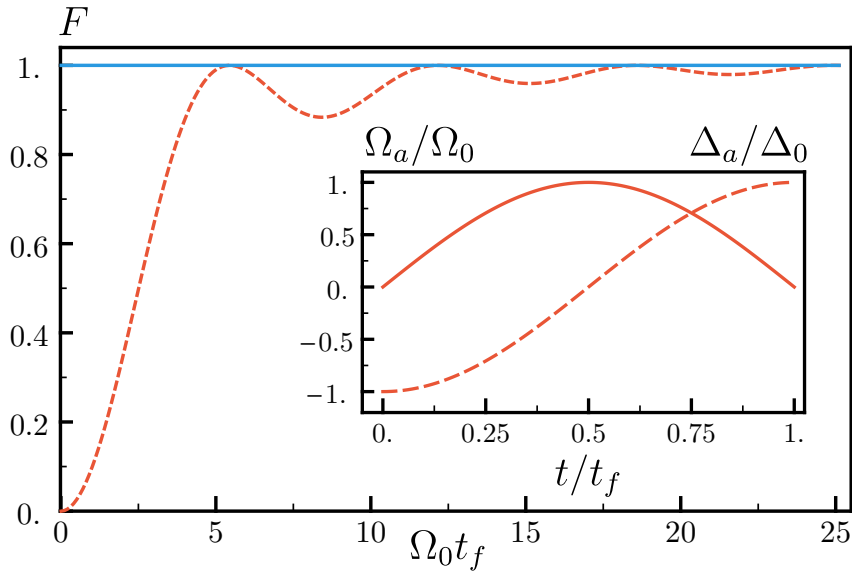


FIGURE 2.6: Fidelity for IBIE (solid-blue) and RAP (dashed-red) protocols, with $\Omega_0 = \Delta_0$ and unit of time Ω_0^{-1} . Inset: Examples of Ω_a (solid red) and Δ_a (dashed red) from Eq. (2.101).

As a comparison, consider the standard rapid adiabatic protocol with $\Omega_I = 0$,

$$\begin{aligned}\Omega_a &= \Omega_0 \sin\left(\frac{\pi t}{t_f}\right), \\ \Delta_a &= -\Delta_0 \cos\left(\frac{\pi t}{t_f}\right).\end{aligned}\tag{2.101}$$

The fidelity for the two schemes is shown in Fig. 2.6, with the IBIE protocol giving perfect fidelity while the RAP scheme needs longer t_f to achieve high fidelities.

2.3 Numerical Methods

While we design the control schemes in this thesis analytically, we use numerical simulation of the Schrödinger equation to evaluate the fidelity and robustness of the designed schemes. In this section we describe some core numerical methods that were used in this thesis.

2.3.1 Operator splitting

Operator splitting is a general method for numerically solving differential equations [80]. In this thesis we apply operator splitting to the Schrödinger equation,

$$i\hbar \frac{\partial}{\partial t} |\psi\rangle = \mathcal{H} |\psi\rangle, \quad (2.102)$$

where $\mathcal{H} = T_K + V$ is the Hamiltonian of the system and $T_K = -(\hbar^2/2m)\nabla^2$ is the kinetic energy operator and V is the potential energy operator. The system starts in a known initial state $|\psi_0\rangle$ at $t = 0$, and our goal is to calculate the final state of the system $|\psi_{t_f}\rangle$ at $t = t_f$. In this thesis we are concerned with time-dependent potentials, with the time dynamics of the system described by the time-ordered time-evolution operator ([81])

$$\mathcal{U}(t_f, 0) = \mathcal{T} \exp \left[-\frac{i}{\hbar} \int_0^{t_f} ds \mathcal{H}(s) \right], \quad (2.103)$$

where $|\psi_{t_f}\rangle = \mathcal{U}(t_f, 0) |\psi_0\rangle$ and \mathcal{T} indicates time ordering. To simulate the dynamics we numerically implement $\mathcal{U}(t_f, 0)$ using the split operator method. We first discretise the time interval $[0, t_f]$ into N steps of Δt , and consider \mathcal{U} over a single step of $\Delta t = t_f/N$, which we assume are small enough such that H does not vary significantly over Δt . Using a perturbative approach, \mathcal{U} can be approximated over Δt by ([81])

$$\begin{aligned} \mathcal{U}(t + \Delta t, t) &= \mathcal{T} \exp \left[-\frac{i}{\hbar} \int_t^{t+\Delta t} ds \mathcal{H}(s) \right] \\ &= + \left(-\frac{i}{\hbar} \right) \int_t^{t+\Delta t} dt_1 \mathcal{H}(t_1) \\ &+ \left(-\frac{i}{\hbar} \right)^2 \int_t^{t+\Delta t} dt_1 \int_t^{t_1} dt_2 \mathcal{H}(t_1) \mathcal{H}(t_2) + \dots \end{aligned} \quad (2.104)$$

For the first non-trivial term

$$\int_t^{t+\Delta t} dt_1 \mathcal{H}(t_1) = \int_t^{t+\Delta t} dt_1 [T_K + V(t_1)] = \Delta t T_K + \int_t^{t+\Delta t} dt_1 V(t_1), \quad (2.105)$$

and the integral of the potential can be approximated using the Midpoint Rule (see [80] for details)

$$\int_t^{t+\Delta t} dt_1 V(t_1) = \Delta t V_{\text{mid}} + \mathcal{O}(\Delta t^3), \quad (2.106)$$

where $V_{\text{mid}} = [V(t) + V(t + \Delta t)]/2$. The second integral in Eq. (2.104) becomes

$$\int_t^{t+\Delta t} dt_1 \int_t^{t_1} dt_2 [T_K^2 + V(t_1)T_K + T_K V(t_2) + V(t_1)V(t_2)]. \quad (2.107)$$

The first term in Eq. (2.107) simply becomes $(\Delta t T_K)^2/2$. The second term in Eq. (2.107) can be approximated

$$\begin{aligned} \int_t^{t+\Delta t} dt_1 \int_t^{t_1} dt_2 V(t_1) T_K &= T_K \int_t^{t+\Delta t} dt_1 (t_1 - t) V(t_1) \\ &= \frac{T_K}{2} \Delta t^2 V(t + \Delta t) + \mathcal{O}(\Delta t^3). \end{aligned} \quad (2.108)$$

Using Eq. (2.106) the third term in Eq. (2.107) becomes

$$\begin{aligned} \int_t^{t+\Delta t} dt_1 \int_t^{t_1} dt_2 T_K V(t_2) &= T_K \int_t^{t+\Delta t} dt_1 \frac{[V(t_1) + V(t)]}{2} (t_1 - t) + \mathcal{O}(\Delta t^3) \\ &= \frac{T_K}{2} \Delta t^2 V_{\text{mid}} + \mathcal{O}(\Delta t^3). \end{aligned} \quad (2.109)$$

Again using Eq. (2.106) twice (let $\tilde{V}(t_1) = V(t_1) [V(t_1) + V(t)] (t_1 - t) / 2$ in the second application), the last term in Eq. (2.107) becomes

$$\begin{aligned} \int_t^{t+\Delta t} dt_1 \int_t^{t_1} dt_2 V(t_1) V(t_2) &= \int_t^{t+\Delta t} dt_1 V(t_1) \frac{[V(t_1) + V(t)]}{2} (t_1 - t) + \mathcal{O}(\Delta t^3) \\ &= \frac{\Delta t^2}{4} [V(t + \Delta t)^2 + V(t + \Delta t)V(t)] + \mathcal{O}(\Delta t^3). \end{aligned} \quad (2.110)$$

Combining these terms we can write Eq. (2.104) up to third order in Δt as

$$\begin{aligned} \mathcal{U}(t + \Delta t, t) &= + \left(-\frac{i\Delta t}{\hbar} \right) (T_K + V_{\text{mid}}) \\ &\quad + \left(-\frac{i\Delta t}{\hbar} \right)^2 \frac{1}{2} [T_K^2 + V(t)T_K + T_K V(t) + V(t)^2] + \mathcal{O}(\Delta t^3). \end{aligned} \quad (2.111)$$

Now we notice that this is exactly what we obtain on expanding the series forms of the following exponential operators up to $\mathcal{O}(\Delta t^3)$, i.e.

$$\begin{aligned} \mathcal{U}(t + \Delta t, t) &= \exp\left(-\frac{i}{\hbar} \frac{\Delta t}{2} T_K\right) \exp\left(-\frac{i}{\hbar} \Delta t V_{\text{mid}}\right) \exp\left(-\frac{i}{\hbar} \frac{\Delta t}{2} T_K\right) \\ &\quad + \mathcal{O}(\Delta t^3). \end{aligned} \quad (2.112)$$

Thus Eq. (2.112) provides an approximation to the true time evolution with error of order Δt^3 . Thus choosing a large enough number of time steps N will allow us to numerically implement the time evolution operator to high precision. An estimate of the required N can be found by choosing N such that $\Delta t/\hbar V_{\text{mid}} \ll 2\pi$ and $\Delta t/\hbar T_K \ll 2\pi$. Note that Eq. (2.112) is a very useful way to approximate \mathcal{U} , since T_K and V have diagonal representations in the momentum and position bases respectively. Furthermore, transforming between the position and momentum bases can be implemented efficiently using the Fast Fourier Transform (FFT) and its inverse. Let \mathcal{F} represent the Fourier

transform, then the wavefunction after Δt will be well approximated by

$$\psi(x, t + \Delta t) \approx \left[\mathcal{F}^{-1} \exp\left(-\frac{i}{\hbar} \frac{\Delta t}{2} T_K\right) \mathcal{F} \exp\left(-\frac{i}{\hbar} \Delta t V_{\text{mid}}\right) \mathcal{F}^{-1} \exp\left(-\frac{i}{\hbar} \frac{\Delta t}{2} T_K\right) \mathcal{F} \right] \psi(x, t), \quad (2.113)$$

where transforming the wavefunction between the position and momentum basis allows the application of the exponential operators to be numerically calculated as a vector dot product, rather than a full matrix-vector operation.

There are also alternative and higher order decompositions of the time evolution operator [82], where the decomposition discussed here is used as an illustrative example. The question of the error of a given decomposition is an area of active research and depends on the exact system in question. Recently a more general approach to the question of decomposition error (often called Trotter error) has been developed in [83]. For more complicated situations than the simple Schrödinger equation simulation we consider here, the interplay of decomposition length and error bound can be significant when numerically simulating more complicated systems [83].

2.3.2 Imaginary time evolution

Imaginary time evolution is a very useful technique to find the ground state of a stationary Hamiltonian

$$\mathcal{H} = -\frac{\hbar^2}{2m} \nabla^2 + V(\vec{x}). \quad (2.114)$$

We choose an initial trial wave function

$$|\psi\rangle = \sum_k c_k |\phi_k\rangle \quad (2.115)$$

where $|\phi_k\rangle$ are the energy eigenstates of \mathcal{H} with ordered energy levels $E_0 < E_1 < \dots < E_k < \dots$, and we assume that there is some overlap between the trial wavefunction and the groundstate i.e. $c_0 \neq 0$. The time evolution of \mathcal{H} acting on $|\psi\rangle$ is given by $|\Psi(t)\rangle$, where

$$|\Psi(t)\rangle = \exp\left(-\frac{i}{\hbar}\mathcal{H}t\right)|\psi\rangle = \sum_k c_k \exp\left(-\frac{i}{\hbar}E_k t\right)|\phi_k\rangle,$$

since \mathcal{H} is time independent. Now we map $t \rightarrow it = \tau$, so that $\tau \in \mathbb{R}$ and obtain

$$\begin{aligned} |\Psi(\tau)\rangle &= \sum_k c_k \exp\left(-\frac{1}{\hbar}E_k \tau\right)|\phi_k\rangle \\ &= \alpha(\tau) \left\{ |\phi_0\rangle + \sum_{k \neq 0} \frac{c_k}{c_0} \exp\left[-\frac{1}{\hbar}(E_k - E_0)\tau\right] |\phi_k\rangle \right\}, \end{aligned} \quad (2.116)$$

where $\alpha(\tau) = c_0 \exp(-\frac{1}{\hbar}E_0 \tau)$. As τ increases, the sum term will tend towards $|\phi_0\rangle$ while $\alpha(\tau)$ tends exponentially to zero. When implementing this process numerically, we discretise time and we can counter the $\alpha(\tau)$ term's effect by renormalising the wavefunction after each imaginary time step. During the imaginary time evolution the energy states $|\phi_k\rangle$ decay at a rate proportional to their energy E_k . This means that if we can evolve $|\Psi(\tau)\rangle$ for long enough imaginary time, we will ensure that all other energy states will have decayed leaving only the ground state. Note that if the trial wave function has no overlap with the ground state $|\phi_0\rangle$, then this procedure cannot converge to the groundstate. In practice this is not a significant problem as long as we know approximately the form of the ground state (for systems in this thesis this is the case, for example the groundstate of any anharmonic trap is approximately the harmonic groundstate for sufficiently deep traps). When implementing this method numerically, it is useful to evolve two different trial wave functions and at each step measure their overlap. When the overlap approaches close to unity we know that both trial wave functions have approached the ground state. Furthermore, this the imaginary time evolution is easily implemented using the

split operator method.

2.3.3 The GRAPE algorithm

The GRAPE algorithm (gradient ascent pulse engineering) was first introduced in [5], where an iterative gradient ascent process was used to calculate optimal pulses for coupled spin systems. GRAPE was initially formulated for open systems, but for simplicity we describe it here for a closed quantum system.

The goal of GRAPE is to design a control pulse that takes an initial state $|\psi_0\rangle$ to a target state $|\psi_T\rangle$ in a given time t_f . We assume a Hamiltonian of the form

$$\mathcal{H} = \mathcal{H}_0 + \sum_{k=1}^M u_k(t) \mathcal{H}_k, \quad (2.117)$$

where \mathcal{H}_0 is the time-independent free evolution of the system and \mathcal{H}_k are constant. We now discretise the time evolution into N equal steps of duration Δt . For the j^{th} time step the Hamiltonian has M adjustable parameters $u_{k,j}$ that we assume are constant over Δt , i.e. $u_{k,j}(t) = u_{k,j}$ for $t_{j-1} < t < t_j$ with $j = 0, \dots, N$ and $k = 0, \dots, M$. This allows us to write the time evolution as a simple matrix exponential, with the time evolution during the j^{th} time step given by

$$U_j = \exp \left[-\frac{i}{\hbar} \Delta t \left(\mathcal{H}_0 + \sum_{k=1}^M u_{k,j} \mathcal{H}_k \right) \right]. \quad (2.118)$$

The final state after the full time evolution is

$$|\psi(t_f)\rangle = |\psi_N\rangle = U_N \dots U_1 |\psi_0\rangle. \quad (2.119)$$

We define a state transfer cost function

$$C = 1 - |\langle \psi_f | \psi_N \rangle|^2. \quad (2.120)$$

Now we calculate $\partial C/\partial u_{k,j}$ over the j^{th} time interval to first order in Δt ,

$$\begin{aligned} \frac{\partial C}{\partial u_{k,j}} &= -\frac{\partial}{\partial u_{k,j}} \left(\langle \psi_f | U_N \dots U_1 \psi_0 \rangle \langle \psi_0 | U_1^\dagger \dots U_N^\dagger \psi_f \rangle \right) \\ &= -\langle U_{j+1}^\dagger \dots U_N^\dagger \psi_f | \left(\frac{\partial U_j}{\partial u_{k,j}} \right) U_{j-1} \dots U_1 \psi_0 \rangle \langle \psi_f | \psi_N \rangle + c.c. \\ &= -2\text{Re} \left[\langle U_{j+1}^\dagger \dots U_N^\dagger \psi_f | \left(\frac{\partial U_j}{\partial u_{k,j}} \right) U_{j-1} \dots U_1 \psi_0 \rangle \langle \psi_f | \psi_N \rangle \right] \end{aligned} \quad (2.121)$$

To calculate the derivative one can follow the approach in [5], by first letting $u_{k,j} \mapsto u_{k,j} + \delta u_{k,j}$ and using the formula ¹

$$\frac{d}{dx} e^{A+xB} \Big|_{x=0} = \frac{e^A}{\Delta t} \int_0^{\Delta t} e^{A\tilde{\tau}} B e^{-A\tilde{\tau}} d\tilde{\tau}, \quad (2.122)$$

with $\tilde{\tau} = t \Delta t$ and

$$A = -\frac{i}{\hbar} \Delta t \left(\mathcal{H}_0 + \sum_{k=1}^M u_{k,j} \mathcal{H}_k \right), \quad B = -\frac{i}{\hbar} \Delta t \mathcal{H}_k, \quad x = \delta u_{j,k}. \quad (2.123)$$

Then we have

$$\frac{\partial U_j}{\partial u_{k,j}} = -\frac{i}{\hbar} \Delta t \bar{\mathcal{H}}_k U_j + \mathcal{O}(\Delta t^2), \quad (2.124)$$

with

$$\bar{\mathcal{H}}_k = \frac{1}{\Delta t} \int_0^{\Delta t} U_j(\tau) \mathcal{H}_k U_j(-\tau) d\tau, \quad (2.125)$$

and

$$U_j(\tau) = \exp \left[-\frac{i}{\hbar} \tau \left(\mathcal{H}_0 + \sum_{k=1}^M u_{k,j} \mathcal{H}_k \right) \right]. \quad (2.126)$$

¹Eq. (2.122) has several independent origins, the earliest is found in [84] and then in [85]. Later the result was made rigorous in [86] and [87]. Eq. (2.122) has been generalised to ordered exponentials in [88].

If we consider the norm $\|A\| = \Delta t \|\mathcal{H}_0 + \sum_k u_{k,j} \mathcal{H}_k\| \lll 1$, then for $\Delta t \lll \|\mathcal{H}_0 + \sum_k u_{k,j} \mathcal{H}_k\|^{-1}$ we can approximate $\bar{\mathcal{H}}_k \approx \mathcal{H}_k$. Thus Eq. (2.121) becomes

$$\frac{\partial C}{\partial u_{k,j}} = -2\Delta t \operatorname{Re} \left[\langle U_{j+1}^\dagger \dots U_N^\dagger \psi_f | i \mathcal{H}_k U_j U_{j-1} \dots U_1 \psi_0 \rangle \langle \psi_N | \psi_f \rangle \right]. \quad (2.127)$$

There is a simpler way to derive the same result using time-dependent perturbation theory. If we consider the time evolution over Δt , and set $\mathcal{H} = H_A + \delta\mathcal{H}_k$ where

$$\mathcal{H}_A = \mathcal{H}_0 + \sum_{l=1}^M u_l \mathcal{H}_l, \quad (2.128)$$

and $k \in \{1, \dots, M\}$. We define an interaction picture by

$$|\tilde{\Psi}(t)\rangle = U^{(A)\dagger}(t, 0) |\Psi(t)\rangle, \quad (2.129)$$

where $U^{(A)}(t, 0)$ is the time-evolution operator for the system with Hamiltonian $H_A(t)$. We then have

$$\frac{d}{dt} |\tilde{\Psi}(t)\rangle = -\frac{i}{\hbar} U^{(A)\dagger}(t, 0) \delta\mathcal{H}_k U^{(A)}(t, 0) |\tilde{\Psi}(t)\rangle. \quad (2.130)$$

Considering the integral form of this equation over $[t, t + \Delta t]$, and using that \mathcal{H}_k is time independent, gives

$$U(t + \Delta t, t) = U^{(A)}(t + \Delta t, t) - \frac{i\delta\mathcal{H}_k}{\hbar} \int_t^{t+\Delta t} dt_1 U^{(A)}(t_1, t) + \dots \quad (2.131)$$

where we have only written the first iteration of solving the integral equation for the time evolution operator U . Note that $U^{(A)} = U_j$ is time independent and the first time integral can be done trivially. Now we take the derivative

with respect to δ to obtain

$$\frac{\partial}{\partial \delta} U(t + \Delta t, t) \approx -\frac{i\mathcal{H}_k \Delta t}{\hbar} U_j, \quad (2.132)$$

which is equivalent to Eq. (2.124) (after the approximation $\overline{\mathcal{H}}_k \approx \mathcal{H}_k$).

For closed quantum systems there is an efficient way to implement the gradient calculation:

Step 1: Using current control parameters $u_{k,j}$, evolve $|\psi_0\rangle \rightarrow |\psi_N\rangle$. If the fidelity $|\langle \psi_T | \psi_N \rangle|^2 > c$, we are done (where c is a threshold fidelity we choose).

Step 2: Evolve backwards $|\psi_N\rangle$ and $|\psi_f\rangle$ simultaneously using U_N^\dagger a single Δt step and calculate all k derivatives using Eq. (2.127), to give the gradient for $j = 1$.

Step 3: Repeat the previous for all time steps, calculating the gradient for each j .

Step 4: Update the control parameters $u_{k,j} \rightarrow u_{k,j} + \epsilon \frac{\partial C}{\partial u_{k,j}}$, with a chosen small ϵ (in practice a simple line search can be used, or extended versions see [80]). Return to step 1.

This algorithm is naturally suited to implementation on a GPU, since the backwards in time evolution is easily parallelised. For example in step 2, this means we can evolve both $|\psi_N\rangle$ and $|\psi_f\rangle$ backwards at the same time. On the GPU the FFT of complex vectors is very fast, and since we are considering a closed system the evolution is unitary, and the previous mentioned split-operator method works very efficiently on the GPU. Note that for closed systems the memory requirement is small, since we only need to hold two states in memory during the gradient calculation process.

Chapter 3

Quantum control via enhanced shortcuts to adiabaticity

3.1 Overview

In this chapter we develop an analytic extension to STA called enhanced shortcuts to adiabaticity (eSTA). The eSTA method provides control schemes for Hamiltonians that have no known STA control method, by providing an analytical correction to existing STA protocols. This correction can be easily calculated, and the resulting protocols can be outside the class of STA schemes. We demonstrate the effectiveness of the method in both finite and infinite dimensional settings using three distinct cases: manipulation of an internal atomic state beyond the rotating-wave approximation, transport of a neutral atom in an optical Gaussian trap, and transport of two trapped ions in an anharmonic trap.

This chapter is based on the following publication:

C. Whitty, A. Kiely and A. Ruschhaupt,

Enhanced shortcuts to adiabaticity,

[Phys. Rev. Research 2, 023360 \(2020\)](#).

3.2 Introduction

The development of quantum technologies for a wide variety of applications is a rapidly growing field [89]. However, a common roadblock is the requirement for fast and robust control of fragile quantum states, which is critical to exploiting any quantum advantage. The process must be fast to avoid long interaction times with the external environment (decoherence) and stable to avoid accumulation of errors. These problems have been addressed by a number of distinct techniques such as adiabatic methods [9], composite pulses [90–92], numerical optimal control [5, 7, 93, 94] and shortcuts to adiabaticity [10, 11].

Shortcuts to adiabaticity (STA) are analytical methods to design the time dependence of the Hamiltonian to ensure effective adiabatic state evolution in finite time. STA methods have the advantage of providing physical insight into the control process as well as constructing a whole class of protocols that achieve the desired result. In combination with perturbation theory, the optimal protocol in this class can be found which is most stable regarding a relevant type of noise or imperfection [79, 95, 96]. There has also been work to improve protocols in a non-perturbative manner [37, 97], using variational methods [45, 49] and in combination with numerical optimal control [46, 98–100].

STA methods have been used to control a variety of Hamiltonians such as harmonic oscillator potentials [72, 77, 101] and two-level [79, 96], three-level [102, 103] and four-level [104] systems. They have been utilised experimentally for trapped ions [105], superconducting qubits [106, 107], nitrogen-vacancy centers [108, 109], ultracold atoms [25] and Bose-Einstein condensates [42]. However there are still many Hamiltonians which are not tractable with standard STA techniques. Our new procedure is intended to deal with such cases.

In this chapter we provide an analytical enhancement to STA protocols inspired by techniques of numerical optimal control, termed *enhanced shortcuts*

to adiabaticity (eSTA). There are several key benefits. Firstly, the eSTA protocol provides higher fidelities than the STA protocol and may be outside the original class of STA protocols. This represents a significant improvement over previous methods based on optimisation inside the STA class [79]. Secondly, the resulting protocol is still completely analytical in nature, requiring no significant numerical computation or iterative procedure and therefore the resulting protocols can provide further physical insight. In addition, it is expected that eSTA protocols can also serve as good initial seeds for further numerical optimisation. As STA methods have also been applied beyond quantum systems [11], for example in optical waveguides [110–112], classical mechanical systems [33, 54, 113] and statistical physics [114], eSTA has a broad range of applicability and in principle can be applied beyond the scope of quantum control. In the following, we will outline the details of the eSTA method; the key result is summarised in Eq. (3.8). After this, we will demonstrate the flexibility of this approach by applying it to three different settings which are all ubiquitous in quantum technologies: population transfer in a two-level system beyond the rotating wave approximation [115–118], transport of a single neutral atom in an optical trap [119–121] and the transport of two trapped ions in an anharmonic trap [36, 122–125].

3.3 Formalism of eSTA

Consider a closed quantum system described by a Hamiltonian \mathcal{H}_μ , which we will refer to as the system Hamiltonian. Our goal is to change the Hamiltonian in time so that the system evolves from the initial state $|\Psi_0\rangle$ at $t = 0$ to the target state $|\Psi_T\rangle$ in a given total time t_f . The Schrödinger equation is $i\hbar\frac{\partial}{\partial t}|\Psi(t)\rangle = \mathcal{H}_\mu(\vec{\lambda}; t)|\Psi(t)\rangle$, where the value of μ fixes the form of the Hamiltonian and the time dependent control of the system parameters is characterised by $\vec{\lambda}$. The fidelity for this evolution is $F(\mu, \vec{\lambda}) = \left| \langle \Psi_T | U_{\mu, \vec{\lambda}}(t_f, 0) | \Psi_0 \rangle \right|^2$.

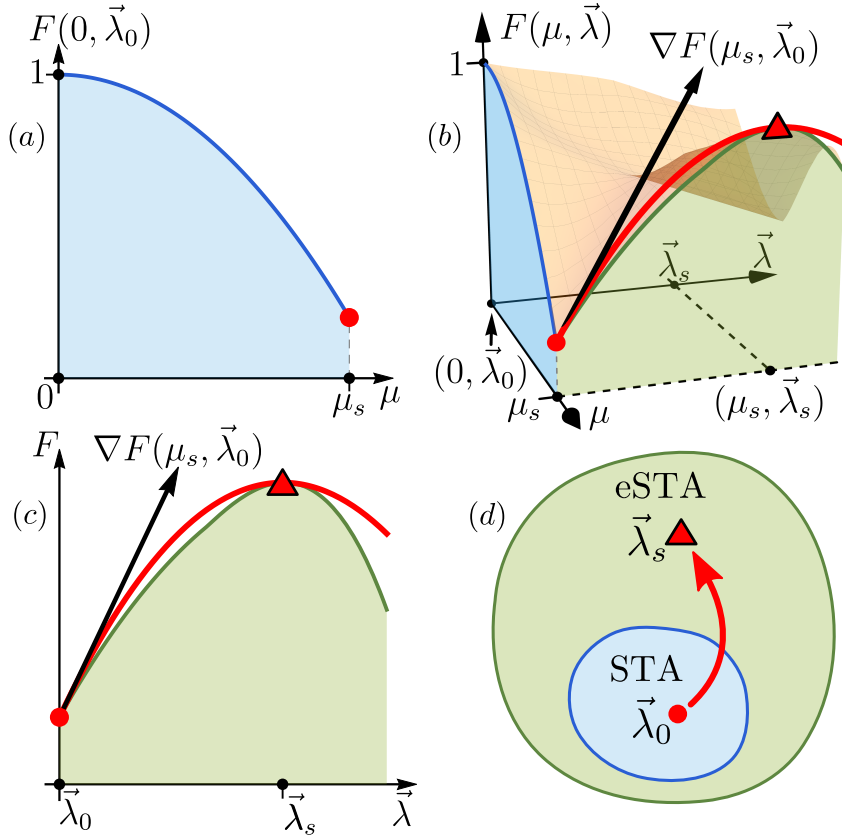


FIGURE 3.1: Schematic overview of eSTA: (a) Fidelity using the STA protocol $\vec{\lambda}_0$ as a function of the Hamiltonian parameterisation μ . Red dot indicates the fidelity at the point μ_s . (b) Surface diagram of the fidelity for different Hamiltonians μ and different control protocols $\vec{\lambda}$. The black arrow shows the gradient at $(\mu_s, \vec{\lambda}_0)$. The solid red line indicates the parabolic approximation with the red triangle located at its maximum. (c) Cross section of part (b), showing the fidelity for the system Hamiltonian as a function of the control parameterisation. (d) Set of control protocols using STA methods (blue, inner region) and using eSTA (green, outer region)

First the system Hamiltonian \mathcal{H}_μ (which is not easily dealt with using STA techniques) is approximated by an idealised, simpler Hamiltonian \mathcal{H}_0 where an STA method can be applied. The manipulations required for the STA protocol are parameterised by $\vec{\lambda}_0 \in \mathbb{R}^N$. Our goal is to find $\vec{\lambda}$ such that the fidelity of this chosen evolution under \mathcal{H}_μ is improved, where the method of improvement is motivated by the GRAPE algorithm [5, 126]. We now specify that the particular system we want to control has Hamiltonian $\mathcal{H}_{\mu=\mu_s}$, and that $\mathcal{H}_{\mu=0}$ is the approximate STA Hamiltonian. Clearly, just using the STA protocol that

was designed for the idealised Hamiltonian \mathcal{H}_0 does not give perfect fidelity for the system Hamiltonian \mathcal{H}_{μ_s} (see red dot in Fig. 3.1(a)). However, we assume that the difference between the system and idealised Hamiltonians μ_s is small. Hence, we also assume that using the STA protocol $\vec{\lambda}_0$ for the system Hamiltonian is close to optimal, see Fig. 3.1(b). In order to calculate how much and in what manner to alter the original STA scheme $\vec{\lambda}_0$, we calculate the gradient with respect to $\vec{\lambda}$ and assume that the fidelity behaves quadratically in the neighborhood of $(\mu_s, \vec{\lambda}_0)$, see Fig. 3.1(c).

The new control function parameterised by $\vec{\lambda}$ is given by $\vec{\lambda}_s = \vec{\lambda}_0 + \vec{\epsilon}$, where the correction is

$$\vec{\epsilon} \approx \frac{2 \left[1 - F(\mu_s, \vec{\lambda}_0) \right]}{\left| \nabla F(\mu_s, \vec{\lambda}_0) \right|} \frac{\nabla F(\mu_s, \vec{\lambda}_0)}{\left| \nabla F(\mu_s, \vec{\lambda}_0) \right|}, \quad (3.1)$$

and $\nabla = \nabla_{\vec{\lambda}}$ is the gradient with respect to $\vec{\lambda}$. Here, we have assumed the fidelity at the maximum of the parabola (see red triangle in Figs. 3.1(b) and 3.1(c)) is approximately one i.e. $F(\mu_s, \vec{\lambda}_0 + \vec{\epsilon}) \approx 1$.

To calculate $\vec{\epsilon}$ we must estimate the gradient and the value of the fidelity at $(\mu_s, \vec{\lambda}_0)$, (see red dot in Fig. 3.1). To derive these estimates, we assume that the initial state $|\Psi_0\rangle$ and the final target state $|\Psi_T\rangle$ are independent of the parameterisation μ . Since STA methods can be applied for the idealised Hamiltonian, the solutions $|\chi_n(t)\rangle$ are known (using Lewis-Riesenfeld invariants for example). Since $U_{0, \vec{\lambda}_0}(t_2, t_1)$ is the time-evolution for $\mu = 0$, we have that $|\chi_n(t)\rangle = U_{0, \vec{\lambda}_0}(t, 0)|\chi_n(0)\rangle$ and $U_{0, \vec{\lambda}_0}(t, s) = \sum_n |\chi_n(t)\rangle\langle\chi_n(s)|$. We assume $|\chi_0(0)\rangle = |\Psi_0\rangle$ and therefore $|\chi_0(t_f)\rangle = |\Psi_T\rangle$.

We now estimate the terms needed to calculate the correction, assuming that we can neglect higher order contributions in both μ and $\vec{\epsilon}$. We start with a series expansion $\mathcal{H}_{\mu}(\vec{\lambda}; t) = \sum_{n=0}^{\infty} \mu^n \mathcal{H}^{(n)}(\vec{\lambda}; t)$ where $\mathcal{H}^{(0)}(\vec{\lambda}; t) = \mathcal{H}_0(\vec{\lambda}; t)$. Using time-dependent perturbation theory [23], we construct a series expansion of the corresponding time-evolution operator $U_{\mu, \vec{\lambda}}(t_2, t_1) = \sum_{n=0}^{\infty} \mu^n U_{\vec{\lambda}}^{(n)}(t_2, t_1)$

where exact form of the first, second and third order can be found in Appendix 3.8.

From a series expansion of the fidelity in μ we get $F(\mu, \vec{\lambda}_0) = \sum_{n=0}^{\infty} \mu^n F^{(n)}$. The STA scheme works perfectly for the idealised Hamiltonian by construction, $F^{(0)} = 1$. For the higher orders, one gets (see Appendix 3.8 for details):

$$\begin{aligned} F^{(1)} &= 0, \\ F^{(2)} &= -\frac{1}{\hbar^2} \sum_{n=1}^{\infty} \left| \int_0^{t_f} dt \alpha_{n,0}^{(1)}(t) \right|^2, \\ F^{(3)} &\approx -\frac{2}{\hbar^2} \sum_{n=1}^{\infty} \text{Re} \left[\left(\int_0^{t_f} dt \alpha_{n,0}^{(1)}(t) \right)^* \left(\int_0^{t_f} dt \alpha_{n,0}^{(2)}(t) \right) \right], \end{aligned} \quad (3.2)$$

where we have defined $\alpha_{n,m}^{(j)}(t) = \langle \chi_n(t) | \mathcal{H}^{(j)}(\vec{\lambda}_0; t) | \chi_m(t) \rangle$. Using these results, the fidelity $F(\mu_s, \vec{\lambda}_0)$ can be approximated up to second order in μ_s as

$$F(\mu_s, \vec{\lambda}_0) \approx 1 - \frac{1}{\hbar^2} \sum_{n=1}^{\infty} \left| \int_0^{t_f} dt \left(\mu_s \alpha_{n,0}^{(1)}(t) + \mu_s^2 \alpha_{n,0}^{(2)}(t) \right) \right|^2 \approx 1 - \frac{1}{\hbar^2} \sum_{n=1}^{\infty} |G_n|^2, \quad (3.3)$$

where

$$G_n = \int_0^{t_f} dt \langle \chi_n(t) | \left[\mathcal{H}_S(\vec{\lambda}_0; t) - \mathcal{H}^{(0)}(\vec{\lambda}_0; t) \right] | \chi_0(t) \rangle, \quad (3.4)$$

and $\mathcal{H}_S = \mathcal{H}_{\mu_s}$. The gradient of the fidelity with respect to $\vec{\lambda}$ can be expanded in μ as $\nabla F(\mu, \lambda_0) = \sum_{n=0}^{\infty} \mu^n \vec{\mathcal{F}}^{(n)}$. The relevant orders are in Appendix 3.8,

$$\begin{aligned} \vec{\mathcal{F}}^{(0)} &= \vec{0} \\ \vec{\mathcal{F}}^{(1)} &= -\frac{2}{\hbar^2} \sum_{n=1}^{\infty} \text{Re} \left[\int_0^{t_f} dt \alpha_{n,0}^{(1)}(t) \int_0^{t_f} ds \vec{\beta}_{n,0}^{(0)}(s)^* \right], \\ \vec{\mathcal{F}}^{(2)} &\approx -\frac{2}{\hbar^2} \sum_{n=1}^{\infty} \text{Re} \left[\left(\int_0^{t_f} dt \vec{\beta}_{n,0}^{(1)}(t) \right)^* \left(\int_0^{t_f} dt \alpha_{n,0}^{(1)}(t) \right) \right. \\ &\quad \left. + \left(\int_0^{t_f} dt \vec{\beta}_{n,0}^{(0)}(t) \right)^* \left(\int_0^{t_f} dt \alpha_{n,0}^{(2)}(t) \right) \right], \end{aligned} \quad (3.5)$$

where we have defined $\vec{\beta}_{n,m}^{(j)}(t) = \langle \chi_n(t) | \nabla \mathcal{H}^{(j)}(\vec{\lambda}_0; t) | \chi_m(t) \rangle$. From these results, we get up to second order in μ_s that

$$\begin{aligned} \nabla F(\mu_s, \lambda_0) &\approx -\frac{2\mu_s}{\hbar^2} \sum_{n=1}^{\infty} \text{Re} \left\{ \int_0^{t_f} dt \left[\mu_s \alpha_{n,0}^{(1)}(t) + \mu_s^2 \alpha_{n,0}^{(2)}(t) \right] \right. \\ &\quad \left. \int_0^{t_f} ds \left[\vec{\beta}_{n,0}^{(0)}(s) + \mu_s \vec{\beta}_{n,0}^{(1)}(s) \right]^* \right\} \\ &\approx -\frac{2}{\hbar^2} \sum_{n=1}^{\infty} \text{Re} \left(G_n \vec{K}_n^* \right), \end{aligned} \quad (3.6)$$

where

$$\vec{K}_n = \int_0^{t_f} dt \langle \chi_n(t) | \nabla \mathcal{H}_S(\vec{\lambda}_0; t) | \chi_0(t) \rangle. \quad (3.7)$$

From Eq. (3.1), we finally arrive at the key result of the chapter, the analytical expression for the eSTA protocol

$$\vec{\lambda}_s \approx \vec{\lambda}_0 - \frac{\left(\sum_{n=1}^N |G_n|^2 \right) \left[\sum_{n=1}^N \text{Re} \left(G_n^* \vec{K}_n \right) \right]}{\left| \sum_{n=1}^N \text{Re} \left(G_n^* \vec{K}_n \right) \right|^2}, \quad (3.8)$$

where G_n is given by Eq. (3.4), K_n is given by Eq. (3.7), and we have truncated the infinite sums to the first N terms.

We underline that G_n and \vec{K}_n can be both easily calculated as only the Hamiltonians and the known solutions for the idealised Hamiltonian \mathcal{H}_0 are involved. Note that using the eSTA method provides protocols which are outside the class of STA schemes (see Fig. 3.1(d)) and so represents a significant improvement over previous perturbation based optimisation [79].

3.4 Population inversion without the Rotating-Wave-Approximation

As a first example, we consider the following system Hamiltonian

$$\mathcal{H}_S = \frac{\hbar}{2} \begin{pmatrix} -\delta(\vec{\lambda}; t) & \Omega^*(\vec{\lambda}; t) (1 + e^{-2i\omega t}) \\ \Omega(\vec{\lambda}; t) (1 + e^{2i\omega t}) & \delta(\vec{\lambda}; t) \end{pmatrix},$$

which generically appears in many areas of quantum technologies. A common setting is that of two atomic states which are coupled by a classical light source (e.g. a laser) where the Rabi frequency Ω depends on the light amplitude and the detuning δ depends on the light frequency ω .

The terms $e^{\pm 2i\omega t}$ are typically neglected, which is known as the ‘‘Rotating-wave-approximation’’ (RWA) [127]. Our idealised Hamiltonian \mathcal{H}_0 is then just \mathcal{H}_S where the terms $e^{\pm 2i\omega t}$ are set to zero.

While this approximation may work well for adiabatic methods, it will fail for fast nonadiabatic operations. Our goal is to use the eSTA method to provide fast population inversion even in the regime where the RWA does not hold (i.e. small values of t_f). This has been previously attempted using numerical methods [118]; however here it will be done analytically.

Our initial scheme $\vec{\lambda}_0$ was derived to be stable concerning systematic errors in the Rabi frequency [79] (e.g. arising from the Gaussian profile of the laser), and is given by

$$\begin{aligned} \Omega(\vec{\lambda}_0; t) &= \frac{\pi}{t_f} \sqrt{1 + 16 \sin^2 \left(\frac{\pi t}{t_f} \right)^6}, \\ \delta(\vec{\lambda}_0; t) &= -8 \frac{\pi}{t_f} \sin \left(\frac{\pi t}{t_f} \right) \sin \left(\frac{2\pi t}{t_f} \right) \frac{1 + 4 \sin^2(\pi t/t_f)^6}{1 + 16 \sin^2(\pi t/t_f)^6} \end{aligned} \quad (3.9)$$

By design, this scheme gives perfect population inversion for the idealised Hamiltonian \mathcal{H}_0 .

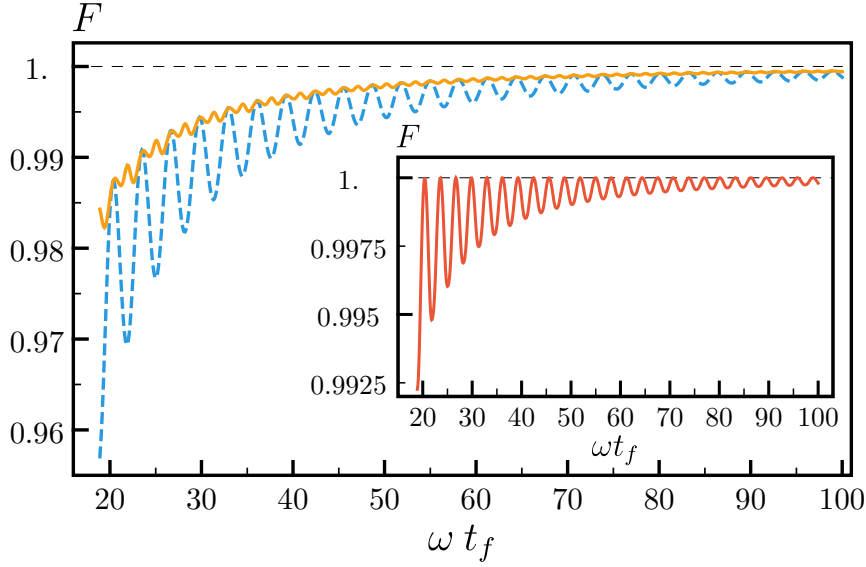


FIGURE 3.2: Population inversion without rotating-wave approximation: Fidelity F versus final time t_f for two-level Hamiltonian Eq. (3.9); STA scheme $\vec{\lambda}_0$ (blue, dashed line) and the eSTA scheme $\vec{\lambda}_s$ (orange, solid line). Inset: Fidelity F for the idealised Hamiltonian \mathcal{H}_0 using the eSTA scheme $\vec{\lambda}_s$ (red, solid line).

The scheme is modified as $\Omega(\vec{\lambda}; t) = \Omega(\vec{\lambda}_0; t) + f_1(\vec{\epsilon}; t)$ and $\delta(\vec{\lambda}; t) = \delta(\vec{\lambda}_0; t) + f_2(\vec{\epsilon}; t)$ where f_1 and f_2 are the minimal polynomial functions which fulfil $f_i(\vec{\epsilon}; t') = 0$ for $t' = 0, t_f$ and $f_i(\vec{\epsilon}; \frac{j t_f}{5}) = \epsilon_{4(i-1)+j}$, where we have chosen to use 8 components $\vec{\epsilon} = (\epsilon_n)_{n=1, \dots, 8}$. Note that $f_1(\vec{0}, t) = 0$ and $f_2(\vec{0}, t) = 0$. Since there are only two solutions in this setting, we can calculate $\vec{\epsilon}$ exactly, without any truncation. These solutions can be found analytically using Lewis-Riesenfeld Invariants [79].

The fidelity using the STA scheme and eSTA schemes for the system Hamiltonian \mathcal{H}_S , is shown in Fig. 3.2. For the shown final times t_f , the eSTA scheme outperforms the original STA scheme, since it always results in a higher or equal fidelity. The eSTA schemes are outside the set of STA control functions (see Fig. 3.1(d)). This can be seen by calculating the fidelity of the eSTA schemes for the the idealised Hamiltonian \mathcal{H}_0 (see inset of Fig.3.2). Since applying the STA scheme to the idealised Hamiltonian gives unit fidelity for all total times

t_f by construction, every fidelity value below one shows that the eSTA scheme is outside the set of STA schemes.

3.5 Single Particle Transport

We consider transport of a particle in a one dimensional trap over a distance d in a total time t_f . The trap trajectory $q_0(\vec{\lambda}, t)$ is parameterised by a real valued control vector $\vec{\lambda} = (\lambda_1, \dots, \lambda_6)$, so that $q_0(0) = 0$, $q_0(t_f) = d$ and $q_0(j/7) = \lambda_j$ for $j = 1, \dots, 6$. The system/idealised Hamiltonian is $\mathcal{H}_{S/0} = \frac{p^2}{2m} + V_{S/0}[x - q_0(\vec{\lambda}, t)]$ where $V_S(x) = U_0 \left[1 - \exp\left(-\frac{m\omega^2}{2U_0}x^2\right) \right]$ is a Gaussian potential, and $V_0(x) = \frac{1}{2}m\omega^2x^2$, since $V(x) \rightarrow V_0(x)$ for $\mu = 1/a \rightarrow 0$ where $a = U_0/(\hbar\omega)$. There are known STA techniques for \mathcal{H}_0 to design trajectories q_0 that give perfect fidelity e.g. using Lewis-Riesenfeld invariants [77]. A known dynamical invariant for harmonic trap transport has the form $I(t) = \frac{1}{2m}(p - m\dot{q}_c)^2 + \frac{1}{2}m\omega^2[x - mq_c(t)]^2$ where $q_c(t)$ must satisfy the auxiliary equation

$$\ddot{q}_c + \omega^2(q_c - q_0) = 0. \quad (3.10)$$

This equation relates the physical trap trajectory $q_0(t)$ with the particle's classical path $q_c(t)$ (which parameterises the state). $q_0(t)$ can be inverse engineered using boundary conditions and an appropriately chosen $q_c(t)$ via Eq. (3.10). To ensure the system is in the ground state after transport and that the trap is stationary, we require the boundary conditions $q_c(0) = 0$, $q_c(t_f) = d$, $\frac{d^n q_c(t')}{dt^n} = 0$ for $n = 1, \dots, 4$ at $t' = 0, t_f$. We set $q_c(t) = \sum_{n=0}^{10} c_n t^n$, and find $q_0(t)$ from Eq. (3.10). To implement eSTA we need only to calculate $\vec{\epsilon}$ using G_n and \vec{K}_n . The eigenstates $|\chi_n(s)\rangle$ are known analytically from [77], and so the integrals G_n and K_n can be calculated for each n . In the following, we will show that using $N = 1$ is sufficient.

In Fig. 3.3, the fidelity F is shown versus different final times t_f using the

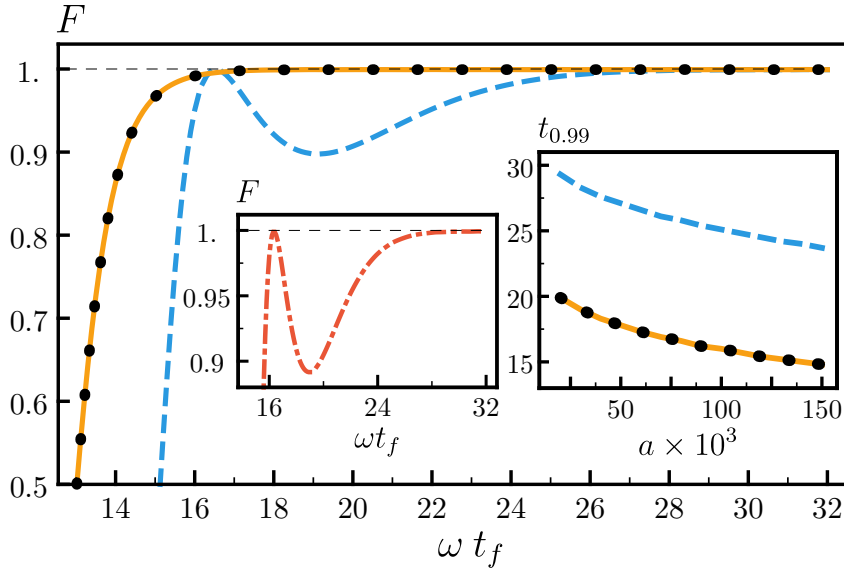


FIGURE 3.3: Transport of a single particle: Fidelity F versus total time t_f using the STA scheme $\vec{\lambda}_0$ (blue, dashed line) and the eSTA scheme $\vec{\lambda}_s$ ($N = 1$: orange, solid line, $N = 2$: black, dots); $a = 100 \times 10^3$. Left inset: Fidelity F for the idealised Hamiltonian \mathcal{H}_0 using the eSTA scheme $\vec{\lambda}_s$ (red, dashed-dotted line). Right inset: threshold time $t_{0.99}$ versus a . Transport distance $d = 1562\sigma$.

STA transport scheme $\vec{\lambda}_0$ (blue, dashed line) and eSTA transport scheme $\vec{\lambda}_s$ (using $N = 1$, orange, solid line). This was calculated numerically where the time evolution was performed using the Fourier split-operator method and the initial ground state was found by imaginary-time evolution. For generality, we use natural units; the frequency ω of the approximated harmonic potential as the inverse time unit, $\sigma = \sqrt{\hbar/(m\omega)}$ as the length scale and $\hbar\omega$ as the energy scale. We set the transport distance to $d = 1562\sigma$ and $a = 100 \times 10^3$. The chosen dimensionless values can correspond to different physical settings, for example to a ^{87}Rb atom within an optical Gaussian trap of $U_0 = 0.4 \text{ mK}$, a trap width of $w = 2\sqrt{a}\sigma = 334 \mu\text{m}$ (purposely chosen very wide to be far from the regime of classical and adiabatic motion) and a transport distance of $d = 825 \mu\text{m}$.

We see a significant improvement in transport fidelity using eSTA in comparison with STA. For extremely short times the approximation breaks down and neither STA nor eSTA produce good fidelity. For longer times the system

approaches adiabaticity and the two schemes converge. Clearly it is sufficient to consider just the first term, as the results for $N = 1$ and $N = 2$ are identical, see Fig. 3.3. While not a requirement, we note that the symmetry of the STA trajectory is preserved by the eSTA protocol.

To highlight these eSTA schemes are outside the set of STA schemes (Fig. 3.1(d)), we calculate the fidelity using $\vec{\lambda}_s$ for the idealised Hamiltonian \mathcal{H}_0 (left inset in Fig. 3.3, red dashed-dotted line). By design every STA scheme must give a fidelity of exactly one, which is not necessarily true when using the eSTA protocol.

To examine the dependence on a , we look at a threshold time $t_{0.99}$ which is defined as the time such that the fidelity $F \geq 0.99$ for all final times $t_f \geq t_{0.99}$. The right inset plot shows this threshold time $t_{0.99}$ versus different values of a . We see that the eSTA threshold time (orange, solid line) decreases with increasing a and is always much lower than the corresponding STA threshold time (blue, dashed line). We have also investigated other potentials which produced qualitatively similar results to the Gaussian trap. This underlines the broad applicability of eSTA for single particle transport.

3.6 Transport of two ions including Coulomb interaction

We now consider transport of two interacting (Coulomb) ions with equal mass m and charge $+e$, in a one dimensional Gaussian trap V_S (as in the previous case), over a distance d , and in total time t_f . The coordinates of the ions in the lab frame are given by x_1 and x_2 . We assume that $x_1 > x_2$ and treat the ions as distinguishable. We define $M = 2m$ and move to center-of-mass and relative coordinates defined by $x_c = (x_1 + x_2)/2$ and $x_r = (x_1 - x_2)/2$. The

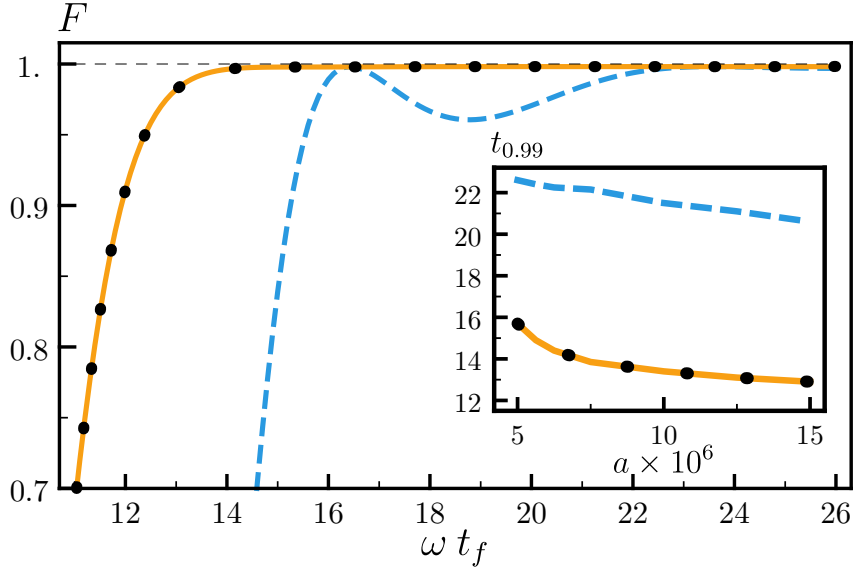


FIGURE 3.4: Transport of two ions including Coulomb interaction: $a = 10^7$ for the outer figure, $\tilde{C} = 7.35 \times 10^7$; otherwise see caption of Fig. 3.3.

system/idealised Hamiltonian then becomes

$$\mathcal{H}_{S/0} = \frac{p_c^2}{2M} + \frac{p_r^2}{2M} + \frac{C}{2x_r} + V_{S/0} [x_c + x_r - q_0(\vec{\lambda}, t)] + V_{S/0} [x_c - x_r - q_0(\vec{\lambda}, t)] \quad (3.11)$$

where $C = e^2/4\pi\epsilon_0$, and $V_0(x) = \frac{1}{2}M\omega^2x^2$ in this case. As \mathcal{H}_0 becomes separable in center-of-mass and relative coordinates, STA techniques need only be applied to the center-of-mass [124]. For the eSTA scheme, we assume that the relative distance between the ions is constant and equal to the stationary equilibrium distance when calculating G_n and \vec{K}_n .

In Fig. 3.4, the fidelity F is shown versus different final times t_f using the STA transport scheme $\vec{\lambda}_0$ (dashed, blue line) and the eSTA transport scheme $\vec{\lambda}_s$ (using $N = 1$, orange, solid line). We set the transport distance to $d = 1562\sigma$, $a = 10^7$ and the dimensionless Coulomb constant $\tilde{C} = \frac{e^2}{4\pi\epsilon_0} \frac{1}{\sigma\hbar\omega} = 7.35 \times 10^7$. These dimensionless values can correspond to different physical settings, for example transport of two ${}^9\text{Be}^+$ ions over $370 \mu\text{m}$ in a surface ion trap of depth $U_0 = 0.8 \text{ meV}$, and frequency 0.13 MHz (again a large trap width).

Similar to the previous case, we see a significant improvement in transport fidelity based on eSTA in comparison with STA. For longer times the system approaches adiabaticity and the two schemes converge. It is sufficient to consider just the first order (i.e. set $N = 1$ when calculating the eSTA scheme); to check this we also plot the result for $N = 2$ (black dots) which give identical results. As before, one finds that the eSTA schemes are outside the set of STA schemes. The inset of Fig. 3.4 shows the threshold time $t_{0.99}$ versus a . We see that the eSTA threshold times (using $N = 1$, orange, solid line) decreases with increasing a and it is always significantly lower than the corresponding STA threshold time (blue dashed line).

3.7 Conclusion

In this chapter we have presented an analytic extension to previous STA quantum control methods. We have demonstrated through three complementary examples relevant to quantum technologies, that this method can be applied to improve performance and achieve physical insight. Further work could focus on deriving strict criteria and uncertainty relations for when the method works effectively. The eSTA procedure could be extended in several ways such as to condensates, open systems, and even beyond the scope of quantum control.

3.8 Appendix

In the following we provide further details concerning the estimations of $F(\mu, \vec{\lambda}_0)$ and $\nabla F(\mu, \vec{\lambda}_0)$, which are used to derive the main eSTA formula. We highlight again that throughout the derivations, $\nabla = \nabla_{\vec{\lambda}}$ i.e. the gradient with respect to $\vec{\lambda}$. A series expansion of the time-evolution operator of the system Hamiltonian is

$$U_{\mu, \vec{\lambda}}(t_2, t_1) = \sum_{n=0}^{\infty} \mu^n U_{\vec{\lambda}}^{(n)}(t_2, t_1), \quad (3.12)$$

where the first order is

$$U_{\vec{\lambda}}^{(1)}(t_2, t_1) = -\frac{i}{\hbar} \int_{t_1}^{t_2} dt U_{\vec{\lambda}}^{(0)}(t_2, t) \mathcal{H}^{(1)}(\vec{\lambda}; t) U_{\vec{\lambda}}^{(0)}(t, t_1), \quad (3.13)$$

the second order is

$$\begin{aligned} U_{\vec{\lambda}}^{(2)}(t_2, t_1) = & -\frac{1}{\hbar^2} \int_{t_1}^{t_2} dt \int_{t_1}^t ds U_{\vec{\lambda}}^{(0)}(t_2, t) \mathcal{H}^{(1)}(\vec{\lambda}; t) U_{\vec{\lambda}}^{(0)}(t, s) \mathcal{H}^{(1)}(\vec{\lambda}; s) U_{\vec{\lambda}}^{(0)}(s, t_1) \\ & - \frac{i}{\hbar} \int_{t_1}^{t_2} dt U_{\vec{\lambda}}^{(0)}(t_2, t) \mathcal{H}^{(2)}(\vec{\lambda}; t) U_{\vec{\lambda}}^{(0)}(t, t_1), \end{aligned} \quad (3.14)$$

and finally the third order is

$$\begin{aligned} U_{\vec{\lambda}}^{(3)}(t_2, t_1) = & \frac{i}{\hbar^3} \int_{t_1}^{t_2} dt \int_{t_1}^t ds \int_{t_1}^s du \left[\right. \\ & U_{\vec{\lambda}}^{(0)}(t_2, t) \mathcal{H}^{(1)}(\vec{\lambda}; t) U_{\vec{\lambda}}^{(0)}(t, s) \mathcal{H}^{(1)}(\vec{\lambda}; s) U_{\vec{\lambda}}^{(0)}(s, u) \mathcal{H}^{(1)}(\vec{\lambda}; u) U_{\vec{\lambda}}^{(0)}(u, t_1) \left. \right] \\ & - \frac{1}{\hbar^2} \int_{t_1}^{t_2} dt \int_{t_1}^t ds U_{\vec{\lambda}}^{(0)}(t_2, t) \left[\mathcal{H}^{(1)}(\vec{\lambda}; t) U_{\vec{\lambda}}^{(0)}(t, s) \mathcal{H}^{(2)}(\vec{\lambda}; s) \right. \\ & \quad \left. + \mathcal{H}^{(2)}(\vec{\lambda}; t) U_{\vec{\lambda}}^{(0)}(t, s) \mathcal{H}^{(1)}(\vec{\lambda}; s) \right] U_{\vec{\lambda}}^{(0)}(s, t_1) \\ & - \frac{i}{\hbar} \int_{t_1}^{t_2} dt U_{\vec{\lambda}}^{(0)}(t_2, t) \mathcal{H}^{(3)}(\vec{\lambda}; t) U_{\vec{\lambda}}^{(0)}(t, t_1). \end{aligned} \quad (3.15)$$

We define the following useful matrix elements

$$\alpha_{n,m}^{(j)}(t) = \langle \chi_n(t) | \mathcal{H}^{(j)}(\vec{\lambda}_0; t) | \chi_m(t) \rangle, \quad (3.16)$$

$$\vec{\beta}_{n,m}^{(j)}(t) = \langle \chi_n(t) | \nabla \mathcal{H}^{(j)}(\vec{\lambda}_0; t) | \chi_m(t) \rangle. \quad (3.17)$$

Note also that the matrix elements defined in Eq. (3.16) and Eq. (3.17) obey the relations $\alpha_{n,m}^{(j)}(t) = \alpha_{m,n}^{(j)}(t)^*$ and $\vec{\beta}_{n,m}^{(j)}(t) = \vec{\beta}_{m,n}^{(j)}(t)^*$. Hence it follows that $\alpha_{n,n}^{(j)}(t)$ and $\vec{\beta}_{n,n}^{(j)}(t)$ are real.

3.8.1 Approximation of $F(\mu, \vec{\lambda}_0)$

From a series expansion of the fidelity in μ we get

$$F(\mu, \vec{\lambda}_0) = \sum_{n=0}^{\infty} \mu^n F^{(n)}. \quad (3.18)$$

By defining

$$u_j = \langle \chi_0(t_f) | U_{\vec{\lambda}_0}^{(j)}(t_f, 0) | \chi_0(0) \rangle, \quad (3.19)$$

we can express the coefficients in Eq. (3.18) generally as

$$F^{(n)} = \sum_{k=0}^n u_{n-k} u_k^* = \begin{cases} |u_{n/2}|^2 + 2 \operatorname{Re} \left(\sum_{k=0}^{\frac{n}{2}-1} u_{n-k} u_k^* \right), & n \text{ is even} \\ 2 \operatorname{Re} \left(\sum_{k=0}^{(n-1)/2} u_{n-k} u_k^* \right), & n \text{ is odd} \end{cases}$$

Since the STA scheme works perfectly for the idealised Hamiltonian by construction, we have that $u_0 = 1$ and hence $F^{(0)} = 1$. From Eq. (3.13), we get

$$u_1 = -\frac{i}{\hbar} \int_0^{t_f} dt \langle \chi_0(t) | \mathcal{H}^{(1)}(\vec{\lambda}_0; t) | \chi_0(t) \rangle = -\frac{i}{\hbar} \int_0^{t_f} dt \alpha_{0,0}^{(1)}(t). \quad (3.20)$$

As u_1 is purely imaginary, it follows that $F^{(1)} = 0$.

Now by using Eq. (3.14), we get

$$u_2 = -\frac{1}{\hbar^2} \int_0^{t_f} dt \int_0^t ds \langle \chi_0(t) | \mathcal{H}^{(1)}(\vec{\lambda}; t) U_{\vec{\lambda}_0}^{(0)}(t, s) \mathcal{H}^{(1)}(\vec{\lambda}; s) | \chi_0(s) \rangle \\ - \frac{i}{\hbar} \int_0^{t_f} dt \langle \chi_n(t) | \mathcal{H}^{(2)}(\vec{\lambda}_0; t) | \chi_0(t) \rangle. \quad (3.21)$$

Using $U_{\vec{\lambda}_0}^{(0)}(t, s) = \sum_n |\chi_n(t)\rangle \langle \chi_n(s)|$ simplifies this to

$$u_2 = -\frac{1}{\hbar^2} \int_0^{t_f} dt \int_0^t ds \sum_n \alpha_{0,n}^{(1)}(t) \alpha_{n,0}^{(1)}(s) - \frac{i}{\hbar} \int_0^{t_f} dt \alpha_{0,0}^{(2)}(t).$$

After a suitable transformation of the integration variables, we can also write this as

$$u_2 = -\frac{1}{2\hbar^2} \int_0^{t_f} dt \sum_n \left[\int_0^t ds \alpha_{0,n}^{(1)}(t) \alpha_{n,0}^{(1)}(s) + \int_t^{t_f} ds \alpha_{0,n}^{(1)}(s) \alpha_{n,0}^{(1)}(t) \right] \\ - \frac{i}{\hbar} \int_0^{t_f} dt \alpha_{0,0}^{(2)}(t). \quad (3.22)$$

This form will be useful for calculating $F^{(2)}$ since

$$2 \operatorname{Re}(u_2) = -\frac{1}{\hbar^2} \sum_n \int_0^{t_f} dt \int_0^t ds \operatorname{Re} \left[\alpha_{0,n}^{(1)}(t) \alpha_{n,0}^{(1)}(s) \right] \\ = -\frac{1}{\hbar^2} \sum_n \operatorname{Re} \left[\int_0^{t_f} dt \alpha_{0,n}^{(1)}(t) \int_0^{t_f} ds \alpha_{n,0}^{(1)}(s) \right] \\ = -\frac{1}{\hbar^2} \sum_n \left| \int_0^{t_f} dt \alpha_{n,0}^{(1)}(t) \right|^2 \quad (3.23)$$

because $\alpha_{0,n}^{(1)} = \alpha_{n,0}^{(1)*}$ and $\alpha_{0,0}^{(2)}(t)$ is real. Finally, we get

$$F^{(2)} = -\frac{1}{\hbar^2} \sum_{n=1}^{\infty} \left| \int_0^{t_f} dt \alpha_{n,0}^{(1)}(t) \right|^2. \quad (3.24)$$

In a similar way by using Eq. (3.15), we arrive at

$$\begin{aligned}
u_3 &= \frac{i}{\hbar^3} \int_{t_1}^{t_f} dt \int_0^t ds \int_0^s du \sum_{n,m} \alpha_{0,n}^{(1)}(t) \alpha_{n,m}^{(1)}(s) \alpha_{n,0}^{(1)}(u) \\
&\quad - \frac{1}{\hbar^2} \int_0^{t_f} dt \int_0^t ds \sum_n \left[\alpha_{0,n}^{(1)}(t) \alpha_{n,0}^{(2)}(s) + \alpha_{0,n}^{(2)}(t) \alpha_{n,0}^{(1)}(s) \right] \\
&\quad - \frac{i}{\hbar} \int_0^{t_f} dt \alpha_{0,0}^{(3)}. \tag{3.25}
\end{aligned}$$

We use this together with previous results to calculate $F^{(3)}$. However, we restrict to the contributions which involve double integrals (while ignoring the contributions with three integrals over time). In such a way,

$$F^{(3)} \approx -\frac{2}{\hbar^2} \sum_{n=1}^{\infty} \text{Re} \left[\left(\int_0^{t_f} dt \alpha_{n,0}^{(1)}(t) \right)^* \left(\int_0^{t_f} dt \alpha_{n,0}^{(2)}(t) \right) \right].$$

3.8.2 Approximation of $\nabla F(\mu, \vec{\lambda}_0)$

The gradient of the fidelity

$$\nabla F(\mu, \vec{\lambda}_0) = 2 \text{Re} \left[\langle \chi_0(t_f) | \nabla U_{\mu, \vec{\lambda}_0}(t_f, 0) | \chi_0(0) \rangle \langle \chi_0(t_f) | U_{\mu, \vec{\lambda}_0}(t_f, 0) | \chi_0(0) \rangle^* \right], \tag{3.26}$$

can be expand in μ

$$\nabla F(\mu, \lambda_0) = \sum_{n=0}^{\infty} \mu^n \vec{\mathcal{F}}^{(n)}. \tag{3.27}$$

If we define

$$\vec{v}_j = \langle \chi_0(t_f) | \nabla U_{\vec{\lambda}_0}^{(j)}(t_f, 0) | \chi_0(0) \rangle, \tag{3.28}$$

then we can express the coefficients in Eq. (3.27) as

$$\vec{\mathcal{F}}^{(n)} = 2 \operatorname{Re} \left(\sum_{k=0}^n \vec{v}_{n-k} u_k^* \right). \quad (3.29)$$

It will be useful to define a generalisation of \vec{v}_0 namely

$$\vec{W}_{n,m}(t_2, t_1) \equiv \langle \chi_n(t_2) | \nabla U_{\vec{\lambda}_0}^{(0)}(t_2, t_1) | \chi_m(t_1) \rangle. \quad (3.30)$$

Using time-dependent perturbation theory (similar to the previous subsection) and $\mathcal{H}^{(0)}(\vec{\lambda}) \approx \mathcal{H}^{(0)}(\vec{\lambda}_0) + (\vec{\lambda} - \vec{\lambda}_0) \cdot \nabla \mathcal{H}^{(0)}(\vec{\lambda}_0)$, simplifies this to

$$\vec{W}_{n,m}(t_2, t_1) = -\frac{i}{\hbar} \int_{t_1}^{t_2} dt \vec{\beta}_{n,m}^{(0)}(t). \quad (3.31)$$

Especially $\vec{v}_0 = \vec{W}_{0,0}(t_f, 0)$. Since $\vec{W}_{0,0}$ is purely imaginary, it follows that $\vec{\mathcal{F}}^{(0)} = \vec{0}$.

From Eq. (3.13), we get

$$\vec{v}_1 = -\frac{i}{\hbar} \int_0^{t_f} dt \langle \chi_0(t_f) | \nabla \left[U_{\vec{\lambda}}^{(0)}(t_f, t) \mathcal{H}^{(1)}(\vec{\lambda}; t) U_{\vec{\lambda}}^{(0)}(t, 0) \right] \Big|_{\vec{\lambda}=\vec{\lambda}_0} | \chi_0(0) \rangle. \quad (3.32)$$

Using the product rule and inserting identities $= \sum_n |\chi_n(t)\rangle \langle \chi_n(t)|$ we arrive at

$$\begin{aligned} \vec{v}_1 &= -\frac{i}{\hbar} \int_0^{t_f} dt \left\{ \sum_n \left[\vec{W}_{0,n}(t_f, t) \alpha_{n,0}^{(1)}(t) + \alpha_{0,n}^{(1)}(t) \vec{W}_{n,0}(t, 0) \right] + \vec{\beta}_{0,0}^{(1)}(t) \right\} \\ &= -\frac{1}{\hbar^2} \sum_n \int_0^{t_f} dt \left[\int_t^{t_f} ds \vec{\beta}_{0,n}^{(0)}(s) \alpha_{n,0}^{(1)}(t) + \int_0^t ds \alpha_{0,n}^{(1)}(t) \vec{\beta}_{n,0}^{(0)}(s) \right] \\ &\quad - \frac{i}{\hbar} \int_0^{t_f} dt \vec{\beta}_{0,0}^{(1)}(t). \end{aligned} \quad (3.33)$$

In order to find $\vec{\mathcal{F}}^{(1)}$, we first calculate

$$2 \operatorname{Re}(\vec{v}_1) = -\frac{2}{\hbar^2} \sum_n \operatorname{Re} \left[\int_0^{t_f} dt \alpha_{n,0}^{(1)}(t) \int_0^{t_f} ds \vec{\beta}_{n,0}^{(0)}(s)^* \right], \quad (3.34)$$

and

$$2 \operatorname{Re}(\vec{v}_0 u_1^*) = \frac{2}{\hbar^2} \operatorname{Re} \left[\int_0^{t_f} dt \alpha_{0,0}^{(1)}(t) \int_0^{t_f} ds \vec{\beta}_{0,0}^{(0)}(s)^* \right]. \quad (3.35)$$

By combining these two results gives

$$\vec{\mathcal{F}}^{(1)} = -\frac{2}{\hbar^2} \sum_{n=1}^{\infty} \operatorname{Re} \left[\int_0^{t_f} dt \alpha_{n,0}^{(1)}(t) \int_0^{t_f} ds \vec{\beta}_{n,0}^{(0)}(s)^* \right]. \quad (3.36)$$

Using Eq. (3.14) and a similar calculation as above, we arrive at

$$\begin{aligned} \vec{v}_2 = & \frac{i}{\hbar^3} \int_0^{t_f} dt \int_0^t ds \sum_{n,m} \left[\int_t^{t_f} du \vec{\beta}_{0,n}^{(0)}(u) \alpha_{n,m}^{(1)}(t) \alpha_{m,0}^{(1)}(s) \right. \\ & \left. + \int_s^t du \alpha_{0,n}^{(1)}(t) \vec{\beta}_{n,m}^{(0)}(u) \alpha_{m,0}^{(1)}(s) + \int_0^s du \alpha_{0,n}^{(1)}(t) \alpha_{n,m}^{(1)}(s) \vec{\beta}_{m,0}^{(0)}(u) \right] \\ & - \frac{1}{\hbar^2} \int_0^{t_f} dt \int_0^t ds \left\{ \sum_n \left[\vec{\beta}_{0,n}^{(1)}(t) \alpha_{n,0}^{(1)}(s) + \alpha_{0,n}^{(1)}(t) \vec{\beta}_{n,0}^{(1)}(s) \right] \right\} \\ & - \frac{1}{\hbar^2} \sum_n \int_0^{t_f} dt \left[\int_t^{t_f} ds \vec{\beta}_{0,n}^{(0)}(s) \alpha_{n,0}^{(2)}(t) + \int_0^t ds \alpha_{0,n}^{(2)}(t) \vec{\beta}_{n,0}^{(0)}(s) \right] \\ & - \frac{i}{\hbar} \int_0^{t_f} dt \vec{\beta}_{0,0}^{(2)}(t). \end{aligned} \quad (3.37)$$

Similarly to the calculation of $\vec{\mathcal{F}}^{(2)}$, we neglect contributions involving three integrals over time which results in

$$\begin{aligned} \vec{\mathcal{F}}^{(2)} \approx & -\frac{2}{\hbar^2} \sum_{n=1}^{\infty} \operatorname{Re} \left[\left(\int_0^{t_f} dt \vec{\beta}_{n,0}^{(1)}(t) \right)^* \left(\int_0^{t_f} dt \alpha_{n,0}^{(1)}(t) \right) \right. \\ & \left. + \left(\int_0^{t_f} dt \vec{\beta}_{n,0}^{(0)}(t) \right)^* \left(\int_0^{t_f} dt \alpha_{n,0}^{(2)}(t) \right) \right]. \end{aligned} \quad (3.38)$$

Chapter 4

Robustness of enhanced shortcuts to adiabaticity in lattice transport

4.1 Overview

In this Chapter we consider the robustness of eSTA to different types of noise. It is conjectured that eSTA can offer simultaneously improvement in fidelity and robustness against noise. We first provide a heuristic argument as to why this should be true, and then provide numerical evidence of this claim by applying eSTA to fast atomic transport using an optical lattice and evaluating several appropriate robustness measures. We consider several starting STA schemes from which we construct improved eSTA schemes. We show that the eSTA schemes not only produce higher fidelities than the original STA schemes, but also remain more stable against several common errors and environmental noise.

This chapter is based on the following publication:

C. Whitty, A. Kiely and A. Ruschhaupt,

Robustness of enhanced shortcuts to adiabaticity in lattice transport,

Phys. Rev. A 105, 013311 (2022).

4.2 Introduction

Quantum devices and technologies have the potential to revolutionise a broad range of scientific and engineering disciplines [89, 128]. However, fast and stable control of these systems is a significant barrier to building practical devices [93]. Quantum control needs to be fast to avoid decoherence, while simultaneously being robust and stable against implementation errors. Furthermore, it should be effective within the constrained resources of the physical implementation, such as energetic cost or pulse bandwidth [122].

Often practical quantum control relies heavily on numerical optimisation, which has some drawbacks: it can be computationally expensive, difficult to scale and it may be unclear how to understand or generalise the resulting schemes [129–131]. There exists alternative analytic techniques, such as Shortcuts to Adiabaticity (STA), which give exact quantum state transfer. However, analytic techniques such as STA are known exactly for only a limited number of physical systems [10, 11, 72]. In Chapter 3 we developed an extension to STA methods, known as enhanced Shortcuts to Adiabaticity (eSTA), that provides control of a broader class of systems [132]. Crucially, eSTA is an analytic technique that allows physical insight into the control scheme. Additionally, eSTA has a much lower computation cost compared with full numerical optimisation. eSTA has been applied to population inversion in a two-level system without the rotating-wave approximation and to the transport of a Gaussian trap with one and two ions [132]. There has already been a first application of eSTA techniques to the transport of atoms in an optical lattice [12].

STA schemes are extremely robust to noise and systematic errors [35, 40, 79, 101, 133]. An obvious question is whether robustness remains in the eSTA framework. Therefore, the main goal of this chapter is to provide a thorough investigation into how this stability is affected by the application of eSTA.

We choose atomic transport using an optical lattice to examine the robustness of eSTA, since the coherent control of lattice systems has many practical quantum technological applications. For example: transport in atomic chains [134], modeling condensed matter systems [135], many-body phenomena in ultracold gases [136] and the trapping and control of ions [137, 138]. There has been experimental exploration of atom transport via a lattice potential around the quantum speed limit [76]. We consider similar physical parameters with transport times near this proposed speed limit [76]. We then show that the eSTA schemes provide improved robustness over the corresponding STA schemes, when considering a variety of imperfections.

In the following section we give a brief review of the formalism of eSTA. In Section 4.4 we present the physical optical lattice model we are considering; we will introduce different control schemes and we examine and compare the fidelities achieved by eSTA. In Section 4.5, we first define and then examine the deviation of the eSTA control function under variations of the Hamiltonian. This gives a preliminary indication of the stability of eSTA. In the following sections we compare the stability of eSTA and STA in more detail. This includes a definition of a sensitivity quantity and an error bound for a quantitative comparison of the stability of different schemes. In Section 4.6 we consider systematic errors during the transport. In Section 4.7 the stability of lattice transport is examined for noisy fluctuations.

4.3 eSTA Formalism

The purpose of eSTA is to provide a formalism by which existing STA methods can be extended to quantum control problems beyond their current scope.

We start with a system with Hamiltonian \mathcal{H}_s that has a difficult quantum control problem. However, we assume that the Hamiltonian \mathcal{H}_s can be approximated by another Hamiltonian \mathcal{H}_0 of an idealised system that has an exact

STA solution. In the following we construct the improved eSTA protocol for \mathcal{H}_s using the solutions of the idealised system \mathcal{H}_0 .

4.3.1 Construction of eSTA control scheme

To make the approximation of \mathcal{H}_s by \mathcal{H}_0 precise, we assume there is a parameter μ and Hamiltonians \mathcal{H}_μ such that $\mathcal{H}_{\mu=\mu_s} = \mathcal{H}_s$ and $\mathcal{H}_{\mu=0} = \mathcal{H}_0$. We also assume we can parameterise the control scheme by a vector $\vec{\lambda}$. We set $\vec{\lambda}_0$ to denote the STA scheme, and $\vec{\lambda}_s$ as the eSTA scheme.

Our goal is to evolve the initial state $|\Psi_0\rangle$ at time $t = 0$ to the target state $|\Psi_T\rangle$ in a given total time t_f . As previously discussed, we assume there exists an idealised system with known STA solutions and Hamiltonian $\mathcal{H}_0(\vec{\lambda}_0; t)$. $\vec{\lambda}_0$ solves the control problem for \mathcal{H}_0 , and we assume it works approximately for \mathcal{H}_{μ_s} . To state this formally we define the fidelity

$$F(\mu, \vec{\lambda}) = \left| \langle \Psi_T | U_{\mu, \vec{\lambda}}(t_f, 0) | \Psi_0 \rangle \right|^2, \quad (4.1)$$

where $U_{\mu, \vec{\lambda}}$ is the time evolution operator using the Hamiltonian \mathcal{H}_μ with control scheme $\vec{\lambda}$. We have that $F(\mu_s, \vec{\lambda}_0) < F(0, \vec{\lambda}_0) = 1$; see also Fig. 4.1 (a).

The goal of eSTA is to produce a $\vec{\lambda}_s$ that is built upon $\vec{\lambda}_0$, such that we maximise $F(\mu_s, \vec{\lambda}_s)$ with $F(\mu_s, \vec{\lambda}_s) > F(\mu_s, \vec{\lambda}_0)$. We define $\vec{\lambda}_s = \vec{\lambda}_0 + \vec{\epsilon}$, and eSTA is now used to calculate $\vec{\epsilon}$.

To find $\vec{\epsilon}$, we use information about the fidelity and the gradient of the fidelity with respect to $\vec{\lambda}$ to construct a parabola in the parameter space of $\vec{\lambda}$ and F , as illustrated in Fig. 4.1 (b). We assume that this parabola is a good approximation to the fidelity landscape in the direction of the gradient at $(\mu_s, \vec{\lambda}_0)$. This is schematically shown in Fig. 4.1 (b), with the dashed red line representing the parabolic approximation and the solid-blue line denoting the actual fidelity landscape. Furthermore we assume that the maximum of this

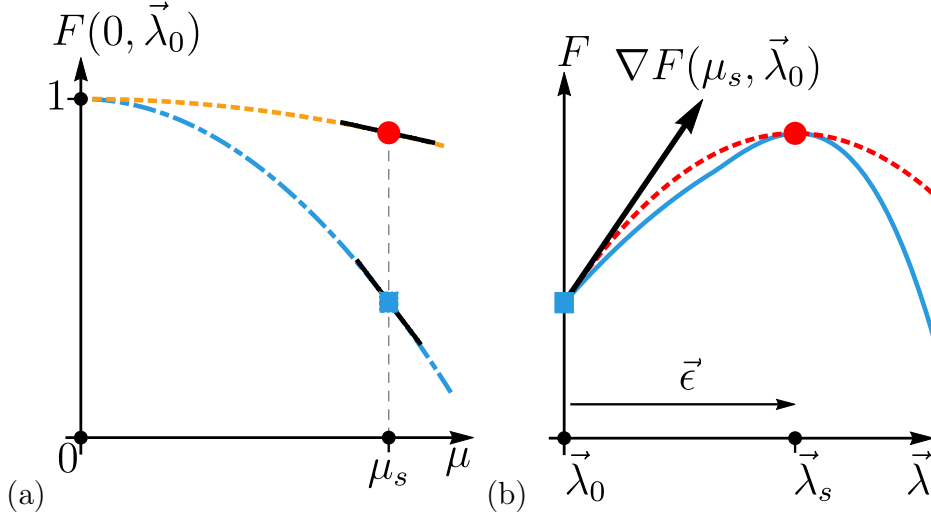


FIGURE 4.1: (a) is a schematic representation of fidelity versus μ . The fidelity of \mathcal{H}_μ using $\vec{\lambda}_0$ is the dash-dotted blue line. The blue square is \mathcal{H}_{μ_s} using $\vec{\lambda}_0$. The red dot is the improved fidelity of \mathcal{H}_{μ_s} using $\vec{\lambda}_s$. The dashed-orange line represents the assumed parabolic profile of the fidelity as $\mathcal{H}_0 \rightarrow \mathcal{H}_{\mu_s}$, with the improved eSTA control $\vec{\lambda}_\mu$ calculated for each μ . The slopes of each line at μ_s are depicted as solid-black lines. (b) is a diagram of eSTA in control space $(\vec{\lambda}, F)$. The starting STA scheme fidelity (blue square), gradient (black arrow) and fidelity at $\vec{\lambda}_s$ (red dot) are shown. The resulting eSTA approximate parabola (dashed-red line), and true fidelity landscape (solid-blue line) are also displayed.

parabola gives perfect fidelity, i.e. $F(\mu_s, \vec{\lambda}_0 + \vec{\epsilon}) \approx 1$. We can then write

$$\vec{\epsilon} \approx \frac{2 \left[1 - F(\mu_s, \vec{\lambda}_0) \right]}{\left| \nabla F(\mu_s, \vec{\lambda}_0) \right|} \frac{\nabla F(\mu_s, \vec{\lambda}_0)}{\left| \nabla F(\mu_s, \vec{\lambda}_0) \right|}, \quad (4.2)$$

where $\nabla = \nabla_{\vec{\lambda}}$, the gradient with respect to $\vec{\lambda}$.

We now calculate $\vec{\epsilon}$ using an approximation of the gradient and fidelity at the point $(\mu_s, \vec{\lambda}_0)$, shown as the blue square in Fig. 4.1. We begin the derivation of these estimates by assuming that the initial state $|\Psi_0\rangle$ and the final target state $|\Psi_T\rangle$ are both the same for the \mathcal{H}_0 and \mathcal{H}_{μ_s} systems. We assume that the idealised \mathcal{H}_0 system can be treated with STA techniques, i.e. there is a solution $|\chi_0(t)\rangle$ of the time evolution leading to fidelity one, i.e. $|\chi_0(0)\rangle = |\Psi_0\rangle$ and $|\chi_0(t_f)\rangle = |\Psi_T\rangle$. In addition, we assume that there are solutions of

the time evolution of \mathcal{H}_0 labeled $\{|\chi_n(t)\rangle\}_{n \in \mathbb{N}}$ such that $\{|\chi_n(t)\rangle\}_{n \in \mathbb{N}_0}$ form an orthonormal basis for solutions of the \mathcal{H}_{μ_s} system. So we have

$$|\chi_n(t)\rangle = U_{0, \vec{\lambda}_0}(t, 0)|\chi_n(0)\rangle, \quad (4.3)$$

$$U_{0, \vec{\lambda}_0}(t, s) = \sum_n |\chi_n(t)\rangle \langle \chi_n(s)|. \quad (4.4)$$

Note that in the following examples, we will use invariant-based inverse engineering to design the STA solutions and in these cases $\{|\chi_n(t)\rangle\}_{n \in \mathbb{N}_0}$ are (up to a phase) the instantaneous eigenstates of the corresponding invariant.

We use time dependent perturbation theory to calculate an approximation of the fidelity $F(\mu_s, \vec{\lambda}_0)$ and the gradient of the fidelity $\nabla F(\mu_s, \vec{\lambda}_0)$. We assume that we can neglect higher order contributions in both μ and $\vec{\epsilon}$. The details of the calculations can be found in [132]. For the fidelity $F(\mu_s, \vec{\lambda}_0)$ we then obtain up to second order in μ_s

$$F(\mu_s, \vec{\lambda}_0) \approx 1 - \frac{1}{\hbar^2} \sum_{n=1}^{\infty} |G_n|^2, \quad (4.5)$$

where

$$G_n = \int_0^{t_f} dt \langle \chi_n(t) | \left[\mathcal{H}_{\mu_s}(\vec{\lambda}_0; t) - H_0(\vec{\lambda}_0; t) \right] | \chi_0(t) \rangle. \quad (4.6)$$

For the gradient approximation we find

$$\nabla F(\mu_s, \lambda_0) \approx -\frac{2}{\hbar^2} \sum_{n=1}^{\infty} \text{Re} \left(G_n \vec{K}_n^* \right), \quad (4.7)$$

with

$$\vec{K}_n = \int_0^{t_f} dt \langle \chi_n(t) | \nabla \mathcal{H}_{\mu_s}(\vec{\lambda}_0; t) | \chi_0(t) \rangle. \quad (4.8)$$

Using Eq. (4.2), we can now write the analytical expression for the eSTA protocol $\vec{\lambda}_s \approx \vec{\lambda}_0 + \vec{\epsilon}$

$$\vec{\epsilon} = - \frac{\left(\sum_{n=1}^N |G_n|^2 \right) \left[\sum_{n=1}^N \operatorname{Re} \left(G_n^* \vec{K}_n \right) \right]}{\left| \sum_{n=1}^N \operatorname{Re} \left(G_n^* \vec{K}_n \right) \right|^2}, \quad (4.9)$$

where G_n is given by Eq. (4.6), K_n is given by Eq. (4.8), and we have truncated the infinite sums to the first N terms.

It is important to note that G_n and \vec{K}_n can both be easily calculated as only the Hamiltonians and the known STA solutions for the idealised system with Hamiltonian \mathcal{H}_0 are needed. We also note that eSTA can produce protocols which are outside the class of STA schemes and offers improvement over previous perturbation based optimisation [132].

4.3.2 Expected stabilities of eSTA and STA

We now provide a general heuristic argument of why it is expected that eSTA protocols not only have improved fidelity, but also have improved stability compared with their corresponding STA schemes. Let us consider Fig. 4.1 (a), showing schematically the fidelity versus μ ; $\mu = 0$ corresponds with the approximated system and μ_s the system of interest. The fidelity of \mathcal{H}_μ using the initial STA control scheme $\vec{\lambda}_0$ is the dot-dashed blue line; the dashed-orange line represents the fidelity using the improved eSTA control $\vec{\lambda}_\mu$ calculated for each μ . Since the STA and eSTA control schemes agree at $\mu = 0$, the fidelity must be one for both at this point. By construction, for a given μ the fidelity produced using the eSTA control scheme (dashed orange line) is higher than the corresponding one for the STA scheme (dot-dashed blue line). Assuming that the fidelity behaves as a parabola, the magnitude of the slope of the eSTA fidelity must be less than the slope of the STA fidelity at μ_s .

We now consider the effect of a systematic error δ , such that the STA and

eSTA schemes derived using μ_s are now applied to the system at a different, near-by $\mu = \mu_s(1 + \delta)$. We expect that the derivative of the fidelity in both cases can be approximated by the slopes shown in Fig. 4.1 (a) (solid-black lines). Therefore, the fidelity in the eSTA case should vary less than the fidelity in the STA case. Thus, the eSTA protocol should have higher stability against changes in μ than the corresponding STA scheme. To confirm this intuitive reasoning, in the following we will examine the stability in more detail.

4.4 Physical Model

We consider atomic transport in an optical lattice, which currently has no STA solution. For sufficient trapping depths the lattice potential can be well approximated locally by the harmonic potential. The transport of a harmonic potential has an exact STA solution for all transport times using Lewis-Riesenfeld invariants [10, 11]. Hence, we choose the harmonic potential transport STA solutions as the starting point to produce an eSTA protocol for the lattice transport problem.

The lattice potential is given by

$$V_S(x) = U_0 \sin^2(k_0 x), \quad (4.10)$$

where $U_0 = \alpha E_{\text{rec}}$, $E_{\text{rec}} = 2(\pi\hbar)^2/m\lambda^2$ and $k_0 = 2\pi/\lambda$. We choose $\alpha = 150$ in agreement with a physically implemented value in [76]. The motion of the lattice is described by a function $q_0(t)$, and Hamiltonian $\mathcal{H}_{\mu_s} = H_S$ where

$$H_S = \frac{p^2}{2m} + V_S \left[x - q_0(\vec{\lambda}, t) \right]. \quad (4.11)$$

For designing the STA trajectories, we apply a harmonic approximation to the potential V_S . A series expansion of $V_S(x)$ results in

$$V_S(x) = V_0(x) + \mathcal{O}(x^4), \quad (4.12)$$

where

$$V_0(x) = \frac{1}{2}m\omega_0^2x^2, \quad (4.13)$$

and $\omega_0 = \sqrt{\frac{2U_0}{m}}k_0 = \sqrt{\alpha}(4\pi^2\hbar)/m\lambda^2$. The corresponding idealised Hamiltonian $\mathcal{H}_0 = H_0$ is

$$H_0 = \frac{p^2}{2m} + V_0[x - q_0(\vec{\lambda}, t)]. \quad (4.14)$$

Note that in this case as $U_0 \rightarrow \infty$, $H_S \rightarrow H_0$.

We also define a time unit $\tau = 2\pi/\omega_0$ and a spatial unit $\sigma = \sqrt{\hbar/(m\omega_0)}$.

4.4.1 STA control functions

There exists known STA techniques to design trajectories $q_0(t)$ that give fidelity $F = 1$ for the harmonic potential H_0 and arbitrary transport times [10, 11]. In the following, we will use Lewis-Riesenfeld invariants to obtain STA trajectories for H_0 [11, 77]. For harmonic trap transport a known dynamical invariant has the form [11]

$$I(t) = \frac{1}{2m}(p - m\dot{q}_c)^2 + \frac{1}{2}m\omega_0^2[x - mq_c(t)]^2, \quad (4.15)$$

where $q_c(t)$ must satisfy the auxiliary equation

$$\ddot{q}_c + \omega_0^2(q_c - q_0) = 0. \quad (4.16)$$

Note that Eq. (4.16) describes a single-particle classical equation of motion, where $q_0(t)$ is the trajectory of the potential minimum and $q_c(t)$ is the resulting classical particle trajectory.

Solutions of the Schrödinger equation $i\hbar\partial/\partial t\Psi(x, t) = H_0\Psi(x, t)$ can be expressed in terms of weighted transport modes,

$$\Psi(x, t) = \sum_n c_n e^{i\theta_n(t)} \psi_n(x, t), \quad (4.17)$$

where $\psi_n(x, t)$ are orthonormal eigenstates of the invariant I , satisfying $I(t)\psi_n(x, t) = \lambda_n\psi_n(x, t)$, c_n are constants and the Lewis-Riesenfeld phase is given by

$$\theta_n(t) = \frac{1}{\hbar} \int_0^t \langle \phi(t', n) | i\hbar \frac{\partial}{\partial t'} - H_0(t') | \phi(t', n) \rangle dt'. \quad (4.18)$$

In the specific case of harmonic transport, the resulting transport modes in Eq. (4.17) are

$$\chi_n(x, t) = e^{i\theta_n(t)} \psi_n(x, t) = e^{i\theta_n(t)} e^{\frac{i}{\hbar} m \dot{q}_c x} \phi_n(x - q_c), \quad (4.19)$$

where

$$\theta_n(t) = -\frac{i}{\hbar} [(n + 1/2)\hbar\omega_0]t + \int_0^t \frac{m\dot{q}_c^2}{2} dt', \quad (4.20)$$

with $\lambda_n = (n + 1/2)\hbar\omega_0$ and $\phi_n(x)$ are solutions to the Schrödinger equation at $t = 0$, i.e. harmonic eigenstates.

To ensure $I(t)$ and $H_0(t)$ agree at initial and final times, we set $[I(t), H_0(t)] = 0$ for $t = 0, t_f$. This is equivalent [via Eq. (4.16) and Eq. (4.19)] to the boundary

conditions

$$\begin{aligned} q_c(0) &= 0, & q_c(t_f) &= d, \\ \dot{q}_c(0) = \ddot{q}_c(0) &= 0, & \dot{q}_c(t_f) = \ddot{q}_c(t_f) &= 0. \end{aligned} \quad (4.21)$$

The key idea is that $q_c(t)$ can be chosen first, for example to be a polynomial that satisfies the boundary conditions in Eq. (4.21), and then $q_0(t)$ can be inverse engineered using Eq. (4.16).

Throughout this chapter we enforce further boundary conditions on $q_c(t)$, namely

$$q_c^{(3)}(t') = q_c^{(4)}(t') = 0, \text{ for } t = 0, t_f, \quad (4.22)$$

so that the resulting trap trajectory $q_0(t)$ ensures the trap is at rest for initial and final times. In the following, we will use three different auxiliary functions $q_c(t)$ and calculate the corresponding STA trajectories $q_0(t)$.

Polynomial Function $q_{c,1}(t)$: One of the simplest choices for an auxiliary function is a polynomial ansatz $q_{c,1}(t)$ [11], i.e.

$$q_{c,1}(t) = \sum_{j=1}^J a_j t^j \quad (4.23)$$

where J is the number of boundary conditions. For the boundary conditions in Eq. (4.21) and Eq. (4.22), $J = 10$ and we solve for the a_j to get $q_{c,1}(t)$. We then use Eq. (4.16) to produce $q_{0,1}(t)$. Examples of $q_{c,1}(t)$ and $q_{0,1}(t)$ can be seen in Fig. 4.2 (a) and (b) respectively (blue dot-dashed lines).

Quasi-optimal function $q_{c,2}(t)$: Moving beyond the simple polynomial ansatz for q_c , we consider a trajectory introduced in [139] as a quasi-optimal solution to minimizing the quartic term in the potential $(1/2)m\omega_0^2[x - q_0(t)]^2 - \beta[x - q_0(t)]^4$. We label this auxiliary function $q_{c,2}(t)$ and our motivation for using

this function is that it should reduce the effect of the anharmonic contribution within H_s . This auxiliary function was derived using Pontryagin's maximal principle, and relies on first calculating a function f_c that minimises the quartic term contribution to the potential during transport [139],

$$f_c(t) = \frac{3d}{8} \left(1 - 2\frac{t}{t_f}\right)^{7/3} + \frac{7d}{4} \frac{t}{t_f} - \frac{3d}{8}. \quad (4.24)$$

This function f_c does not satisfy the boundary conditions in Eq. (4.21) and it is the root of a complex valued equation [139]. We simplify the definition of f_c , by mapping f_c from $(0, t_f/2)$ to $(t_f/2, t_f)$ appropriately. We also enforce the boundary conditions from Eq. (4.21),

$$q_{c,2}(t) = \begin{cases} 0, & t \leq 0 \\ f_c(t), & 0 < t < t_f/2 \\ -f_c(t_f - t) + d, & t_f/2 < t < t_f \\ d, & t \geq t_f \end{cases}. \quad (4.25)$$

To calculate $q_{0,2}(t)$, it is convenient to define $f_u(t) = 1/\omega_0^2 f_c''(t_f - t)$ where

$$f_u(t) = \frac{14d}{3\omega_0^2 t_f^2} \left(2\frac{t}{t_f} - 1\right)^{1/3}. \quad (4.26)$$

Similarly we first consider f_u on $(t_f/2, t_f)$ and map appropriately to $(0, t_f/2)$, and obtain

$$q_{0,2}(t) = \begin{cases} 0, & t \leq 0 \\ f_c(t) + f_u(t_f - t), & 0 < t < t_f/2 \\ -f_c(t_f - t) - f_u(t) + d, & t_f/2 < t < t_f \\ d, & t \geq t_f \end{cases}, \quad (4.27)$$

that has discontinuities at $t = 0, t = t_f/2$ and $t = t_f$. These jump-points may be difficult to implement practically, so we smooth $q_{c,2}(t)$ in a time-interval of length t_T around the jump points, using polynomial interpolation. Later we will show that high performance can be achieved even with this smoothing process, and that the exact time-interval chosen is not critical to robust and high-fidelity transport. Using Eq. (4.16) we can now calculate $q_{0,2}(t)$,

$$q_{0,2}(t) = \begin{cases} p_0''(t)/\omega_0^2 + p_0(t), & 0 \leq t < t_0 \\ f_c(t) + f_u(t_f - t), & t_0 \leq t \leq t_1 \\ p_1''(t)/\omega_0^2 + p_1(t), & t_1 < t < t_2 \\ -f_c(t_f - t) - f_u(t) + d, & t_2 \leq t \leq t_3 \\ p_2''(t)/\omega_0^2 + p_2(t), & t_3 \leq t \leq t_f \end{cases}, \quad (4.28)$$

where $t_0 = t_T$, $t_1 = (t_f - t_T)/2$, $t_2 = (t_f + t_T)/2$ and $t_3 = t_f - t_T/2$. By design, the polynomials $p_j(t)$ are matched to $f_c(t)$ and $-f_c(t)$ on the appropriate boundary points. Throughout this chapter we choose $t_T = t_f/8$. An example of $q_{c,2}(t)$ and $q_{0,2}(t)$ can be seen in Fig. 4.2 (a) and (b), respectively (green dashed lines).

Quasi-optimal classical function $q_{c,3}(t)$: Lastly we use a quasi-optimal classical auxiliary function as described in [76]. This auxiliary function is also derived via transport time-minimisation in [78]. One motivation for this function is to consider the classical version of the particle transport problem. The intuitive optimal strategy in this case is to maximally accelerate the particle during the first half of the transport, and maximally decelerate the particle in the second half of the transport. In [76] a sudden initial and final displacement of the potential is also included; we omit this since these displacements will occur within the smoothing intervals. We call this auxiliary function the

quasi-optimal classical function, and define it by

$$q_{c,3}(t) = \begin{cases} 2d \left(\frac{t}{t_f}\right)^2, & 0 \leq t < \frac{t_f}{2} \\ d \left[1 - 2 \left(\frac{t}{t_f} - 1\right)^2\right], & \frac{t_f}{2} < t \leq t_f \end{cases}. \quad (4.29)$$

We obtain $q_{0,3}$ using Eq. (4.16), giving

$$q_{0,3}(t) = \begin{cases} 0, & t \leq 0 \\ 2d \left[\left(\frac{t}{t_f}\right)^2 + \frac{2}{\omega_0^2 t_f^2} \right], & 0 < t < \frac{t_f}{2} \\ -2d \left(\frac{t}{t_f} - 1\right)^2 - d \left(\frac{4}{\omega_0^2 t_f^2} - 1\right), & \frac{t_f}{2} < t < t_f \\ d, & t \geq t_f \end{cases}. \quad (4.30)$$

We perform the same smoothing procedure as in the previous section. In the next section we investigate the impact smoothing has on fidelity for this trajectory. Examples of $q_{c,3}(t)$ and $q_{0,3}(t)$ can be seen in Fig. 4.2 (a) and (b) respectively (solid red lines).

4.4.2 Derivation of eSTA control functions

To derive the eSTA control function, we must calculate $\vec{\epsilon}$ in Eq. (4.9). In Fig. 4.1 (b) the improved eSTA control vector is shown schematically, with $\vec{\lambda}_s = \vec{\lambda}_0 + \vec{\epsilon}$. $\vec{\lambda}_0$ characterises the STA control function, while $\vec{\epsilon}$ parameterises the eSTA correction. The purpose of this distinction is to highlight how eSTA improves the control of a system, starting with an idealised STA system with control vector $\vec{\lambda}_0$.

Now we wish to parameterise explicitly the eSTA modification and, without loss of generality, we can simplify our chosen parameterisation by choosing $\vec{\lambda}_0 = \vec{0}$. This allows us to define the new improved eSTA control function $Q_j(\vec{\epsilon}, t)$ as the sum of the original STA control function and a second function

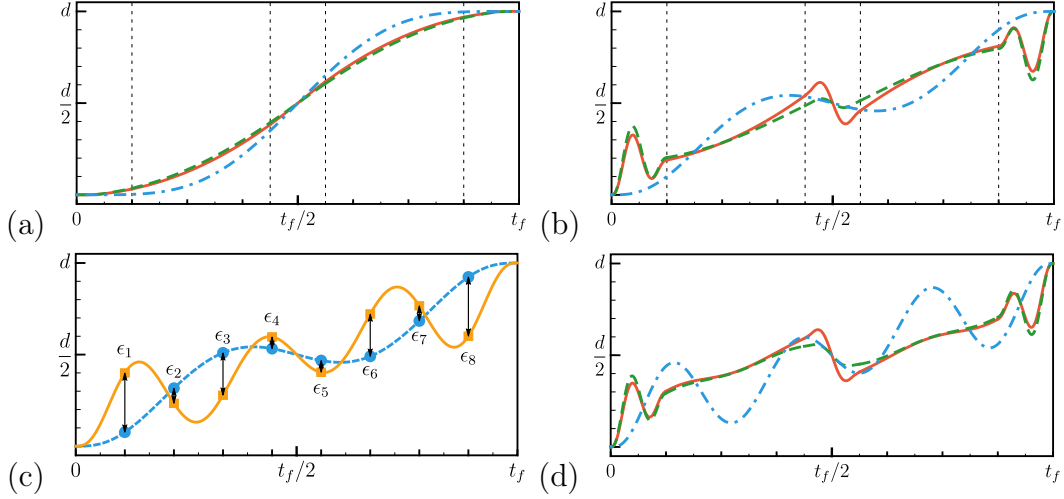


FIGURE 4.2: Plot of STA and eSTA control functions. (a) Plot of the auxiliary functions, $q_{c,1}(t)$ (dot-dashed blue), $q_{c,2}(t)$ (dashed green) and $q_{c,3}(t)$ (solid red). In each of these plots $t_f/\tau = 0.8$ and $d = \lambda/2\sigma$ (one lattice site). (b) Corresponding plots of the STA transport functions, $q_{0,1}(t)$ (dot-dashed blue), $q_{0,2}(t)$ (dashed green) and $q_{0,3}(t)$ (solid red). (c) Example of the vector components of the eSTA correction $\vec{\epsilon}$, with $q_{0,1}$ (dashed blue) and Q_1 (solid orange) shown for $t_f/\tau = 0.8$ and $d = \lambda/2\sigma$. (d) Examples of the eSTA control functions. The vertical dashed lines in plots (a) and (b) indicate the smoothing boxes of length $t_f/8$ about the discontinuities in $q_{c,2}$, $q_{0,2}$, $q_{c,3}$ and $q_{0,3}$.

$$\Delta q_{0,j}(\vec{\epsilon}, t),$$

$$Q_j(\vec{\epsilon}, t) = q_{0,j}(t) + \Delta q_{0,j}(\vec{\epsilon}, t). \quad (4.31)$$

We now have the freedom to define $\Delta q_{0,j}$ and the $\vec{\epsilon}$ parameterisation in any manner that is convenient, provided that $Q_j(\vec{\epsilon}, t)$ remains consistent with the boundary conditions of $q_{0,j}(t)$.

We define $\vec{\epsilon}$ by values that $\Delta q_{0,j}$ takes for equally spaced points in time during the transport. It is then convenient to set $\Delta q_{0,j}$ to be a polynomial

$$\Delta q_{0,j}(\vec{\epsilon}, t) = \sum_{l=0}^{L+5} b_l t^l, \quad (4.32)$$

that satisfies

$$\begin{aligned}\Delta q_{0,j}(t') &= 0, & t = 0, t_f \\ \frac{\partial^n}{\partial t^n} \Delta q_{0,j}(t') &= 0, & t = 0, t_f \text{ and } n = 1, 2, \\ \Delta q_{0,j} \left(\frac{l t_f}{L} \right) &= \epsilon_l, & l = 1, \dots, L.\end{aligned}\tag{4.33}$$

We choose $L = 8$ as a good compromise between numerical implementation and optimisation freedom, further details can be found in [132].

To implement eSTA for a given trajectory, we calculate $\vec{\epsilon}$ using Eq. (4.9). The states $|\chi_n(s)\rangle$ are known analytically from Eq. (4.19), and so the integrals G_n and K_n can be calculated for each n . We choose $N = 4$ for all the results presented in this chapter as terms beyond $N = 4$ do not have an impact on the resulting fidelities or robustness, for this physical setting.

Both $\Delta q_{0,j}$ and $\vec{\epsilon}$ are illustrated in Fig. 4.2 (c), with the STA trajectory $q_{0,1}(t)$ (dot-dashed blue line) and the improved eSTA trajectory $Q_1(\vec{\epsilon}, t)$ (solid orange line) shown for $t_f/\tau = 0.8$. The magnitude of the $\vec{\epsilon}$ components ϵ_l are shown explicitly as changes to the original STA trajectory at the times $l t_f/L$, where $l = 1, \dots, L$ and $L = 8$.

4.4.3 Fidelities for STA and eSTA schemes

We investigate the fidelities using STA and eSTA by numerically simulating the Schrödinger equation with the lattice Hamiltonian from Eq. (4.11), for short transport times. We choose $m = 133$ amu (^{133}Cs), $\lambda = 866$ nm and $\alpha = 150$, motivated by the physical values stated for lattice transport near the quantum speed limit in [76]. This choice of units correspond to a natural time unit of $\tau = 20 \mu\text{s}$, where τ is approximately the quantum speed limit for this transport given in [76].

We first consider the fidelity of the STA trajectories $q_{0,1}(t)$, $q_{0,2}(t)$ and $q_{0,3}(t)$,

and the results are shown in Fig. 4.3. The STA trajectories based on quasi-optimal solutions $[q_{0,2}(t)$ and $q_{0,3}(t)]$ perform better than a simple polynomial ansatz $[q_{0,1}(t)]$. We now fix a reference fidelity $F_R = 0.9$, and we see that both $q_{0,2}(t)$ and $q_{0,3}(t)$ have $F > F_R$ for $t_f/\tau \gtrsim 1.2$, while $t_f/\tau \gg 1.5$ is required for $q_{0,1}(t)$. Since the performance of STA is already optimal for $t_f/\tau \approx 1.45$, we will focus on the region $t_f/\tau < 1.5$.

The fidelities for the three eSTA optimised trajectories $Q_1(t)$, $Q_2(t)$ and $Q_3(t)$ are also shown in Fig. 4.3. They show improvement over their corresponding STA trajectories for the transport times considered. As with the STA trajectories, the eSTA trajectories also show that the quasi-optimal solutions out-perform the polynomial ansatz. Furthermore, the eSTA trajectories produce higher fidelities for shorter times than the STA trajectories; $Q_{0,2}(t)$ has $F > F_R$ for $t_f/\tau \gtrsim 1.025$ and $Q_{0,3}(t)$ has $F > F_R$ for $t_f/\tau \gtrsim 0.98$.

As a side remark, we investigated whether the smoothing we performed on the trajectories had a significant impact on fidelity. As an example, in inset of Fig. 4.3 the fidelities for different smoothing possibilities are shown for $Q_3(t)$. It was found that the smoothing interval t_T was not critical in obtaining high fidelities. While the highest fidelity is obtained for the fully discontinuous trajectory (dashed line), very similar results are found using a smoothing interval even as large as $t_T = t_f/8$ (dashed line). An alternative approach is to use a fully discontinuous $q_{c,3}(t)$ and perform a smoothing procedure on the resulting eSTA trajectory $Q_{0,3}(t)$. However, this was found to give poorer performance, as shown in the inset of Fig. 4.3 (dash-dotted line). Thus, for the results in this chapter the STA trajectories $q_{c,j}(t)$ were smoothed using $t_T = t_f/8$, and then the eSTA trajectories $Q_j(t)$ were calculated.

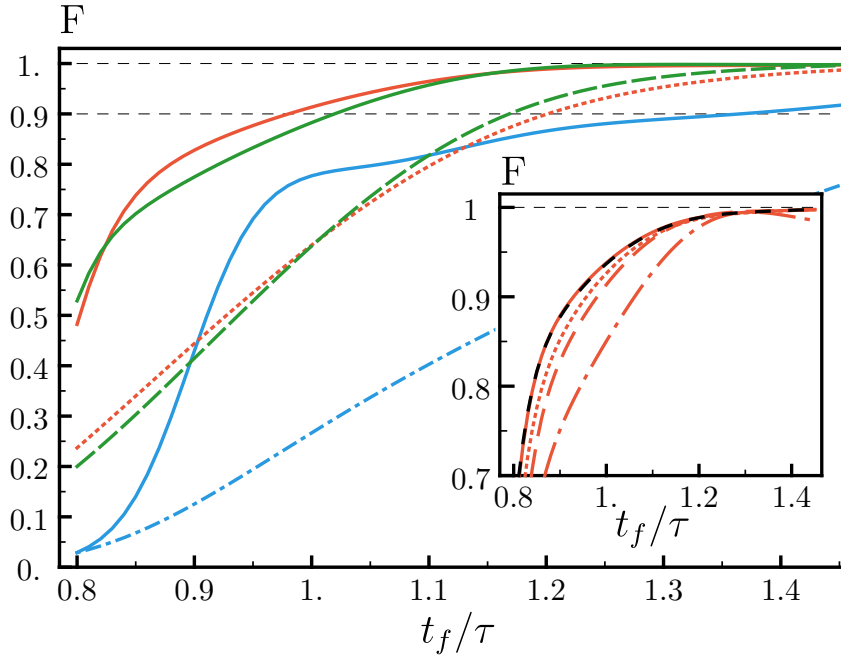


FIGURE 4.3: Fidelity F versus final time t_f , for $\delta = 0$. The fidelities for the STA trajectories are given by the broken lines; $q_{0,1}(t)$ (dot-dashed blue), $q_{0,2}(t)$ (dashed green) and $q_{0,3}(t)$ (dotted red). The corresponding eSTA optimised fidelities are solid lines; $Q_1(t)$ (blue), $Q_2(t)$ (green) and $Q_3(t)$ (red). Inset of (a): Fidelity F versus final time t_f using Q_3 with different smoothing options. The solid-red line uses a fully discontinuous $q_{c,3}$, and the dashed-black line on top of it uses $q_{c,3}$ with only the center discontinuity smoothed over a $t_T = t_f/16$ interval. The dotted-red line uses $q_{c,3}$ smoothed in an interval of length $t_T = t_f/16$ around the three discontinuities and the dashed-red line uses $q_{c,3}$ smoothed in an interval of length $t_T = t_f/8$ around the three discontinuities. The dot-dashed line uses a discontinuous $q_{c,3}$ and then a smoothed $q_{0,3}$.

4.5 eSTA Control Function Deviation

Before starting with an examination of the robustness of eSTA, we will first examine the related question of how much the eSTA control function deviates when parameters within the potential are slightly changed. We define the deviation \mathcal{C}_Q of the control function Q . The motivation for examining \mathcal{C}_Q is an expectation that if the control function does not depend strongly on a specific parameter of the potential, then this could result in stability concerning systematic errors in that parameter.

In detail, we define the deviation \mathcal{C}_Q as

$$\mathcal{C}_Q := \lim_{\delta \rightarrow 0} \frac{1}{\delta} \|Q(\delta) - Q(0)\| = \left\| \frac{\partial}{\partial \delta} Q \Big|_{\delta=0} \right\|. \quad (4.34)$$

where δ is some variation of the potential.

There is freedom in the choice of norm in Eq. (4.34), in the following we will use the L_1 norm

$$\|Q(\delta)\| = \int_0^{t_f} ds |Q(\delta, s)|. \quad (4.35)$$

As in Eq. (4.31), we assume that the solution to the eSTA system with Hamiltonian $\mathcal{H}(\delta)$ takes the form

$$Q(\delta, t) = q_0(\delta, t) + \Delta q_0[\vec{\epsilon}(\delta), t], \quad (4.36)$$

where $q_0(\delta, t)$ is the STA control function that solves the approximate STA system, and Δq_0 is a polynomial as defined in Eq. (4.33). We set $\Delta q_0[\vec{0}, t] = 0$ and assume Δq_0 does not depend on the STA control function $q_0(\delta, t)$. We also have that

$$\begin{aligned} \frac{\partial Q}{\partial \delta} \Big|_{\delta=0} &= \frac{\partial q_0}{\partial \delta} \Big|_{\delta=0} + \frac{\partial}{\partial \delta} \Delta q_0(\vec{\epsilon}(0), t) \Big|_{\delta=0} \\ &= \frac{\partial q_0}{\partial \delta} \Big|_{\delta=0} + \sum_{j=1}^N \frac{\partial \Delta q_0}{\partial \epsilon_j}(\vec{\epsilon}(0), t) \frac{\partial \epsilon_j}{\partial \delta} \Big|_{\delta=0}. \end{aligned} \quad (4.37)$$

Using the definition of \mathcal{C}_Q in Eq. (4.34) we obtain

$$\mathcal{C}_Q := \left\| \frac{\partial q_0}{\partial \delta} \Big|_{\delta=0} + \sum_{j=1}^N \frac{\partial \Delta q_0}{\partial \epsilon_j}(\vec{\epsilon}(0), t) \frac{\partial \epsilon_j}{\partial \delta} \Big|_{\delta=0} \right\| \quad (4.38)$$

By using the eSTA formalism, we can calculate $\frac{\partial \epsilon_j}{\partial \delta}$ explicitly as shown in Appendix 4.9.1. Starting from Eq. (4.38), we can also derive an upper bound of

the quantity \mathcal{C}_Q :

$$\begin{aligned} \mathcal{C}_Q &\leq \left\| \frac{\partial q_0}{\partial \delta} \Big|_{\delta=0} \right\| + \sum_{j=1}^N \left\| \frac{\partial \Delta q_0}{\partial \epsilon_j}(\bar{\epsilon}(0), t) \right\| \left\| \frac{\partial \epsilon_j}{\partial \delta} \Big|_{\delta=0} \right\| \\ &\leq \left\| \frac{\partial q_0}{\partial \delta} \Big|_{\delta=0} \right\| + \left[\max_j \left\| \frac{\partial \Delta q_0}{\partial \epsilon_j}(\bar{\epsilon}(0), t) \right\| \right] \sum_{j=1}^N \left\| \frac{\partial \epsilon_j}{\partial \delta} \Big|_{\delta=0} \right\|. \end{aligned} \quad (4.39)$$

The first term $\partial q_0/\partial \delta$ is the deviation of the STA trajectory. The second term is a measure of the eSTA dependence with respect to the control function Q , and this is the term we wish to investigate. Note that the calculation of \mathcal{C}_Q can be done fully analytically as shown in Appendix 4.9.1, and so requires far less computation than the numerical derivative of the fidelity which we will consider in the next section. We highlight here that \mathcal{C}_Q offers potential as a tool to evaluate and classify possible eSTA trajectories in lieu of full numerical treatment. As an example, we consider a correlated error in the lattice amplitude U_0 and wavenumber k_0 :

$$V_{\text{err}}^c(x, t) = U_0(1 + \delta) \sin^2 \left\{ k_0 \frac{[x - Q_j(t)]}{\sqrt{(1 + \delta)}} \right\}, \quad (4.40)$$

such that $\omega = \omega_0 = \sqrt{\frac{2U_0}{m}} k_0$ is kept constant, hence the STA trajectories do not depend on δ . Systematic errors in the lattice amplitude or wavenumber alone will be considered in following sections. This error potential allows us to focus on applying \mathcal{C}_Q to eSTA control functions, since the STA trajectories $q_{0,j}$ do not depend on δ .

The corresponding results of \mathcal{C}_Q can be seen in Fig. 4.4. We find that the trajectories Q_2 and Q_3 (solid lines) show a lower deviation with changes in δ than the trajectory Q_1 . The upper bound on \mathcal{C}_Q from Eq. (4.39) is also shown and we see that the upper bound can be also used for classifying the different schemes. From these results, one would expect that the trajectories Q_2 and Q_3 are more stable concerning a systematic error δ . This will be examined in the

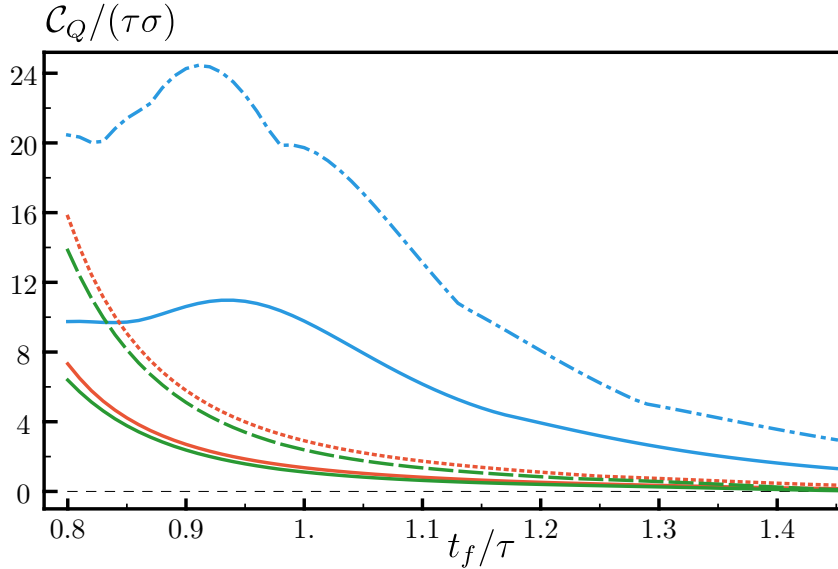


FIGURE 4.4: Control function deviation \mathcal{C}_Q versus t_f for correlated systematic error. Trajectories $Q_1(t)$ (solid blue), $Q_2(t)$ (solid green) and $Q_3(t)$ (solid red). Upper bound of \mathcal{C}_Q : trajectories $Q_1(t)$ (dot-dashed blue), $Q_2(t)$ (dashed green) and $Q_3(t)$ (dotted red).

next section in detail and will be shown to be the case.

4.6 Robustness to Systematic Errors

In this section we compare the robustness of the eSTA and STA trajectories by considering how the fidelity changes under three systematic errors in the lattice potential.

We first consider the correlated error V_{err}^c introduced in the last section for a specific final time and then define a sensitivity S for a given trajectory. We compare eSTA to STA using three systematic errors: the correlated error V_{err}^c and two further errors, an error in the lattice amplitude V_{err}^A and an error in the lattice wavenumber V_{err}^k . The amplitude and wavenumber errors can occur in the physical implementation of lattice potentials [140].

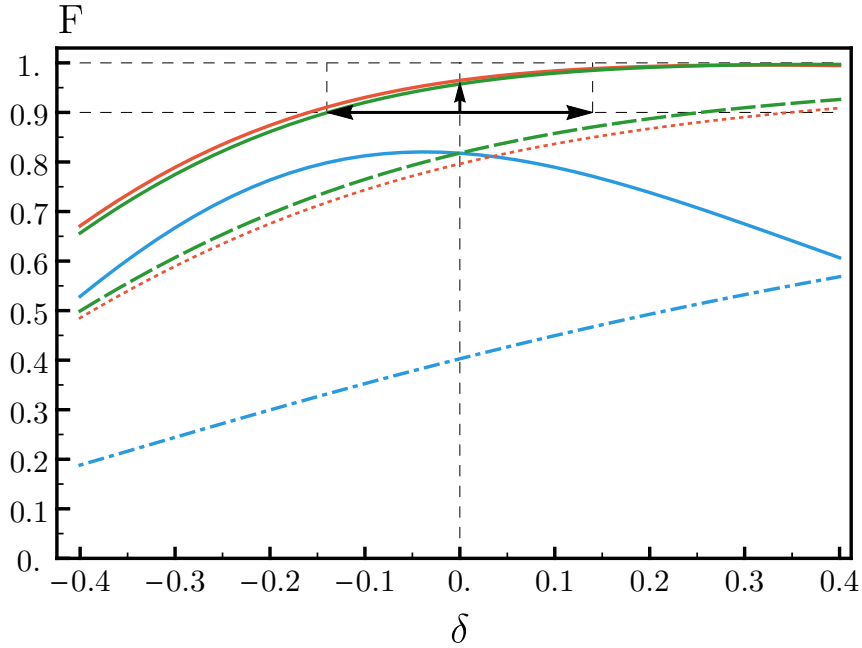


FIGURE 4.5: Fidelity at $t_f/\tau = 1.1$ versus δ for correlated error. The fidelities for the STA trajectories are shown, for $q_{0,1}(t)$ (dot-dashed blue), $q_{0,2}(t)$ (dashed green) and $q_{0,3}(t)$ (dotted red). The corresponding eSTA optimised fidelities are $Q_1(t)$ (solid blue), $Q_2(t)$ (solid green) and $Q_3(t)$ (solid red). The horizontal solid-black arrows show $|\delta|$, such that $F(\delta) > F_R = 0.9$ for Q_2 (solid green). The vertical solid-black arrow at $\delta = 0$ is $F(\delta = 0) - F_R$. These quantities are used in the definition of the systemic error bound \mathcal{B} , in Eq. (4.45).

We define δ to be the strength of the systematic error, and define two further error potentials: The lattice amplitude error potential is given by

$$V_{\text{err}}^A(x, t) = U_0(1 + \delta) \sin^2 \{k_0 [x - Q_j(t)]\}, \quad (4.41)$$

and the wavenumber error potential is

$$V_{\text{err}}^k(x, t) = U_0 \sin^2 \left\{ k_0 \sqrt{1 + \delta} [x - Q_j(t)] \right\}, \quad (4.42)$$

with $\omega = \omega_0 \sqrt{1 + \delta}$ in both cases.

As a first step, we consider the correlated error V_{err}^c for a fixed final time of $t_f/\tau = 1.1$.

In Fig. 4.5, the fidelity F versus the error strength δ is shown for the three eSTA and three STA trajectories. The STA trajectories $q_{0,2}$ and $q_{0,3}$ show similar fidelities about $\delta = 0$, and the same is true for the eSTA trajectories Q_2 and Q_3 . We see significant higher fidelities of the eSTA schemes Q_2 and Q_3 over the STA schemes $q_{0,2}$ and $q_{0,3}$, respectively. While the eSTA polynomial ansatz Q_1 has much higher fidelity than the STA $q_{0,1}$, Q_1 has fidelity $F < 0.9$ for all δ in the range considered.

We see that there is no significant change in the fidelity for the eSTA trajectories in a neighborhood about $\delta = 0$, and that even for larger values of δ the eSTA trajectories maintain their higher fidelity over their related STA trajectories.

We will show later that even $\partial F/\partial\delta$ at $\delta = 0$ is smaller for the eSTA trajectories Q_2 and Q_3 , than the STA trajectories $q_{0,2}$ and $q_{0,3}$ (see Fig. 4.6). This can also already be seen in Fig. 4.5, as the slopes of the eSTA lines (solid green and red line) are less than those for the STA lines (dashed-green line and dotted-red line).

Note that for V_{err}^c , increasing δ corresponds with deepening of the lattice. As the lattice is deepened we find increased fidelity and stability for both Q_2 and Q_3 , and $q_{0,2}$ and $q_{0,3}$.

4.6.1 Systematic Error Sensitivity

To examine the robustness of eSTA quantitatively for the three types of systematic errors we define the sensitivity

$$S := \left| \frac{\partial F}{\partial \delta} \Big|_{\delta=0} \right|. \quad (4.43)$$

A smaller value of S corresponds to a more robust protocol, i.e. less sensitivity to the error induced by δ . We evaluate S for the different errors and trajectories numerically around $\delta = 0$ by simulating the full transport. Note that using

time-dependent perturbation theory, S can be expressed as

$$S = \frac{1}{\hbar} \left| \int_0^{t_f} dt \langle \Psi_T(t) | \frac{\partial H}{\partial \delta} \Big|_{\delta=0} | \Psi_0(t) \rangle \langle \Psi_T(t_f) | \Psi_0(t_f) \rangle \right|, \quad (4.44)$$

where $|\Psi_0(0)\rangle$ is the initial state, $|\Psi_T(t_f)\rangle$ is the target state and $|\Psi_0(t)\rangle$ is the time-evolved solution of the Schrödinger equation.

In the following, we will evaluate both eSTA and STA for the three systematic errors stated previously. Since we are interested in trajectories that give the highest fidelity, we restrict our focus to Q_2 and Q_3 ($q_{0,2}$, $q_{0,3}$ respectively).

In Fig. 4.6 (c) we consider the correlated error V_{err}^c . For $t_f/\tau \geq 0.95$, eSTA shows reduced sensitivity over STA. Note that the fidelities are also higher in this t_f range (see Fig. 4.3). We also find that Q_2 and Q_3 in Fig. 4.6 (c) both agree qualitatively with their analytic \mathcal{C}_Q behavior in Fig. 4.4.

We show the sensitivity of eSTA and STA versus t_f/τ for V_{err}^A in Fig. 4.6 (a) and V_{err}^k in Fig. 4.6 (b). For these errors, the eSTA trajectories (solid lines) generally have lower sensitivities than the STA trajectories (dashed and dotted lines).

If we first consider longer transport times t_f , S is approaching zero for every trajectory. This behavior is expected given the Adiabatic theorem; as t_f approaches the adiabatic limit, small perturbations in the potential will have less impact on the instantaneous eigenstate of the system. Thus, $F \rightarrow 1$, and $S \rightarrow 0$.

For very short final times ($t_f/\tau < 1$), S becomes a less useful description of robustness since the fidelity is rapidly decreasing for all trajectories. Hence a more useful quantity would consider the fidelity F and sensitivity S together, and this motivates us to define a new quantity in the next section that we call the systemic error bound.

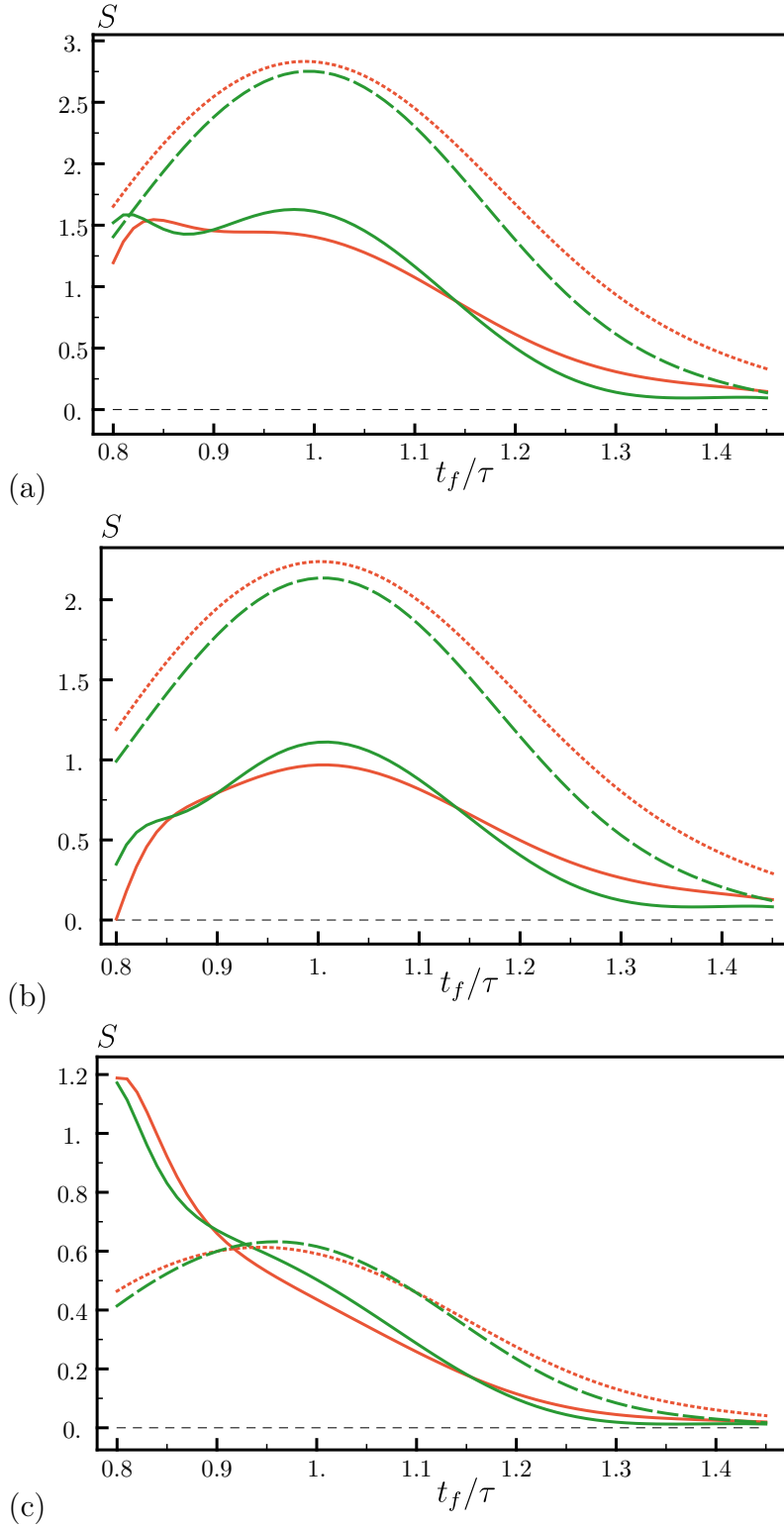


FIGURE 4.6: Sensitivity S for systematic errors versus t_f for (a) amplitude error V_{err}^A , (b) wavenumber error V_{err}^k , (c) correlated error V_{err}^c . eSTA trajectories: Q_2 (solid green) and Q_3 (solid red).

STA trajectories: $q_{0,2}$ (dashed green) and $q_{0,3}$ (dotted red).

4.6.2 Systematic Error bound

For practical implementation, we are interested in protocols that exceed a chosen threshold fidelity F_R while also having stability against a systematic error within a certain bound. To address these concerns, we now define a new quantity \mathcal{B} called the systematic error bound. For a given final time, we approximate a bound \mathcal{B} on the strength of the systematic error δ , such that for $|\delta| < \mathcal{B}$ we ensure that the fidelity satisfies $F > F_R$, with F_R a given reference fidelity. We can approximate \mathcal{B} by assuming a linear dependence of the fidelity on δ , with

$$\mathcal{B} = \begin{cases} \frac{F(\delta=0) - F_R}{S} & : F(\delta = 0) > F_R \\ 0 & : F(\delta = 0) \leq F_R \end{cases}, \quad (4.45)$$

where for simplicity we have used the convention that $\mathcal{B} = 0$ for $F(\delta = 0) \leq F_R$. The systematic error bound \mathcal{B} indicates that for a given final time, the trajectory achieves fidelity above F_R for $|\delta| < \mathcal{B}$. Hence, higher values of \mathcal{B} mean higher fidelity and lower sensitivity. (In contrast, higher values of S correspond with decreased stability at a given δ .)

In Fig 4.5 we show a specific example of the quantities needed to calculate \mathcal{B} . For Q_2 (solid-green line), the horizontal solid-black arrows in Fig. 4.5 show $|\delta|$ symmetric about $\delta = 0$ such that $F(\delta) > F_R = 0.9$. To calculate \mathcal{B} , we find the difference $F(\delta = 0) - F_R$ (the vertical solid arrow in Fig 4.5), and then scale by $1/S$. Note that for this example, S can be seen on Fig. 4.6 (c).

The systematic error bound \mathcal{B} is shown in Fig. 4.7 for the same trajectories and errors as shown previously in Fig. 4.6. In Fig. 4.7 we choose $F_R = 0.9$ and note that the quasi-optimal eSTA trajectories Q_2 and Q_3 show significant improvement over the polynomial ansatz eSTA Q_1 . We include the polynomial ansatz trajectories Q_1 and $q_{0,1}$, as a reference case to highlight the usefulness of \mathcal{B} as a robustness measure. For all three errors the eSTA trajectories achieve a higher or equal \mathcal{B} over their STA counterparts, and this reflects the previous

fidelity results (Fig. 4.3) and sensitivity results (Fig. 4.6).

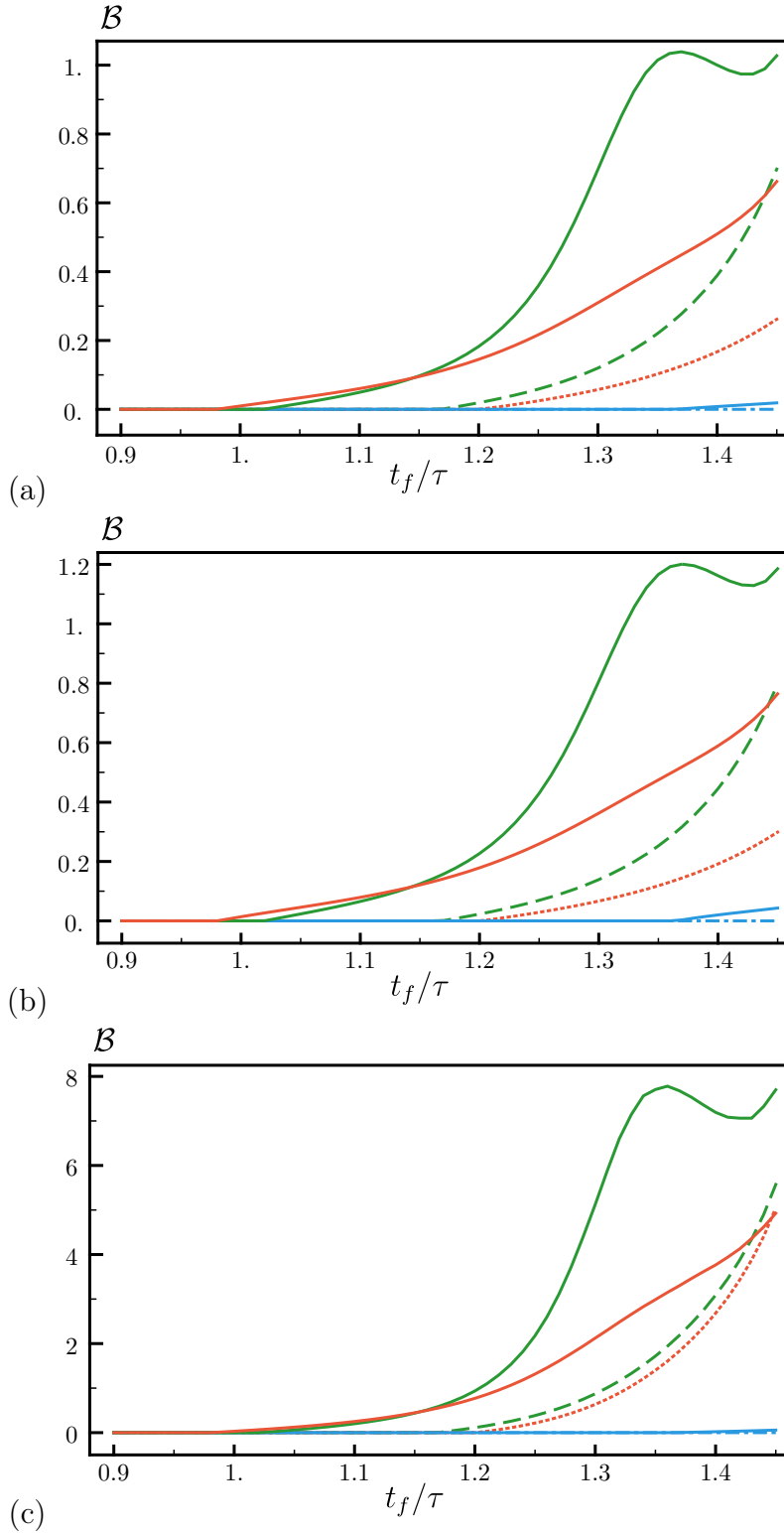


FIGURE 4.7: Systematic error bound \mathcal{B} versus t_f with $F_R = 0.9$ for (a) amplitude error V_{err}^A , (b) wavenumber error V_{err}^k , (c) correlated error V_{err}^c . eSTA: Q_2 (solid green) and Q_3 (solid red). STA: $q_{0,2}$ (dashed green) and $q_{0,3}$ (dotted red).

For $t_f \rightarrow \infty$, for both the eSTA and STA error bounds $\mathcal{B} \rightarrow \infty$, since as discussed in the last section $S \rightarrow 0$ in the adiabatic limit. This is not an inherent problem with \mathcal{B} , since we are interested in applying \mathcal{B} in regions far from adiabaticity. Thus we restrict our investigation to $t_f/\tau < 1.45$, as shown in Fig. 4.7.

In Fig. 4.7 we note that the three error types produce similar \mathcal{B} behavior for each trajectory, although the magnitude of \mathcal{B} is different in each case. We find that from $t_f \geq 1$ the eSTA trajectories Q_2 and Q_3 give larger values of \mathcal{B} than the STA trajectories $q_{0,2}$ and $q_{0,3}$. These values are increasing, indicating that even when the fidelities are very high, a larger value of \mathcal{B} informs us that the eSTA sensitivity must be decreasing faster than the STA sensitivity. In this way the error bound \mathcal{B} gives us a useful comparison between trajectories, as it allows both the fidelity and sensitivity of different trajectories to be compared simultaneously.

4.7 Robustness of eSTA to noise

We now consider the robustness and stability of eSTA with respect to noise. Specifically we consider lattice transport with classical Gaussian white noise in position and lattice amplitude. The noise sensitivity of lattice transport using STA has previously been studied in [35, 140, 141].

We consider a Hamiltonian $\mathcal{H} = H_0(t) + \eta \xi(t)H_1(t)$, where η is the noise strength, $\xi(t)$ is a realisation of the noise and $H_1(t)$ is the operator coupling the system to the noise [142–144]. As shown in Appendix 4.9.2 a master equation can be derived [35, 140]

$$\frac{d}{dt}\rho = -\frac{i}{\hbar} [H_0, \rho] - \frac{\eta^2}{2\hbar^2} [H_1, [H_1, \rho]], \quad (4.46)$$

where H_0 is from Eq. (4.11).

We define the noise sensitivity S_N ,

$$S_N = \left| \frac{\partial F}{\partial (\eta^2)} \right| = \left| \frac{1}{2} \frac{\partial^2 F}{\partial \eta^2} \right|, \quad (4.47)$$

and in Appendix 4.9.2 we use a perturbation approach to the master equation [35, 145] to obtain

$$S_N = \frac{1}{\hbar^2} \left| \int_0^t ds \left[\operatorname{Re} \left\{ \langle \Psi_T(s) | H_1^2(s) | \Psi_0(s) \rangle \langle \Psi_0(s) | \Psi_T(s) \rangle \right\} - |\langle \Psi_T(s) | H_1(s) | \Psi_0(s) \rangle|^2 \right] \right|, \quad (4.48)$$

where we use the same notation as in Eq. (4.44) regarding $|\Psi_0(s)\rangle$ and $|\Psi_T(s)\rangle$. We focus on transport of the ground state of the lattice, but the results in this section can be generalised naturally. The quantity S_N in Eq. (4.48) is useful as it allows us measure the system's sensitivity to noise without having to numerically simulate the full open system dynamics, for example using quantum trajectories.

Let us first consider the special case of the adiabatic limit. Let $\psi_0(x)$ be the ground state of the lattice, thus

$$\Psi_0(t, x) = \Psi_T(t, x) = \psi_0[x - Q_j(t)] e^{i\phi(t)}. \quad (4.49)$$

Then Eq. (4.48) simplifies to

$$S_N = t_f C, \quad (4.50)$$

where C is given by

$$C = \frac{1}{\hbar^2} \left| \langle \psi_0 | H_1^2 | \psi_0 \rangle - |\langle \psi_0 | H_1 | \psi_0 \rangle|^2 \right|. \quad (4.51)$$

We again consider the error bound defined in the previous section which combines the fidelity and the sensitivity, defined as

$$\mathcal{B}_N = \begin{cases} \frac{F(\delta=0) - F_R}{S_N} & : F(\delta=0) > F_R \\ 0 & : F(\delta=0) \leq F_R \end{cases}, \quad (4.52)$$

where we again adopt the convention $\mathcal{B}_N = 0$ for $F \leq F_R$. We note that in the adiabatic limit, $\mathcal{B}_N \approx \frac{1-F_R}{C} \cdot \frac{1}{T}$, i.e. the error bound goes to zero for $T \rightarrow \infty$, where $T = t_f/\tau$ (in contrast with the systemic errors considered in the previous section).

4.7.1 Position noise

As a first example we consider position noise described by the potential

$$V_N^P = V[x - Q_j(t) - \sigma\eta\xi(t)], \quad (4.53)$$

with V the lattice potential and σ the unit of space defined in Section 4.4. Using only first-order in η , we have

$$\begin{aligned} H_1^P &= -\sigma \frac{\partial}{\partial x} V[x - Q_j(t)] \\ &= -\sigma U_0 k_0 \sin \{2k_0[x - Q_j(t)]\}. \end{aligned} \quad (4.54)$$

We evaluate Eq. (4.48) using both STA and eSTA trajectories and plot \mathcal{B}_N in Fig. 4.8 (a). The eSTA trajectories again out-perform their STA counterparts, showing a greater \mathcal{B}_N over a larger range of shorter final times.

In Fig. 4.8 (b) we look at larger t_f/τ and we see the STA trajectories (dashed-coloured lines) approach the adiabatic limit (dashed-black line).

Note that when the ground state is known analytically as with the harmonic oscillator, then explicit formulas for the constant C in Eq. (4.51) can be found.

Using the harmonic oscillator ground state as an approximation to the lattice ground state, we obtain an approximation for Eq. (4.51)

$$\begin{aligned} C^P &\approx \frac{1}{2} \left(\frac{U_0 k_0 \sigma}{\hbar} \right)^2 \left[1 - e^{-4k_0^2 \sigma^2} \right] \\ &= \frac{\omega_0^2 \tilde{U}_0}{4} \left[1 - e^{-2/\tilde{U}_0} \right], \end{aligned} \quad (4.55)$$

where $\tilde{U}_0 = U_0/(\hbar\omega_0)$. For the values considered here, $\tau^2 C_P = 0.0112$ and the approximation in Eq. (4.55) gives $\tau^2 C_P \approx 0.0108$.

4.7.2 Amplitude noise

For noise in the lattice amplitude we define the noise potential as

$$V_N^A = [1 + \eta\xi(t)]V[x - Q_j(t)], \quad (4.56)$$

with V the lattice potential. In this case we have

$$H_1^A = V[x - Q_j(t)]. \quad (4.57)$$

The results for the STA and eSTA trajectories are shown Fig. 4.8 (d). As with the position noise, the eSTA trajectories are an improvement over the STA trajectories.

Both noise sources have similar \mathcal{B}_N scales, with the position noise eSTA results showing greater improvement over STA than the amplitude noise eSTA results have over their STA counterparts

In Fig. 4.8 (c) the STA trajectories for amplitude noise are shown for values of t_f/τ approaching the adiabatic limit, and for $t_f/\tau > 4$ they agree.

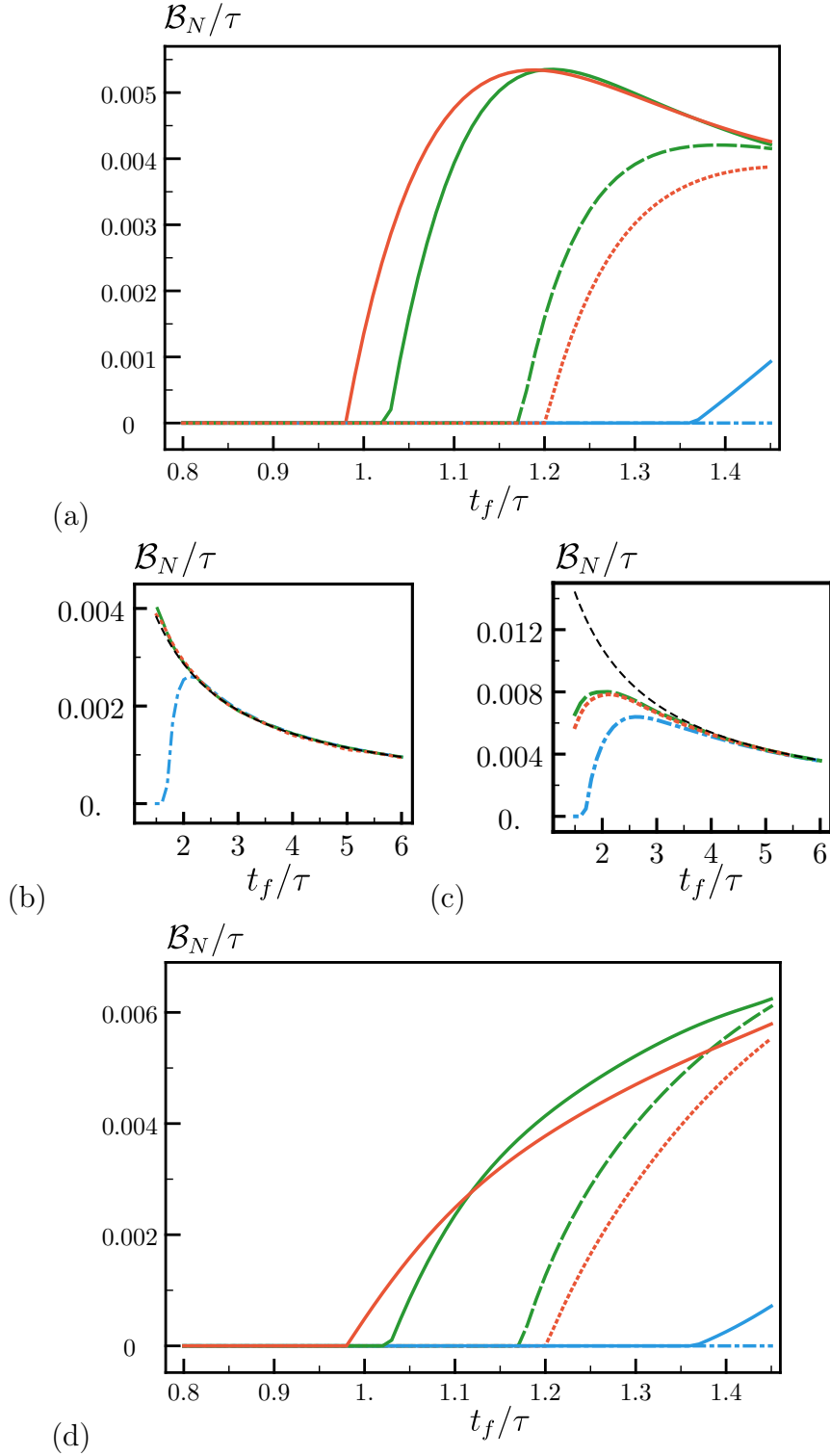


FIGURE 4.8: Noise error bound \mathcal{B}_N versus t_f with $F_R = 0.9$ for: (a) Position noise V_N^P . eSTA trap trajectories $Q_1(t)$ (solid blue), $Q_2(t)$ (solid green) and $Q_3(t)$ (solid red); STA trap trajectories $q_{0,1}(t)$ (dot-dashed blue), $q_{0,2}(t)$ (dashed green) and $q_{0,3}(t)$ (dotted red). (b) Position noise \mathcal{B}_N versus larger t_f using the STA trajectories. All the trajectories converge to the adiabatic limit (dashed black) for large t_f . (c) Amplitude noise \mathcal{B}_N versus larger t_f , again using the STA trajectories. They also converge to the adiabatic limit (dashed black) for large t_f . (d) Amplitude noise V_N^A , with same details as (a).

As with the previous section, we can approximate C^A by using the analytic harmonic ground state with the lattice potential,

$$\begin{aligned} C^A &\approx \frac{1}{8} \left(\frac{U_0}{\hbar} \right)^2 e^{-4k_0^2 \sigma^2} \left(e^{2k_0^2 \sigma^2} - 1 \right)^2, \\ &= \frac{\omega_0^2 \tilde{U}_0^2}{8} e^{-2/\tilde{U}_0} \left(e^{1/\tilde{U}_0} - 1 \right)^2, \end{aligned} \quad (4.58)$$

and again $\tilde{U}_0 = U_0/(\hbar\omega_0)$. The approximation gives $\tau^2 C^A \approx 2.70 \times 10^{-3}$, while the exact value is $\tau^2 C^A = 2.97 \times 10^{-3}$.

4.8 Conclusion

We applied the general eSTA formalism developed in [132] to the the practical problem of atom transport using an optical lattice potential, near the quantum speed limit [76]. By examining the robustness of the eSTA control schemes, we found that the eSTA transport protocols result in higher fidelity and improved robustness against several types of systematic errors and noise errors.

We have provided a general heuristic argument that the eSTA schemes should result in higher fidelities and improved stability compared with the original STA schemes. Furthermore, we have shown strong numerical evidence of this claim by considering noise and systematic errors in the lattice potential.

Finally, we have quantified this increased robustness by defining new measures. These include an eSTA- specific evaluation tool C_Q , that allows possible control functions to be evaluated without full numerical treatment and a practical error bound \mathcal{B} that combines fidelity and sensitivity such that eSTA and STA control functions can be compared qualitatively. In the future the robustness of eSTA schemes and the error bound \mathcal{B} could be considered in further quantum control applications.

4.9 Appendix

4.9.1 Derivation of \mathcal{C}_Q

We can evaluate \mathcal{C}_Q using the formalism of eSTA. As before with eSTA, we write the system Hamiltonian $\mathcal{H}(\delta)$ as an expansion about the STA system that approximates it

$$\mathcal{H}(\delta) = H_0^{\text{STA}}(\delta) + \mu \mathcal{H}_1(\delta) + \mu^2 \mathcal{H}_2(\delta) + \dots \quad (4.59)$$

We generalise the definitions of \vec{K}_n and G_n from the eSTA formalism to include the δ dependence in the Hamiltonian, giving

$$\vec{K}_n(\delta) = \int_0^{t_f} dt \langle \chi_n(t) | \nabla \mathcal{H}_S(\vec{\lambda}_0; t; \delta) | \chi_0(t) \rangle, \quad (4.60)$$

and

$$G_n(\delta) = \int_0^{t_f} dt \langle \chi_n(t) | [\mathcal{H}_S(\vec{\lambda}_0; t; \delta) - \mathcal{H}^{(0)}(\vec{\lambda}_0; t)] | \chi_0(t) \rangle. \quad (4.61)$$

Hence we have that the eSTA control vector is given by

$$\vec{\epsilon}(\delta) \approx - \frac{\left[\sum_{n=1}^N |G_n(\delta)|^2 \right] \left\{ \sum_{n=1}^N \text{Re} \left[G_n^*(\delta) \vec{K}_n(\delta) \right] \right\}}{\left| \sum_{n=1}^N \text{Re} \left[G_n^*(\delta) \vec{K}_n(\delta) \right] \right|^2}. \quad (4.62)$$

Now we look at the derivative with respect to δ and evaluate at $\delta = 0$,

$$\begin{aligned} \frac{\partial}{\partial \delta} \epsilon_j(0) = \epsilon_j(0) & \left\{ \frac{\sum_{n=1}^N 2\text{Re} \left[G_n^*(0) \frac{\partial}{\partial \delta} G_n(0) \right]}{\sum_{n=1}^N |G_n(0)|^2} \right. \\ & + \frac{\sum_{n=1}^N \left\{ \text{Re} \left[K_{n,j}^*(0) \frac{\partial}{\partial \delta} G_n(0) \right] + \text{Re} \left[G_n^*(0) \frac{\partial}{\partial \delta} K_{n,j}(0) \right] \right\}}{\sum_{n=1}^N \text{Re} \left[G_n^*(0) \vec{K}_{n,j}(0) \right]} \\ & + \sum_{j=1}^M \left\{ \sum_{n=1}^N \text{Re} \left[G_n^*(0) \vec{K}_{n,j}(0) \right] \sum_{n=1}^N \text{Re} \left[K_{n,j}^*(0) \frac{\partial}{\partial \delta} G_n(0) \right] \right. \\ & \left. + \text{Re} \left[G_n^*(0) \frac{\partial}{\partial \delta} K_{n,j}(0) \right] \right\} / \sum_{j=1}^M \left| \sum_{n=1}^N \text{Re} \left[G_n^*(0) \vec{K}_{n,j}(0) \right] \right|^2 \left. \right\}. \quad (4.63) \end{aligned}$$

While this expression is detailed, the individual terms are known exactly and can be calculated entirely analytically.

4.9.2 Derivation of S_N

To consider the effect of noise on eSTA protocols, we start with a system obeying the Schrödinger equation

$$i\hbar \frac{\partial}{\partial t} |\Psi\rangle = H_0(t) |\Psi\rangle, \quad (4.64)$$

where $H_0(t) = p^2/2m + V(x, t)$, and V is the potential. We consider noise of the form $\eta \xi(t) H_1(t)$, where $\xi(t)$ is a given noise realisation, $H_1(t)$ is the operator coupling the system to the noise and η is the noise strength [35, 142, 143]. We assume that the statistical expectation $\mathcal{E}[\xi(t)] = 0$, with

$$\mathcal{E}[\xi(t)\xi(t')] = \alpha(t - t'), \quad (4.65)$$

where $\alpha(t - t')$ is the correlation function of the noise. Following the approach taken in [145], a master equation can be derived [35, 140]

$$\frac{d}{dt} \rho = -\frac{i}{\hbar} [H_0, \rho] - \frac{i\eta}{\hbar} [H_1, \langle \xi \rho \rangle], \quad (4.66)$$

where η is the perturbation parameter and ρ is the average over realisations of $\xi(t)$. Now we assume Gaussian white noise, i.e. $\alpha(t-t') = \delta(t'-t)$ and using Novikov's theorem [146], $\langle \xi \rho \rangle = -i\eta/2\hbar [H_1, \rho]$ we obtain

$$\frac{d}{dt}\rho = -\frac{i}{\hbar} [H_0, \rho] - \frac{\eta^2}{2\hbar^2} [H_1, [H_1, \rho]]. \quad (4.67)$$

We define

$$\begin{aligned} \frac{d}{dt}\rho_0 &= -\frac{i}{\hbar} [H_0, \rho_0], \\ |\rho_0(t)\rangle\rangle &= U_0(t, 0)|\rho_0(0)\rangle\rangle, \end{aligned} \quad (4.68)$$

where $|\rho_0(t)\rangle\rangle$ denotes $\rho_0(t)$ written in super-operator notation. Let

$$\mathcal{L}(t)|\rho\rangle\rangle = -\frac{1}{2\hbar^2} [H_1, [H_1, \rho]], \quad (4.69)$$

then [145] [35]

$$\begin{aligned} |\rho(t)\rangle\rangle &= |\rho_0(t)\rangle\rangle + \eta^2 \int_0^t ds U_0(t, s) \mathcal{L}(s) U_0(s, 0) |\rho_0(0)\rangle\rangle + \mathcal{O}(\eta^4) \\ &= |\rho_0(t)\rangle\rangle + \eta^2 \int_0^t ds U_0(t, s) \mathcal{L}(s) |\rho_0(s)\rangle\rangle + \mathcal{O}(\eta^4). \end{aligned} \quad (4.70)$$

We denote the target state as $|\Psi_T\rangle$ and set $|\rho_T\rangle\rangle = |\Psi_T\rangle\langle\Psi_T|$. The fidelity is then

$$\begin{aligned} \mathbb{F} &= \langle\langle \rho_T | \rho \rangle\rangle = \text{Tr} \left(\rho_T^\dagger \rho \right) \\ &= \langle\langle \rho_T | \rho_0 \rangle\rangle + \eta^2 \int_0^t ds \langle\langle \rho_T(s) | \mathcal{L}(s) | \rho_0(s) \rangle\rangle + \mathcal{O}(\eta^4). \end{aligned}$$

We define the noise sensitivity S_N ,

$$S_N = \left| \frac{\partial \mathbb{F}}{\partial (\eta^2)} \right| = \left| \int_0^t ds \langle\langle \rho_T(s) | \mathcal{L}(s) | \rho_0(s) \rangle\rangle \right|. \quad (4.71)$$

Using $\rho_0 = |\Psi_0\rangle\langle\Psi_0|$ and the explicit form of \mathcal{L} from Eq. (4.69), this expression can be simplified to

$$S_N = \frac{1}{\hbar^2} \left| \int_0^t ds \left[\text{Re} \left\{ \langle\Psi_T(s)|H_1^2(s)|\Psi_0(s)\rangle \langle\Psi_0(s)|\Psi_T(s)\rangle \right\} - |\langle\Psi_T(s)|H_1(s)|\Psi_0(s)\rangle|^2 \right] \right|. \quad (4.72)$$

Chapter 5

Improved anharmonic trap expansion through eSTA

5.1 Overview

In this chapter we generalise the derivation of eSTA and construct an alternative eSTA method that takes advantage of higher order terms. This alternative method uses higher order terms to remove an assumption used in the original eSTA formulation. We apply both the original eSTA method and the alternative method to the expansion of a Gaussian trap and accordion lattice potential. We demonstrate improved fidelity and robustness of both eSTA versions in both physical settings.

This chapter is based on the following publication:

C. Whitty, A. Kiely and A. Ruschhaupt,
*Improved anharmonic trap expansion through
enhanced shortcuts to adiabaticity*,
J. Phys. B: At. Mol. Opt. Phys. (2022).

5.2 Introduction

Fast high-fidelity control of quantum systems is a key requirement for the implementation of future quantum technologies [7]. Specifically, analytical control solutions are particularly desirable as they are simpler, provide greater physical insight and allow for additional stability requirements [79, 101]. Shortcuts to Adiabaticity (STA) are a broad class of analytical control techniques that mimic adiabatic evolution on much shorter timescales [10, 11, 72]. STA have been applied in many different contexts; engineering quantum heat engines [147–149], creating exotic angular momentum states in optical lattices [104], designing experimentally realisable fast driving of many-body spin systems [45], speed up STIRAP population transfer [9, 43, 150, 151], and to inhibit unwanted transitions in two and three level systems [96].

However, STA methods can have limitations. Some STA techniques could require non-trivial physical implementation (e.g. counterdiabatic driving), while other STA techniques may only be easily applied to small or highly symmetrical systems (e.g. Lewis-Riesenfeld invariants)[10, 11]. This difficulty motivated the development of eSTA where STA solutions can be perturbatively corrected to perform well on more complex quantum systems [132]. This method is broadly applicable, since many applications of STA techniques have already used idealised Hamiltonian descriptions e.g. single effective particles [152, 153], few-level descriptions [103, 104, 154, 155], and mean field Hamiltonians [156]. Indeed, eSTA has been applied to the transport of neutral atoms in optical conveyor belts [12, 13], and additionally has been shown to have intrinsic robustness [157].

In this work we generalise the original eSTA approach and formulate an alternative eSTA scheme. While the original eSTA scheme uses the assumption that perfect fidelity can be achieved near the starting STA scheme, the alternative eSTA scheme does not require this assumption by using higher order terms.

We show how these higher order terms can be systematically calculated using time-dependent perturbation theory.

We apply the original and alternative eSTA schemes to atomic trap expansion, using the physical settings of an optical dipole trap and an optical accordion lattice. Trap expansion of anharmonic potentials using STA has been studied [158, 159], and faster than adiabatic trap expansion has been experimentally realised using STA invariant-based engineering, in a cold atomic cloud [160], one dimensional Bose gas [74], a Fermi gas [75, 161] and loading a Bose Einstein condensate (BEC) into an optical lattice [162, 163]. The dynamic control of lattice spacing in optical accordions is another important trap expansion setting [164–166]. There have been a variety of experimental realisations of optical accordions; dynamically expanding the lattice spacing of an optical accordion loaded with ultra-cold atoms [167], expansion of a one dimensional BEC [168] and loading and compression of a two dimensional tunable Bose gas in an optical accordion [169].

This chapter is organised as follows. In Section 5.3 we introduce the generalised eSTA formalism. Then we look at trap expansion in Section 5.4 and compare STA and eSTA control schemes, considering their sensitivity to amplitude noise in both trap models.

5.3 Generalised eSTA formalism

In the following we give a generalised derivation of eSTA, complementary to the original formalism outlined in [132], which allows the formulation of an alternate eSTA scheme.

The goal of eSTA is to control a quantum system with Hamiltonian H_s . Specifically, we want to evolve the initial state $|\Psi_0\rangle$ at time $t = 0$ to the target state $|\Psi_T\rangle$ in a given total time t_f . We assume that H_s can be approximated by an existing Hamiltonian H_0 with known STA solutions, that we refer to as

the idealised STA system. In detail, we assume that there exists a parameter μ that varies continuously from μ_s to 0, such that $H_s = H_{\mu_s}$ approaches H_0 as μ approaches 0. In later examples μ will represent the anharmonicity of the experimental trapping potential, with the idealised STA system taking the form of a time-dependent harmonic oscillator. We parameterise the control scheme of H_{μ_s} by a vector $\vec{\lambda}$, which represents the deviation from the original STA control scheme ($\vec{\lambda} = \vec{0}$). Our objective is to derive a correction to the STA scheme that improves the fidelity, which we label $\vec{\lambda}_s$.

There are two main steps behind the derivation of eSTA. The first is the assumption that μ and $\|\vec{\lambda}\|$ are small such that the fidelity landscape around $(\mu = 0, \vec{\lambda} = \vec{0})$ can be well approximated to second order in μ and $\vec{\lambda}$. Secondly, we can take advantage of the known time evolution operator of the STA system to derive an improved control scheme analytically using time-dependent perturbation theory.

5.3.1 eSTA construction

Throughout the following derivation of eSTA, we assume that at the initial and target states of H_{μ_s} can be approximated by the known eigenstates of H_0 at initial and final times. We define the fidelity

$$F(\mu, \vec{\lambda}) = \left| \langle \Psi_T | U_{\mu, \vec{\lambda}}(t_f, 0) | \Psi_0 \rangle \right|^2, \quad (5.1)$$

where the time evolution is explicitly parameterised by μ and $\vec{\lambda}$ through the Hamiltonian $H_\mu(\vec{\lambda}, t)$.

For a given H_{μ_s} we derive the eSTA control vector $\vec{\lambda}_s$ by approximating several quantities that allow us to construct a parabola in $\vec{\lambda}$ for fixed $\mu = \mu_s$. This parabola projects a path of increasing fidelity, and using the eSTA formalism we calculate the $\vec{\lambda}_s$ that corresponds to the peak of this parabola. To

illustrate this construction explicitly, we let $\vec{\lambda} = \epsilon \hat{v}$ and set

$$f(\epsilon) = F(\mu_s, \epsilon \hat{v}), \quad (5.2)$$

with $\hat{v} = \nabla F(\mu_s, \vec{0}) / \|\nabla F(\mu_s, \vec{0})\|$. Throughout this chapter we follow the convention set earlier that $\nabla = \nabla_{\vec{\lambda}}$, i.e. the gradient with respect to $\vec{\lambda}$. We now approximate

$$f(\epsilon) \approx f(0) + \epsilon f'(0) + \frac{\epsilon^2}{2} f''(0), \quad (5.3)$$

with

$$\begin{aligned} f(0) &= F(\mu_s, \vec{0}), \\ f'(0) &= \|\nabla F(\mu_s, \vec{0})\|, \\ f''(0) &= \hat{v}^T \text{Hess} \left[F(\mu_s, \vec{0}) \right] \hat{v}, \end{aligned} \quad (5.4)$$

where $\text{Hess} \left[F(\mu_s, \vec{0}) \right]$ is the Hessian matrix of second order partial derivatives of F with respect to the components of $\vec{\lambda}$, and the superscript T denotes vector transposition.

In the original eSTA approach [132], the parabola is constructed using approximations to the fidelity $F(\mu_s, \vec{0})$, the gradient $\nabla F(\mu_s, \vec{0})$, together with the assumption that the optimal control vector $\vec{\lambda}_s^{(1)}$ can achieve perfect fidelity i.e. $F(\mu_s, \vec{\lambda}_s^{(1)}) = 1$. This leads to $\epsilon_s^{(1)} = 2[1 - f(0)]/f'(0)$, with

$$\vec{\lambda}_s^{(1)} = \frac{2 \left[1 - F(\mu_s, \vec{0}) \right]}{\|\nabla F(\mu_s, \vec{0})\|} \hat{v}. \quad (5.5)$$

We label this original method eSTA₁, and note that it does not use approximations to terms beyond the gradient.

Using the generalised derivation presented later in Section 5.3.2, we can

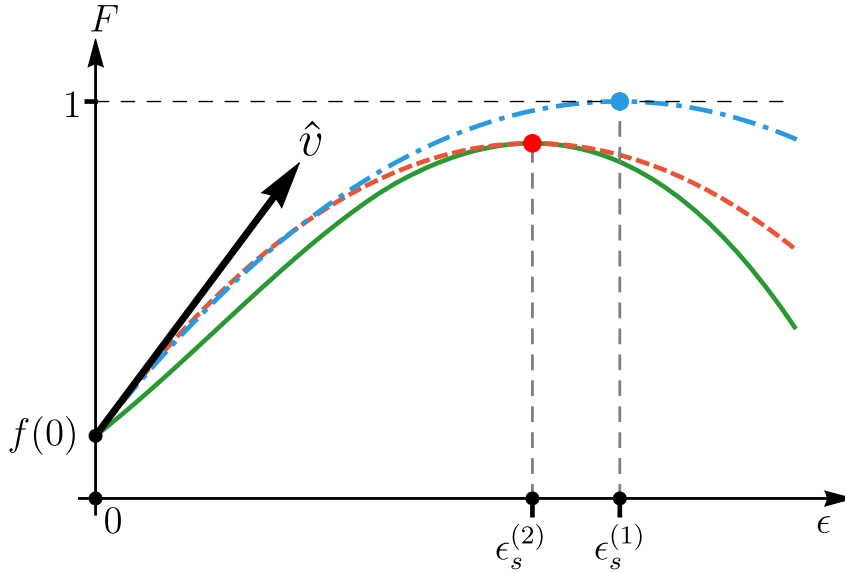


FIGURE 5.1: Diagram of eSTA construction, $F(\mu, \epsilon \hat{v})$ vs. ϵ . The true fidelity landscape (solid green), eSTA₁ parabolic approximation (dot-dashed blue) and eSTA₂ parabola (dashed red) are shown. The normalised gradient \hat{v} is represented by the solid black arrow, and $F(\mu_s, \vec{0})$ corresponds with $f(0)$. The result of applying eSTA₂ is the improved control vector $\vec{\lambda}_s^{(2)} = \epsilon_s^{(2)} \hat{v}$, which is shown matching the peak of the true fidelity landscape well.

obtain a simple approximation to the second order term $f''(0)$ in Eq. (5.4). Using this higher order term we derive an alternative eSTA scheme that we label eSTA₂. We construct this scheme by noting that the maximum of $f(\epsilon)$ will be at $\epsilon_s^{(2)} = -f'(0)/f''(0)$, and the eSTA₂ control vector now takes the form

$$\vec{\lambda}_s^{(2)} = -\frac{\nabla F(\mu_s, \vec{0})}{\hat{v}^T \text{Hess} [F(\mu_s, \vec{0})] \hat{v}}. \quad (5.6)$$

We schematically represent the parabola construction of Eq. (5.3) in Fig. 5.1. Note that eSTA₁ (dot-dashed blue line) can overshoot the desired optimal $\vec{\lambda}_s$, due to the assumption that $F = 1$ at $\vec{\lambda}_s^{(1)}$. At the expense of calculating the Hessian term in Eq. (5.4) this assumption can be removed. Note that in later examples of trap expansions we will show quantitative versions of the schematic in Fig. 5.1.

5.3.2 Perturbative approximations for eSTA control

To calculate the eSTA control vector $\vec{\lambda}_s$ for either eSTA₁ or eSTA₂, we approximate the quantities in Eq. (5.4) using the known solutions to the STA system H_0 (which can be obtained for example by using invariant-based inverse engineering [10, 11, 72]) and time-dependent perturbation theory. We label the STA solutions $\{|\chi_n(t)\rangle\}$, with $|\chi_n(t)\rangle = U_{0,\vec{0}}(t,0)|\chi_n(0)\rangle$. The time evolution operator of the STA system can be written as

$$U_{0,\vec{0}}(t,s) = \sum_{n=0}^{\infty} |\chi_n(t)\rangle\langle\chi_n(s)|. \quad (5.7)$$

The time evolution of a general H_μ can be expanded using time-dependent perturbation theory as

$$U_{\mu,\vec{\lambda}}(t,s) = U_{0,\vec{0}}(t,s) + \sum_{n=1}^{\infty} U_{\mu,\vec{\lambda}}^{(n)}(t,s), \quad (5.8)$$

where

$$U_{\mu,\vec{\lambda}}^{(n)}(t_f,0) = \left(-\frac{i}{\hbar}\right)^n \int^{(n)} U_{0,\vec{0}}(t_f,t_n) \Delta H(t_n) \dots \\ \dots U_{0,\vec{0}}(t_2,t_1) \Delta H(t_1) U_{0,\vec{0}}(t_1,0), \quad (5.9)$$

and $\Delta H_\mu(\vec{\lambda},t) = H_\mu(\vec{\lambda},t) - H_0(\vec{0},t)$, with the multi-integrals defined using the notation

$$\int^{(n)} \equiv \int_0^{t_f} dt_n \int_0^{t_n} dt_{n-1} \dots \int_0^{t_3} dt_2 \int_0^{t_2} dt_1. \quad (5.10)$$

We now set

$$\mathcal{F} = \langle\chi_0(t_f)|U_{\mu,\vec{\lambda}}(t_f,0)|\chi_0(0)\rangle = \sum_{n=0}^{\infty} \langle\chi_0(t_f)|U^{(n)}(t_f,0)|\chi_0(0)\rangle = 1 + \sum_{n=1}^{\infty} \mathcal{F}^{(n)}, \quad (5.11)$$

where we have used $\langle \chi_0(t_f) | U_{0,\bar{0}}(t_f, 0) | \chi_0(0) \rangle = 1$. Thus the fidelity becomes

$$\begin{aligned} F(\mu, \vec{\lambda}) &= \left| \mathcal{F}(\mu, \vec{\lambda}) \right|^2 = \left[1 + \sum_{n=1}^{\infty} \mathcal{F}^{(n)} \right] \left[1 + \sum_{m=1}^{\infty} (\mathcal{F}^{(m)})^* \right] \\ &= 1 + 2 \sum_{n=1}^{\infty} \text{Re} [\mathcal{F}^{(n)}] + \sum_{n=1}^{\infty} \sum_{m=1}^{\infty} \text{Re} [\mathcal{F}^{(n)} (\mathcal{F}^{(m)})^*]. \end{aligned} \quad (5.12)$$

Now we define

$$\Gamma_{n,m}(t) = \langle \chi_n(t) | \Delta H_{\mu}(\vec{\lambda}, t) | \chi_m(t) \rangle, \quad (5.13)$$

and by repeated use of Eq. (5.7) we have

$$\mathcal{F}^{(n)} = \left(\frac{-i}{\hbar} \right)^n \sum_{m_1=0}^{\infty} \cdots \sum_{m_{n-1}=0}^{\infty} \int^{(n)} \prod_{l=0}^{n-1} \Gamma_{m_{l+1}, m_l}(t_{l+1}), \quad (5.14)$$

where $m_0 = m_n = 0$ and the factors in the product commute.

The advantage of this notation is that $\mathcal{F}^{(n)}$ breaks the time interval into n nested integrals, and we can collect the integrals up to second order and obtain

$$\begin{aligned} \mathcal{F}^{(1)} &= -\frac{i}{\hbar} \int_0^{t_f} dt_1 \Gamma_{0,0}(t_1), \\ \mathcal{F}^{(2)} &= -\frac{1}{\hbar^2} \int_0^{t_f} dt_2 \int_0^{t_2} dt_1 \sum_{m=0}^{\infty} \Gamma_{0,m}(t_2) \Gamma_{m,0}(t_1). \end{aligned} \quad (5.15)$$

If we consider the fidelity up to double integrals (i.e. $n = 2$), we can write

$$\begin{aligned} F(\mu, \vec{\lambda}) &\approx 1 + \frac{1}{\hbar^2} \left| \int_0^{t_f} dt \Gamma_{0,0}(t) \right|^2 \\ &\quad - \frac{2}{\hbar^2} \int_0^{t_f} dt_2 \int_0^{t_2} \sum_{m=0}^{\infty} \text{Re} [\Gamma_{m,0}^*(t_2) \Gamma_{m,0}(t_1)], \end{aligned} \quad (5.16)$$

which can be simplified to

$$F(\mu, \vec{\lambda}) \approx 1 - \frac{1}{\hbar^2} \sum_{m=1}^{\infty} \left| \int_0^{t_f} dt \Gamma_{m,0}(t) \right|^2. \quad (5.17)$$

We derive the gradient approximation by directly taking the derivative of Eq. (5.17),

$$\begin{aligned} \frac{\partial F}{\partial \lambda_k} &\approx -\frac{1}{\hbar^2} \sum_{m=1}^{\infty} \left[\int_0^{t_f} dt \frac{\partial}{\partial \lambda_k} \Gamma_{m,0}^*(t) \int_0^{t_f} ds \Gamma_{m,0}(s) \right. \\ &\quad \left. + \int_0^{t_f} dt \Gamma_{m,0}^*(t) \int_0^{t_f} ds \frac{\partial}{\partial \lambda_k} \Gamma_{m,0}(s) \right] \\ &= -\frac{2}{\hbar^2} \sum_{m=1}^{\infty} \text{Re} \left[\int_0^{t_f} dt \frac{\partial}{\partial \lambda_k} \Gamma_{m,0}^*(t) \int_0^{t_f} ds \Gamma_{m,0}(s) \right]. \end{aligned} \quad (5.18)$$

We derive an approximation to the Hessian in the same way,

$$\begin{aligned} \frac{\partial^2 F}{\partial \lambda_l \partial \lambda_k} &\approx -\frac{2}{\hbar^2} \sum_{m=1}^{\infty} \text{Re} \left[\int_0^{t_f} dt \frac{\partial^2}{\partial \lambda_l \partial \lambda_k} \Gamma_{m,0}^*(t) \int_0^{t_f} ds \Gamma_{m,0}(s) \right. \\ &\quad \left. + \int_0^{t_f} dt \frac{\partial}{\partial \lambda_k} \Gamma_{m,0}^*(t) \int_0^{t_f} ds \frac{\partial}{\partial \lambda_l} \Gamma_{m,0}(s) \right]. \end{aligned} \quad (5.19)$$

Note that higher order terms in these approximations are obtained using Eq. (5.12) and taking appropriate derivatives. We highlight that Eq. (5.14) allows one in principle to calculate the fidelity approximation to any order n , which will improve the approximations in Eq. (5.4) that are used to construct eSTA. One could even consider higher orders beyond the second order in Eq. (5.3), but this would require calculating more terms in the fidelity expansion of Eq. (5.12) and evaluating further derivatives of Eq. (5.12).

To calculate eSTA₁ (Eq. (5.5)) and eSTA₂ (Eq. (5.6)) explicitly, we write the fidelity and gradient approximations in terms of the notation from [132],

$$F(\mu_s, \vec{0}) \approx 1 - \frac{1}{\hbar^2} \sum_{n=1}^N |G_n|^2 =: f, \quad (5.20)$$

where

$$G_n = \int_0^{t_f} dt \Gamma_{n,0}(t) \Big|_{\mu=\mu_s, \vec{\lambda}=\vec{0}}, \quad (5.21)$$

and the gradient approximation is given by

$$\nabla F(\mu_s, \vec{0}) \approx -\frac{2}{\hbar^2} \sum_{n=1}^N \operatorname{Re} \left(G_n^* \vec{K}_n \right) =: \vec{v}, \quad (5.22)$$

where the k^{th} component of \vec{K}_n given by

$$\left(\vec{K}_n \right)_k = \int_0^{t_f} dt \frac{\partial}{\partial \lambda_k} \Gamma_{n,0}(t) \Big|_{\mu=\mu_s, \vec{\lambda}=\vec{0}}, \quad (5.23)$$

and we have truncated the infinite sums to the first N terms. We define

$$(W_n)_{l,k} = \int_0^{t_f} dt \frac{\partial^2}{\partial \lambda_l \partial \lambda_k} \Gamma_{n,0}^*(t) \Big|_{\mu=\mu_s, \vec{\lambda}=\vec{0}}, \quad (5.24)$$

and the entries of the Hessian approximation in Eq. (5.6) are then given by

$$\begin{aligned} \operatorname{Hess} \left[F(\mu_s, \vec{0}) \right]_{l,k} &= \frac{\partial^2 F}{\partial \lambda_l \partial \lambda_k} \Big|_{\mu=\mu_s, \vec{\lambda}=\vec{0}} \approx \\ &- \frac{2}{\hbar^2} \sum_{n=1}^N \operatorname{Re} \left[G_n (W_n)_{l,k} - \left(\vec{K}_n^* \right)_k \left(\vec{K}_n \right)_l \right] =: \mathbb{H}_{l,k}. \end{aligned} \quad (5.25)$$

Using Eq. (5.20), Eq. (5.22) and Eq. (5.25) we can write convenient forms for the eSTA corrections, with the improved control vector using eSTA₁ (Eq. (5.5))

$$\vec{\lambda}_s^{(1)} = 2(1-f) \frac{\vec{v}}{\|\vec{v}\|^2}, \quad (5.26)$$

and for eSTA₂ (Eq. (5.6)), we have

$$\vec{\lambda}_s^{(2)} = -\frac{\vec{v} \|\vec{v}\|^2}{\vec{v}^T \mathbb{H} \vec{v}}. \quad (5.27)$$

In the next section we apply both schemes to anharmonic trap expansion and compare the results.

5.4 Anharmonic trap expansion

We now apply eSTA to anharmonic trap expansion and compare control protocols designed using STA, eSTA₁ and eSTA₂. Our goal is to transfer the ground state of the trap with initial trapping frequency ω_0 , to the ground state of the trap with final frequency ω_f with $\omega_f < \omega_0$. We consider two trapping potentials, a Gaussian trap and an accordion lattice. Since both potentials can be approximated by a harmonic trap near their minima, we can use a harmonic trap as the STA system from which we construct eSTA for the anharmonic systems.

5.4.1 Trap potentials

We define the accordion lattice potential as

$$V_L(x, t) = \text{sgn}[\omega_L(t)^2] A_L \sin^2 [k_L(t)x], \quad (5.28)$$

where we write the potential with $\text{sgn}[\omega_L(t)^2]$ so that negative $\omega_L(t)^2$ corresponds to the potential changing from confining to repulsive. For the accordion lattice the wavenumber $k_L(t) = |\omega_L(t)|/\sqrt{2A_L}$ is time dependent and the amplitude constant is $A_L = \alpha[\hbar k_L(0)]^2/2m$ with α a dimensionless constant fixing the size of the recoil energy. Negative $\omega_L(t)^2$ could be implemented physically up to a global phase factor using a simple $\pi/2$ phase shift, i.e. $-A_L \sin^2[k_L(t)x] = A_L \{\sin^2[k_L(t)(x - \pi/2)] - 1\}$.

We define also the Gaussian potential as a one-dimensional approximation to an optical dipole trap [159], given by

$$V_G(x, t) = A_G(t) [1 - \exp(-k_G x^2)]. \quad (5.29)$$

The amplitude is time dependent, with $A_G(t) = 1/4mw^2\omega_G(t)^2$, $k_G = 2\pi/\lambda_G = 2/w^2$, m is the mass, w the beam width and λ_G is the trapping laser wavelength.

Using a series expansion of either potential, we have

$$V_{0,G/L}(x,t) = \frac{1}{2}m\omega_{G/L}(t)^2x^2 + \mathcal{O}(x^4). \quad (5.30)$$

The natural choice for the STA system in the eSTA formalism for both potentials is the corresponding harmonic trap with Hamiltonian

$$H_0 = \frac{p^2}{2m} + \frac{1}{2}m\omega_{G/L}(t)^2x^2. \quad (5.31)$$

Note that as the trap depth is increased for both potentials they approach the limiting case of a harmonic trap.

5.4.2 STA system and eSTA parametrisation

The Hamiltonian for the STA system in Eq. (5.31) has a Lewis-Leach type potential with known Lewis-Riesenfeld invariant [11, 72]

$$I(t) = \frac{1}{2} \left[\frac{x^2}{b(t)^2} m\omega_0^2 + \frac{\pi(t)^2}{m} \right], \quad (5.32)$$

where $\pi = b(t)p - m\dot{b}x$ is the momentum conjugate to $x/b(t)$ and ω_0 is an arbitrary constant, chosen to be $\omega(0)$ for convenience. For $I(t)$ to be a dynamical invariant, $b(t)$ must satisfy the Ermakov equation

$$\ddot{b} + \omega(t)^2b = \frac{\omega_0^2}{b^3}. \quad (5.33)$$

We are free to choose any $b(t)$ that satisfies the appropriate boundary conditions given by $[H(t), I(t)] = 0$ at $t = 0, t_f$:

$$\begin{aligned} b(0) &= 0, & \dot{b}(0) &= 0, & \ddot{b}(0) &= 0, \\ b(t_f) &= \gamma = \sqrt{\frac{\omega_0}{\omega_f}}, & \dot{b}(t_f) &= 0, & \ddot{b}(t_f) &= 0. \end{aligned} \quad (5.34)$$

Here we use a simple polynomial ansatz for $b(t)$ from [72],

$$b(t) = 6(\gamma - 1)\xi^5 - 15(\gamma - 1)\xi^4 + 10(\gamma - 1)\xi^3 + 1, \quad (5.35)$$

where $\xi = t/t_f$. Then $\omega(t)$ can be reverse-engineered using Eq. (5.33) and we obtain [72]

$$\omega(t)^2 = \frac{\omega_0^2}{b^4} - \frac{\ddot{b}}{b}. \quad (5.36)$$

Solutions of the Schrödinger equation $i\hbar\partial/\partial t\Psi(x, t) = H_0\Psi(x, t)$ can be written as,

$$\Psi(x, t) = \sum_{n=0}^{\infty} c_n e^{i\theta_n(t)} \psi_n(x, t), \quad (5.37)$$

where $\psi_n(x, t)$ are orthonormal eigenstates of the invariant I satisfying

$$I(t)\psi_n(x, t) = \lambda_n\psi_n(x, t), \quad (5.38)$$

and c_n are constants, with the Lewis-Riesenfeld phase given by

$$\theta_n(t) = \frac{1}{\hbar} \int_0^t \langle \phi(t', n) | i\hbar \frac{\partial}{\partial t'} - H_0(t') | \phi(t', n) \rangle dt'. \quad (5.39)$$

For harmonic trap expansion, a single mode in Eq. (5.37) is given by

$$\chi_n(x, t) = e^{i\theta_n(t)} e^{i\beta_n(x, t)} \frac{\phi_n(x/b)}{b^{1/2}} \quad (5.40)$$

where

$$\begin{aligned} \theta_n(t) &= -(n + 1/2) \int_0^t dt' \frac{\omega_0}{b(t')^2}, \\ \beta_n(x, t) &= \frac{m}{2\hbar} \frac{\dot{b}}{b(t)} x^2, \end{aligned} \quad (5.41)$$

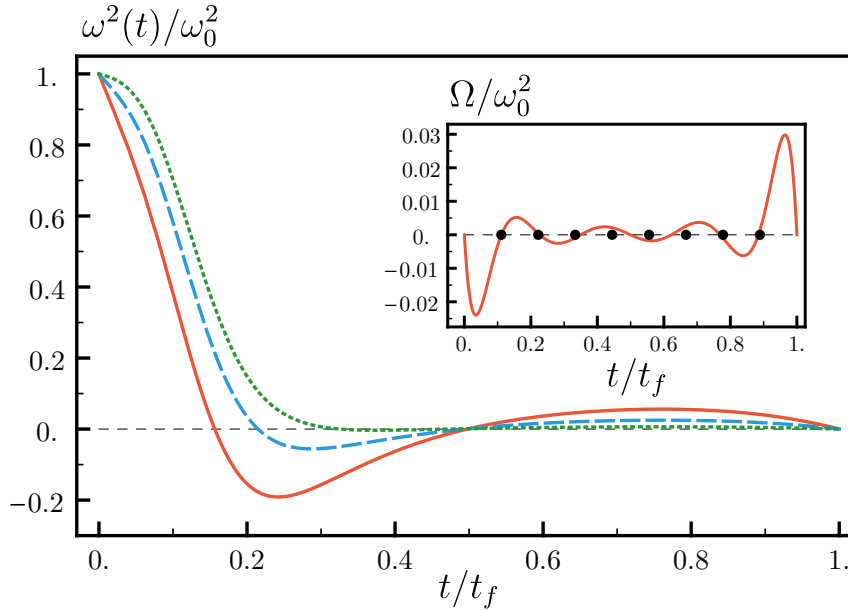


FIGURE 5.2: Examples of $\omega^2(t)/\omega_0^2$ using $\gamma = 10$, with $\omega_0 t_f = 10$ (solid-red), 15 (dashed-blue), and 30 (dotted-green). Inset: Example of Ω with $\tau_L = 26$ for fast lattice expansion using eSTA₂, with black dots indicating $M = 8$ parameterisation of Eq. (5.43).

with $\lambda_n = (n + 1/2)\hbar\omega_0$, and $\phi_n(x)$ are harmonic energy eigenstates.

In Fig. 5.2, $\omega^2(t)/\omega_0^2$ is shown for several different final times t_f . Note that even though the trap frequency can become negative, there are techniques that allow negative potentials to be implemented experimentally [72]. From Eq. (5.36) we obtain the STA solution $\omega(t)^2$ that we use as a starting point to construct the eSTA solution

$$\tilde{\omega}(t)^2 = \omega(t)^2 + \Omega(\vec{\lambda}, t), \quad (5.42)$$

where for convenience we choose the eSTA correction Ω to be a polynomial that satisfies $\Omega(\vec{\lambda}, 0) = 0$ and $\Omega(\vec{\lambda}, t_f) = 0$. We parameterise Ω by the vector $\vec{\lambda} = (\lambda_1, \dots, \lambda_M)$, where

$$\Omega\left(\vec{\lambda}, \frac{j t_f}{M+1}\right) = \lambda_j, \quad j = 1, \dots, M, \quad (5.43)$$

and M is the number of components in $\vec{\lambda}$.

Now we use eSTA to calculate the value of $\vec{\lambda}$ that improves the fidelity. In detail, we calculate $\vec{\lambda}_s^{(1)}$ using Eq. (5.26) (eSTA₁) and $\vec{\lambda}_s^{(2)}$ using Eq. (5.27) (eSTA₂). These formulae require calculating Eq. (5.21), Eq. (5.23) and Eq. (5.25).

First we calculate G_n from Eq. (5.21) using

$$G_n = \int_0^{t_f} dt \Gamma_{n,0}(t) \Big|_{\mu=\mu_s, \vec{\lambda}=\vec{0}} = \int_0^{t_f} dt \langle \chi_n(t) | \Delta H_{\mu_s}(\vec{0}, t) | \chi_0(t) \rangle, \quad (5.44)$$

where $|\chi_n(t)\rangle$ is given by Eq. (5.40) and $\Delta H_{\mu_s} = H_{\mu_s} - H_0 = V_{G/L} - V_{0,G/L}$, with H_0 from Eq. (5.31), $V_{G/L}$ from Eq. (5.29) and Eq. (5.28), and $V_{0,G/L}$ from Eq. (5.30). To calculate the k^{th} component of \vec{K}_n from Eq. (5.23), we have

$$\begin{aligned} (\vec{K}_n)_k &= \int_0^{t_f} dt \frac{\partial}{\partial \lambda_k} \Gamma_{n,0}(t) \Big|_{\mu_s, \vec{\lambda}=\vec{0}} \\ &= \int_0^{t_f} dt \langle \chi_n(t) | \frac{\partial}{\partial \lambda_k} \Delta H_{\mu_s}(\vec{\lambda}, t) \Big|_{\vec{\lambda}=\vec{0}} | \chi_0(t) \rangle \\ &= \int_0^{t_f} dt \langle \chi_n(t) | \frac{\partial}{\partial \lambda_k} V_{G/L} \Big|_{\vec{\lambda}=\vec{0}} | \chi_0(t) \rangle. \end{aligned} \quad (5.45)$$

In a similar manner we evaluate Eq. (5.25) that is required only for calculating $\vec{\lambda}_s^{(2)}$. An example of the resulting eSTA correction $\Omega(\vec{\lambda}, t)$ for fast expansion of the accordion lattice using $\vec{\lambda}_s^{(2)}$ with $M = 8$ components is shown in the inset of Fig 5.2.

5.4.3 Fidelity Results: Accordion Lattice Expansion

We first apply eSTA to the expansion of an accordion lattice with a single trapped ^{133}Cs atom in the ground state. We set the lattice parameters using values from an experimentally implemented optical lattice [76], where the initial wavenumber is $k_L(0) = 2\pi/\lambda_L$ and using Eq. (5.30) we have that $\omega_{0,L} = \omega_L(0) = 4\sqrt{\alpha}\pi^2\hbar/m\lambda_L^2$. We use numerical values $\lambda_L = 866\text{nm}$ and recoil energy

parameter $\alpha = 150$ [76]. We set the dimensionless final time $\tau_L = \omega_{0,L}t_f$ and have that $A_L/\hbar\omega_{0,L} \approx 6.12$.

We calculate the fidelity for different expansion times τ_L . In Fig. 5.3 (a) the results for STA, eSTA₁ and eSTA₂ are shown. For both $\vec{\lambda}_s^{(1)}$ and $\vec{\lambda}_s^{(2)}$ we use $M = 1$ and $M = 8$ components ($M = 1$ and $M = 8$ in Eq. (5.43) resp.). Calculating eSTA requires truncating the sums in Eq. (5.21), Eq. (5.23) and Eq. (5.24). For the results in this chapter we use the first four non-zero terms.

We find that eSTA₂ gives improvement over eSTA₁ and STA as expected. The 8 component schemes show improvement over 1 component schemes, for both eSTA₁ and eSTA₂. This demonstrates that $\vec{\lambda}_s$ with only a few components can produce significant fidelity improvement, particularly when using eSTA₂.

In the derivation of eSTA₁ it was assumed that the system could achieve maximum fidelity, i.e. $F(\mu_s, \vec{\lambda}_s^{(1)}) = 1$. The inset of Fig. 5.3 (a) demonstrates that this can lead to overshooting, which we previously illustrated schematically in Fig. 5.1; here we consider eSTA₁ and eSTA₂ with only 1 component, for $\tau_L = 25$. The true fidelity landscape (solid-green), eSTA₁ (dotted-blue) and eSTA₂ (dashed-red) fidelity approximations are shown, with the eSTA₁ scheme minimally overshooting the optimal ϵ_s . We find that $\epsilon_s^{(1)}$ from eSTA₁ is approximately $1.5 \times \epsilon_s^{(2)}$. Note that both versions of eSTA would agree if the fidelity for both $\vec{\lambda}_s^{(1)}$ and $\vec{\lambda}_s^{(2)}$ was exactly 1. We note that calculating eSTA₁ may be simpler than calculating eSTA₂ in certain settings, and that the utility of either eSTA approach will depend on the given system dynamics.

5.4.4 Fidelity Results: Gaussian Trap Expansion

We consider Gaussian trap expansion and use similar values to the Gaussian approximation of a single trapped ⁸⁷Rb atom in an optical dipole trap in [158, 159], with inverse unit of time $\omega_{0,G} = 2\pi \times 2500\text{Hz}$, $A_G/\hbar\omega_{0,G} \approx 2418$, laser

wavelength $\lambda_{\text{laser}} = 1060\text{nm}$, a beam waist of $20\lambda_{\text{laser}}$ and set the expansion time $\tau_G = \omega_{0,G}t_f$.

We simulate Gaussian trap expansion for different expansion times τ_G and the results are shown in Fig. 5.3 (b), using the STA scheme (solid-green line), eSTA₁ (dotted and solid blue lines) and eSTA₂ (dashed and solid red lines).

As with the optical accordion, we consider eSTA₁ and eSTA₂ with two parameterisations of $\vec{\lambda}_s^{(1)}$ and $\vec{\lambda}_s^{(2)}$, a 1 component scheme (dotted-blue, dashed-red) and an 8 component scheme (solid blue, solid red). We find that eSTA₁ and eSTA₂ are an improvement over STA, and that the 1 and 8 component schemes produce very similar results for both eSTA₁ and eSTA₂. This is an indication that the polynomial form of $\Omega(\vec{\lambda}, t)$ allows a large class of improved schemes. The inset of Fig. 5.3 (b) demonstrates again that the original eSTA scheme can minimally overshoot the optimal ϵ_s (compare again to Fig. 5.1), with the parabola calculated using eSTA₂ matching the true fidelity well.

5.4.5 ESTA Sensitivity

In this section we consider errors in the trapping potentials and calculate the sensitivity to these errors using the STA, eSTA₁ and eSTA₂ schemes introduced earlier. For the lattice potential we consider an error in the amplitude

$$V_{\text{err}}^L(x, t) = \text{sgn}[\omega_L(t)^2] A_L(1 + \delta) \sin^2 [k_L(t)x], \quad (5.46)$$

and for the Gaussian potential we also consider an amplitude error, given by

$$V_{\text{err}}^G(x, t) = A_G(1 + \delta) \{1 - \exp^2 [-k_G(t)x^2]\}. \quad (5.47)$$

We define the error sensitivity by

$$S := \left| \frac{\partial F}{\partial \delta} \Big|_{\delta=0} \right|, \quad (5.48)$$

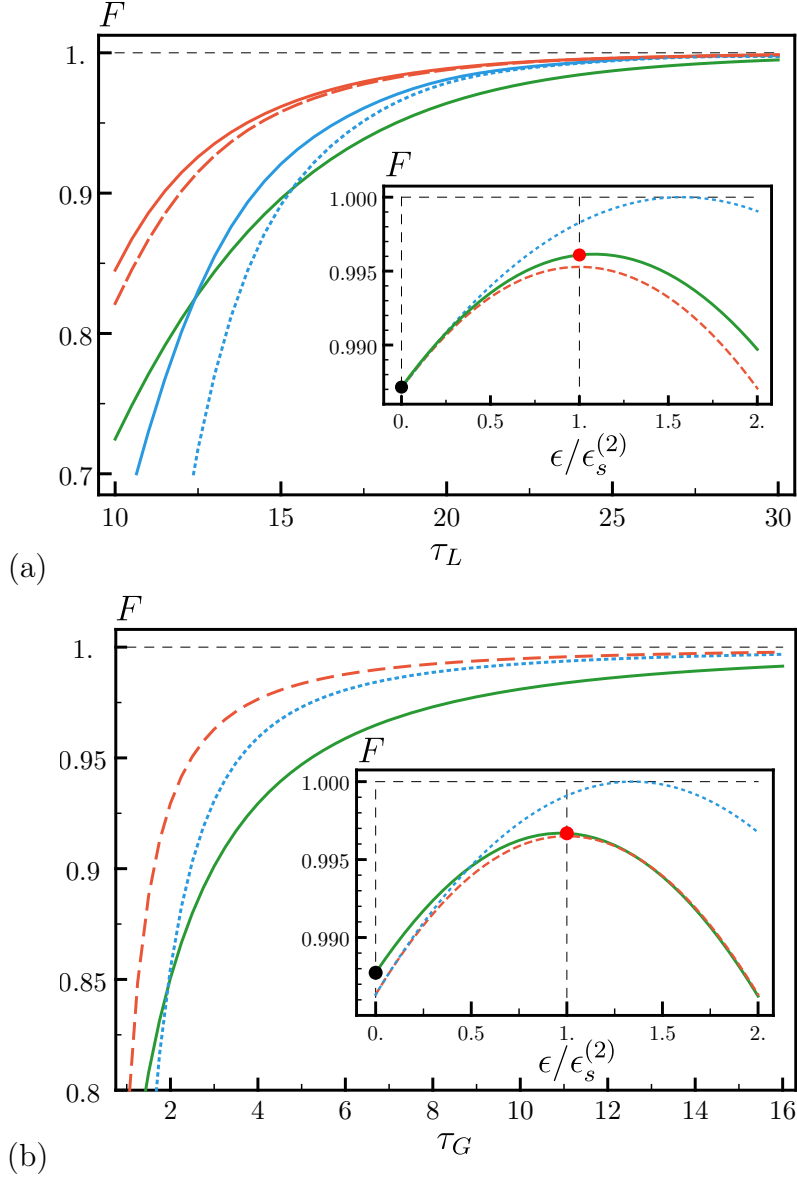


FIGURE 5.3: Fidelity vs. expansion time $\tau_{L/G}$. (a) Lattice expansion; STA (solid green), eSTA₁ with $M = 8$ components (solid blue) and $M = 1$ (dotted blue), eSTA₂ $M = 8$ (solid red) and $M = 1$ (dashed red). Lattice parameters as in Section 5.4.3 for this plot and the inset. Inset: Fidelity vs $\epsilon/\epsilon_s^{(2)}$ for lattice expansion with $\tau_L = 25$; true fidelity landscape (solid green), eSTA₁ (dotted blue) and eSTA₂ (dashed red) parabola approximations. (b) Gaussian trap expansion; same labeling as (a), with $M = 1$ and $M = 8$ results indistinguishable (solid lines omitted). Physical values given in Section 5.4.4. Inset: Same labeling as (a) with $\tau_G = 13$.

and calculate this quantity numerically using a multi-point discrete approximation to the derivative. Note that a lower sensitivity S means a given scheme is

more robust against error.

Heuristically we expect that eSTA will simultaneously improve fidelity and robustness: for $\mu = 0$ both eSTA and STA give fidelity 1, and as μ increases the eSTA fidelity is always higher than the STA fidelity, i.e. the slope of the eSTA fidelity is expected to be smaller than the slope of the STA scheme. Assuming that this slope is approximately proportional to the error sensitivity S , we also expect lower error sensitivity for eSTA than STA.

In the following we look at the numerical error sensitivity. In Fig 5.4 (a) the sensitivity of lattice expansion is shown, with STA (dot-dashed green), eSTA₁ ($M = 1$ dotted-blue, $M = 8$ solid blue) and eSTA₂ ($M = 1$ dashed-red, $M = 8$ solid red). Each line is marked at the point where $F \geq 0.95$, with eSTA₁ and eSTA₂ still achieving this fidelity for lower τ_L than STA. In this high fidelity regime, both eSTA schemes are generally less sensitive (smaller S) to error than the STA scheme for $\tau_L \gtrsim 15$, in agreement with the heuristic argument from above. The eSTA₂ scheme generally gives the highest fidelities and lowest sensitivities, as shown in Fig. 5.3 (a) and Fig. 5.4 (a). Interestingly, the single component ($M = 1$) eSTA₂ scheme (dashed-red line) has lower sensitivity than the 8 component ($M = 8$) eSTA₂ scheme (solid-red line).

For Gaussian trap expansion, see Fig. 5.4 (b), there is negligible difference in sensitivity between choosing a single or 8 component scheme, for either eSTA₁ or eSTA₂. Again, the points for which $F \geq 0.95$ is first achieved are marked on each line. For these high fidelities eSTA₁ and eSTA₂ outperform STA, in agreement with the heuristic argument outlined earlier. In this case eSTA₂ has generally the highest fidelity, as shown in Fig. 5.3 (b), as well as the lowest sensitivity in Fig. 5.4 (b). A convenient eSTA scheme can be chosen depending on the required fidelity or sensitivity.

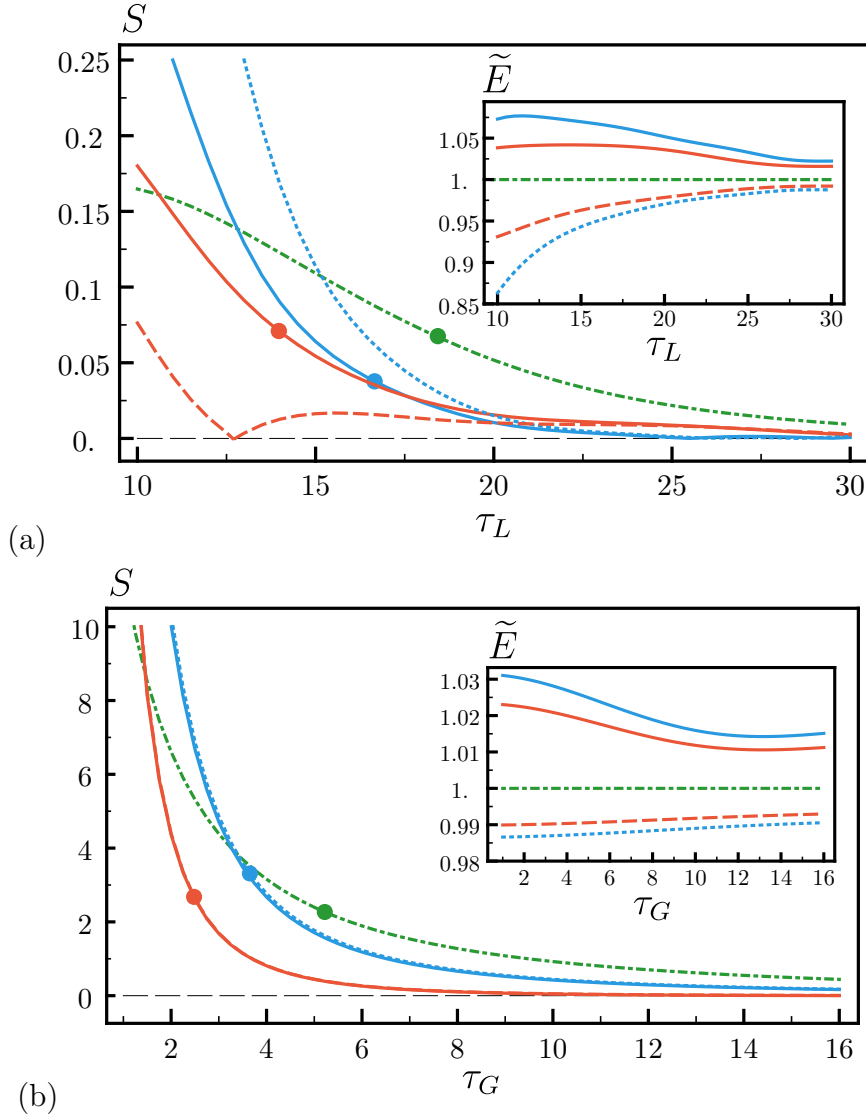


FIGURE 5.4: Trap expansion sensitivity $S = |\partial F/\partial \delta|$ vs. $\tau_{L/G}$. Same parameters and labeling as Fig 5.3. (a) Lattice expansion, with first τ_L for which $F > 0.95$ marked on each line. Inset: Time averaged energy (Eq. (5.49)) of the eSTA schemes scaled by the STA scheme (dot-dashed green), \tilde{E} vs. τ_L . (b) Gaussian trap expansion sensitivity S vs. τ_G , again with first τ_G for which $F > 0.95$ shown.

We also consider the time averaged energy

$$E(\vec{\lambda}) = \frac{1}{t_f} \int_0^{t_f} dt \langle H_{\mu_s}(\vec{\lambda}, t) \rangle, \quad (5.49)$$

and define $\tilde{E} = E(\vec{\lambda})/E(\vec{0})$ such that the different eSTA protocols are in direct comparison with the STA scheme. The insets in Fig. 5.3 (a) and (b) show \tilde{E}

for eSTA₁ and eSTA₂. The values of \tilde{E} of the eSTA schemes are close to 1 (i.e. close to the STA scheme), demonstrating that little additional time averaged energy is required for improvement. In both lattice and Gaussian expansion, the 1 component STA schemes have a lower time averaged energy than STA ($\tilde{E} < 1$), while using more components ($M = 8$) has a higher value ($\tilde{E} > 1$).

5.5 Conclusion

The main result in this chapter is a generalisation of the original eSTA derivation in [132], and the construction of an alternative eSTA scheme. This alternative eSTA scheme allows the removal of an assumption of the original eSTA method, at the expense of calculating an additional Hessian term. Both eSTA schemes are applied to anharmonic trap expansion, resulting in higher fidelity and improved robustness.

Generally, there are several important advantages that the eSTA formalism has to offer; the derivation is analytic, applicable to a wide variety of quantum control problems and the control schemes are expected to have enhanced robustness against noise. In addition, eSTA can offer insight into a given control problem, for example by first considering low dimension parameterisations of the control scheme. There is also significant freedom in choosing how to parameterise the control scheme for either approach; for example, we can choose to preserve the symmetry of the original STA scheme, or use a form of the eSTA improvement that lends itself to certain conditions e.g. a Fourier sum with fixed bandwidth. Analytic eSTA control schemes that are outside the class of STA solutions can be derived, and they could give improved starting points for numerical optimisation. As an outlook, higher order eSTA schemes can be constructed using the formalism presented in this chapter which would be useful if some lower order terms vanish.

Chapter 6

Lattice transport of two Coulomb-interacting ions via eSTA

6.1 Introduction

The physical platform of trapped ions manipulated with coherent light is one of the most promising quantum computing architectures [170]. A critical component of trapped ion quantum computers is shuttling of ions between regions of memory storage and computation [66]. In particular, shuttling of single atom and atomic clouds using STA have been studied extensively [133]. Fast transport of two Coulomb-interacting ions using invariant-based inverse engineering has also been considered in [124], and single atom fast transport in anharmonic traps using reverse engineering has been studied in [171]. In this chapter we use eSTA to design control schemes for transporting two Coulomb-interacting ions in a lattice potential, in contrast to the Gaussian potential used in Section 3.6. We consider amplitude noise in the lattice and show that the quantum derived eSTA scheme even works for the equivalent classical system.

6.2 System Hamiltonian

Our goal is to transport the groundstate of a lattice potential with two equal-mass Coulomb-interacting ions. The time-dependent Schrödinger equation in the lab frame is given by

$$-i\hbar \frac{\partial}{\partial t} \psi(q_1, q_2, t) = \mathcal{H}(t) \psi(q_1, q_2, t), \quad (6.1)$$

with Hamiltonian

$$\mathcal{H}(t) = \frac{p_1^2}{2m} + \frac{p_2^2}{2m} + V[q_1 - Q(t), q_2 - Q(t)] + \frac{C}{|q_1 - q_2|}, \quad (6.2)$$

where q_j are the position operators of each ion, $p_j = -i\hbar \frac{\partial}{\partial q_j}$ ($j = 1, 2$) are the corresponding momentum operators, and $Q(t)$ is the trajectory of the potential minimum. The Coulomb constant is given by $C = e^2/(4\pi\epsilon_0)$ where e is the electron charge, and ϵ_0 is the dielectric vacuum permittivity constant. The potential is given by

$$V(q_1, q_2, t) = a \sin^2 \left\{ m\omega_0^2 q_1 / \sqrt{2a} \right\} + a \sin^2 \left\{ m\omega_0^2 q_2 / \sqrt{2a} \right\}. \quad (6.3)$$

It is convenient to transform Eq. (6.1) to dimensionless units. To achieve this, we define a unit of length $L = \sqrt{\hbar/m\omega_0}$ and unit of time ω_0^{-1} , giving dimensionless spatial coordinates $\tilde{q}_j = q_j/L$ and time $\tilde{t} = \omega_0 t$. The corresponding unit of energy is $\hbar\omega_0$, with the dimensionless trap depth parameter given by $\tilde{a} = a/\hbar\omega_0$. The dimensionless trap trajectory is $\tilde{Q}(\tilde{t}) = Q(\omega_0 t)/L$ and the dimensionless Coulomb constant is $\tilde{C} = C\sqrt{m/\omega_0\hbar^3}$. For notational convenience we now drop the tilde notation and the dimensionless Hamiltonian in the lab frame is given by

$$H = \frac{p_1^2}{2} + \frac{p_2^2}{2} + a \sin^2 \left\{ \frac{[q_1 - Q(t)]}{\sqrt{2a}} \right\} + a \sin^2 \left\{ \frac{[q_2 - Q(t)]}{\sqrt{2a}} \right\} + \frac{C}{q_1 - q_2}. \quad (6.4)$$

Note that for practical values of masses, trap depths and transport times considering here, there is no overlap of the two ion's wavefunctions and we can treat the particles as distinguishable and assume $q_1 > q_2$.

We now transform Eq. (6.4) to a center of mass (c) and relative (r) motion frame, defined by

$$\begin{aligned} x_c &= \frac{1}{2}(q_1 + q_2), & x_r &= \frac{1}{2}(q_1 - q_2), \\ p_c &= p_1 + p_2, & p_r &= p_1 - p_2. \end{aligned} \quad (6.5)$$

The lattice Hamiltonian of Eq. (6.4) then becomes

$$H_{c,r} = \frac{p_c^2}{4} + \frac{p_r^2}{4} + a \sin^2 \left[\frac{x_c - Q(t) + x_r}{\sqrt{2a}} \right] + a \sin^2 \left[\frac{x_c - Q(t) - x_r}{\sqrt{2a}} \right] + \frac{C}{2x_r}. \quad (6.6)$$

Our goal is to transport the groundstate of Eq. (6.6) a distance d in a given transport time t_f , by designing the appropriate transport function $Q(t)$.

6.3 Approximate STA Hamiltonian

To calculate eSTA we must first approximate the lattice Hamiltonian Eq. (6.6) by a Hamiltonian for which a STA scheme $q_0(t)$ can be derived using invariant-based inverse engineering. Our ultimate goal will be to design $Q(t) = q_0(t) + \Delta Q(t)$, where $\Delta Q(t)$ is the calculated eSTA correction that improves the lattice transport in Hamiltonian Eq. (6.6). However, first we derive a STA transport function $q_0(t)$ for the approximated Hamiltonian.

In this particular example we can directly consider a second-order Taylor series of Eq. (6.6) by setting $Q(t) = q_0(t)$, and expanding the series in $x_c - q_0(t)$

and x_r given by

$$H_{c,r} \approx \frac{p_c^2}{4} + \frac{p_r^2}{4} + [x_c - q_0(t)]^2 + x_r^2 + \frac{C}{2x_r}. \quad (6.7)$$

Note that this is equivalent to considering a harmonic approximation in the lab frame given by

$$H_{0,\text{lab}}(t) = \frac{p_1^2}{2} + \frac{p_2^2}{2} + \frac{1}{2} [q_1 - q_0(t)]^2 + \frac{1}{2} [q_2 - q_0(t)]^2 + \frac{C}{q_1 - q_2}, \quad (6.8)$$

and performing the same coordinate transformation steps from Eq. (6.6), which again gives Eq. (6.7). We now set $H_0(t) = H_{0,c}(t) + H_{0,r}$, with

$$H_{0,c}(t) = \frac{p_c^2}{4} + [x_c - q_0(t)]^2, \quad (6.9)$$

$$H_{0,r} = \frac{p_r^2}{4} + x_r^2 + \frac{C}{2x_r}. \quad (6.10)$$

The key point here is that the transport motion only affects the x_c coordinate, hence we can simplify the problem of designing the trap trajectory $q_0(t)$ for two particles, to designing $q_0(t)$ for an effective single particle transport in the center-of-mass coordinate.

We now apply invariant-based engineering in the same manner as in Section 2.2.3. For completeness we consider a separable invariant $I(t) = I_c(t) \otimes I_r$ of Eq. (6.7), which must satisfy the invariant condition now given by

$$\left(\frac{\partial}{\partial t} I_c - \frac{i}{\hbar} [H_{0,c}, I_c] \right) \otimes I_r + I_c \otimes \left(\frac{\partial}{\partial t} I_r - \frac{i}{\hbar} [H_{0,r}, I_r] \right) = 0. \quad (6.11)$$

For simplicity we can choose $I_r = H_{0,r}$ since $H_{0,r}$ is time independent. Then the instantaneous eigenstates of I_r are simply the energy eigenstates of $H_{0,r}$, which we assume are discrete and non-degenerate and denote by $\chi_{r,n}(x_r)$. For the center-of-mass component we can use the single particle harmonic transport

invariant from Section 2.2.3, which in the dimensionless quantities used here is

$$I_c(t) = \frac{1}{4}(p_c - 2\dot{q}_c)^2 + (x_c - q_c)^2, \quad (6.12)$$

where the tap trajectory $q_0(t)$ is given by the auxiliary equation (see Section 2.2.3), given by

$$q_0(t) = \ddot{q}_c(t) + q_c(t). \quad (6.13)$$

The instantaneous eigenstates of $I_c(t)$ are given by

$$\chi_{c,n}(x_c, t) = e^{2i\dot{q}_c x_c} \phi_n(x_c - q_c), \quad (6.14)$$

where $\phi_n(x)$ are solutions to the stationary Schrödinger equation with the center-of-mass Hamiltonian Eq. (6.9) at $t = 0$ (i.e. stationary harmonic eigenstates). We can now write the instantaneous eigenstates of $I(t) = I_c(t) \otimes I_r$ as

$$\Phi_{n,n'}(x_c, x_r, t) = \chi_{c,n}(x_c, t) \chi_{r,n'}(x_r), \quad (6.15)$$

from which we can construct solutions to the Schrödinger equation Eq. (6.6), given by

$$\Psi_{n,n'}(x_c, x_r, t) = \Phi_{n,n'}(x_c, x_r, t) e^{i\alpha_n(t)} e^{i\gamma_{n'}(t)}, \quad (6.16)$$

where $\gamma_{n'}(t) = -E_{n'}t$ is the associated dynamical phase of $\chi_{r,n'}(x_r)$ and $E_{n'}$ the energy eigenvalue of $\chi_{r,n'}(x_r)$. The Lewis-Riesenfeld phase $\alpha_n(t)$ associated with $\chi_{c,n}(x_c, t)$ is given by

$$\alpha_n(t) = -i(n + 1/2)t + \int_0^t \dot{q}_c^2 dt'. \quad (6.17)$$

Following Section 2.2.3, we now apply invariant-based inverse engineering to Eq. (6.9). We assume the ions are at rest at their equilibrium distance at $t = 0$, so that the initial state is a groundstate of Eq. (6.7). As discussed in Section 2.2.3, by considering the commutator $[H_0(t), I(t)] = 0$ at $t = 0, t_f$, we obtain boundary conditions on $q_c(t)$ given by

$$q_c(0) = 0, \quad q_c(t_f) = d, \quad \dot{q}_{c0}(t') = 0, \quad \ddot{q}_{c0}(t') = 0, \quad (6.18)$$

for $t' = 0, t_f$. We further impose $q_c^{(3)}(t') = q_c^{(4)}(t') = 0$ for $t' = 0, t_f$, so that $\dot{q}_0(t') = \ddot{q}_0(t') = 0$. Once we choose a $q_c(t)$ satisfying the boundary conditions in Eq. (6.18), we can inverse engineer $q_0(t)$ from the auxiliary equation Eq. (6.13). We again choose a polynomial ansatz for $q_c(t)$ as in Section 2.2.3,

$$q_c(t) = ds^5 (70s^4 - 315s^3 + 540s^2 - 420s + 126), \quad (6.19)$$

where $s = t/t_f$.

In summary, by choosing $q_c(t)$ given in Eq. (6.19), we obtain the trap trajectory $q_0(t)$ from Eq. (6.13), that will transport the ground state of Eq. (6.7) a distance d in a given transport time t_f , with fidelity 1.

6.4 Calculation of eSTA correction

We now calculate the eSTA trap trajectory $Q(t) = q_0(t) + \Delta Q(t)$ in Eq. (6.6), where $q_0(t)$ is the initial STA scheme from Eq. (6.13). We choose the eSTA correction $Q(t)$ to be a polynomial of degree $M + 1$, which we parameterise by a vector $\vec{\lambda} = (\lambda_1, \dots, \lambda_M)$ with $\Delta Q(0) = 0$ and $\Delta Q(t_f) = 0$, and

$$\Delta Q \left(\frac{k t_f}{M + 1} \right) = \lambda_k, \quad k = 1, \dots, M, \quad (6.20)$$

where M is the number of components in $\vec{\lambda}$ which we choose to be $M = 6$ here. An example of $\Delta Q(t)$ is shown in the inset of Fig. 6.1.

We use the original formulation of eSTA from Section 2.2.3, where the eSTA control vector $\vec{\lambda}$ is then given by

$$\vec{\lambda}_s = -\frac{\left(\sum_{n=1}^N |G_n|^2\right) \left[\sum_{n=1}^N \operatorname{Re}\left(G_n^* \vec{K}_n\right)\right]}{\left|\sum_{n=1}^N \operatorname{Re}\left(G_n^* \vec{K}_n\right)\right|^2}, \quad (6.21)$$

with

$$G_{n,n'} = \int_0^{t_f} dt \langle \Psi_{n,n'}(t) | \left[H_{\text{com,rel}}(\vec{\lambda} = \vec{0}; t) - H_0(t) \right] | \Psi_{0,0}(t) \rangle, \quad (6.22)$$

and

$$\vec{K}_{n,n'} = \int_0^{t_f} dt \langle \Psi_{n,n'}(t) | \nabla_{\vec{\lambda}} H_{\text{com,rel}}(\vec{\lambda} = \vec{0}; t) | \Psi_{0,0}(t) \rangle, \quad (6.23)$$

where the states $|\Psi_{n,n'}(t)\rangle$ are given by Eq. (6.16).

To calculate $G_{n,n'}$, we first simplify the integral using $x_c \mapsto x_c + q_0$, set $\beta(t) = q_0 - q_c$ giving

$$\begin{aligned} G_{n,n'} = & \int_0^{t_f} dt e^{i(\alpha_0 - \alpha_n)t} e^{i(\gamma_0 - \gamma_{n'})t} \int_{-\infty}^{\infty} dx_r \int_{-\infty}^{\infty} dx_c \chi_{c,n}(x_c, t)^* \chi_{r,n'}(x_r)^* \times \\ & \left\{ a \sin^2 \left[\frac{x_c + \beta(t) + x_r}{\sqrt{2a}} \right] + a \sin^2 \left[\frac{x_c + \beta(t) - x_r}{\sqrt{2a}} \right] - [x_c + \beta(t)]^2 - x_r^2 \right\} \times \\ & \chi_{c,0}(x_c, t) \chi_{r,0}(x_r), \end{aligned} \quad (6.24)$$

where $\chi_{c,n}(x_c, t)$ are from Eq. (6.14) and $\chi_{r,n'}(x_r)$ are energy eigenstates of $H_{0,r}$. We now make the approximation that the relative motion remains in the relative groundstate $\chi_{r,0}(x_r)$ during transport, and that $\chi_{r,0}(x_r)$ is strongly peaked about $x_r \approx l/2$, where l is the equilibrium distance of the ions. Hence

we can approximate $G_{n,n'} \approx G_{n,0}$ and set $G_n = G_{n,0}$ given by

$$G_n = a \int_0^{t_f} dt e^{int} \int_{-\infty}^{\infty} dx_c \phi_n(x_c) \phi_0(x_c) \times \left\{ \sin^2 \left[\frac{x_c + \beta(t) + l/2}{\sqrt{2a}} \right] + \sin^2 \left[\frac{x_c + \beta(t) - l/2}{\sqrt{2a}} \right] - [x_c + \beta(t)]^2 - \left(\frac{l}{2} \right)^2 \right\}. \quad (6.25)$$

where $\phi_n(t)$ are given in Eq. (6.14). The integral in the x_c coordinate can be done analytically and then only the time integral needs to be evaluated numerically. In a similar manner, we can also simplify the $\vec{K}_{n,n'}$ integrals, where the m^{th} component of $\vec{K}_n := \vec{K}_{n,0}$ is given by

$$(K_n)_m = \sqrt{\frac{a}{2}} \int_0^{t_f} dt e^{int} \left. \frac{\partial}{\partial \lambda_m} \right|_{\vec{\lambda}=\vec{0}} Q(t) \int_{-\infty}^{\infty} dx_c \phi_n(x_c) \phi_0(x_c) \times \left\{ \sin^2 \left[\sqrt{\frac{2}{a}} (x_c + \beta + l/2) \right] + \sin^2 \left[\sqrt{\frac{2}{a}} (x_c + \beta - l/2) \right] \right\}. \quad (6.26)$$

Again, the integral over x_c can be done analytically and only the time integral needs to be evaluated numerically.

In Fig. 6.1 the fidelity is shown for both the STA trap trajectory $q_0(t)$ (dashed blue), and the eSTA trap trajectory $Q(t) = q_0(t) + \Delta Q(t)$ (solid orange). We find significant improvement in the transport fidelity using eSTA in comparison with STA, particularly for fast transport times ($\tau = \omega_0 t_f < 16$). For longer transport both schemes give very high fidelities.

6.5 Robustness of eSTA to systematic errors

We now consider a systematic amplitude error given by the potential

$$V^A = a(1 + \delta) \sin^2 \left[\frac{x_c + x_r + l/2}{\sqrt{2a}} \right] + a(1 + \delta) \sin^2 \left[\frac{x_c - x_r - l/2}{\sqrt{2a}} \right], \quad (6.27)$$

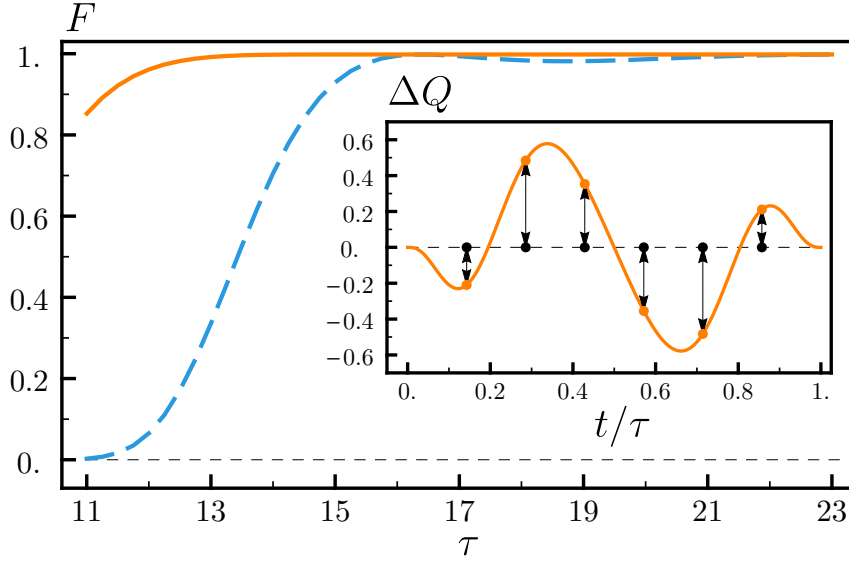


FIGURE 6.1: Fidelity vs transport time $\tau = \omega_0 t_f$, for lattice transport of two Coulomb-interacting ions with $\omega_0 = 4\pi \times 10^4 \text{Hz}$, $\tilde{a} = 10^7$, and $\tilde{C} = 7.35 \times 10^7$ and a transport distance of $\tilde{d} = 1562$; STA $q_0(t)$ (dashed-blue), eSTA $Q(t)$ (solid-orange). Inset: Example of eSTA correction $\Delta Q(t)$ for $\tau = 10$. Black arrows indicate the 6 components of $\vec{\lambda}$ at $t_f/7$ intervals.

where δ is the strength of the amplitude error. In a similar manner to Section 4.6, we evaluate the sensitivity

$$S = \left| \frac{\partial F}{\partial \delta} \Big|_{\delta=0} \right|, \quad (6.28)$$

for both the STA and eSTA schemes. The sensitivity measures the response of the system to a systematic error δ in the potential. A large value of S indicates that a given control scheme is sensitive to perturbations in the potential parameter $a(1 + \delta)$, while a smaller value of S indicates robustness against such perturbations. In Fig. 6.2 the sensitivity is evaluated for different transport times τ for both the STA (dashed blue) and eSTA (solid orange) schemes.

Starting from $\tau \approx 11.8$, we find eSTA gives significant improvement over STA as demonstrated by the much lower values of S that the eSTA scheme produces. The eSTA scheme also has the useful property that the sensitivity is very low for the range of transport times shown with $\tau > 13$. This robustness

against perturbations across a range of protocol times, makes eSTA particularly useful in an experimental setting.

We now compare Fig. 6.2 with the corresponding fidelity plot Fig. 6.1. It can be seen that for $\tau \geq 11.5$ the eSTA scheme gives both improved fidelity and sensitivity over the STA scheme. For $\tau < 11.5$, the situation is less clear since the STA scheme gives a lower sensitivity than the eSTA scheme, however the fidelity is also smaller as shown in Fig. 6.1. As discussed in Section 4.6.2, this motivates the definition of a systematic error bound that takes into account both the fidelity and the sensitivity.

We define the exact systematic error bound \mathcal{B}_E as the largest value of $|\delta|$ for which $F(\delta) > F_R$, where F_R is a chosen reference fidelity. To calculate \mathcal{B}_E , one would need to numerically evaluate $F(\delta)$ until $F < F_R$. This is a computationally expensive task, and so we consider a linear approximation $\mathcal{B} \approx \mathcal{B}_E$. Assuming a linear dependence of F on δ , we consider

$$S = \left| \frac{\partial F}{\partial \delta} \Big|_{\delta=0} \right| \approx \frac{|F(\delta=0) - F(\delta)|}{|\delta|}, \quad (6.29)$$

which can be written

$$|\delta| \approx \frac{|F(\delta=0) - F(\delta)|}{S} \leq \frac{|F(\delta=0) - F_R|}{S}. \quad (6.30)$$

This motivates the definition

$$\mathcal{B} = \begin{cases} \frac{F(\delta=0) - F_R}{S} & : F(\delta=0) > F_R \\ 0 & : F(\delta=0) \leq F_R \end{cases}, \quad (6.31)$$

giving a measure that naturally incorporates both the fidelity and an approximation of the sensitivity for a given control scheme. For a given transport time, the approximate systemic error bound \mathcal{B} gives the largest the magnitude of the error δ can be, such that the fidelity is greater than F_R .

A large value of \mathcal{B} means that a large range of $\delta < |\delta|$ achieves the reference fidelity, while a smaller value of \mathcal{B} indicates that only a narrow range of $\delta < |\delta|$ meet the minimum fidelity requirement. Essentially this means that higher values of \mathcal{B} indicate that a given control scheme has high fidelity and low sensitivity. This is in contrast to evaluating a control scheme using the sensitivity alone, where a smaller value of the sensitivity indicates good performance but tells us nothing about the fidelity value. Note that the approximation in Eq. (6.30) requires that δ is small, and if a given scheme is very stable S can become arbitrarily small leading to very large unphysical values of \mathcal{B} . Hence, for very stable stable schemes \mathcal{B} may take values much larger than the true range of δ that achieves fidelities above F_R .

The inset of Fig. 6.2 shows \mathcal{B} with $F_R = 0.95$ plotted on a Log scale versus transport time $\tau = \omega_0 t_f$, with eSTA (solid orange) giving significant improvement over STA (dashed blue) for all transport times. Note that the values of \mathcal{B} become very large for the eSTA scheme from $\tau = 13$, which can be understood immediately from the very low sensitivity eSTA has in comparison with STA as shown in Fig. 6.1.

One limitation of the approximation $\mathcal{B} \approx \mathcal{B}_E$ is that for schemes with a very small sensitivity S , the value of \mathcal{B} can become very large. Since Eq. (6.30) assumes a small value of δ , control schemes with very low sensitivity cause \mathcal{B} to diverge, and give unphysical values for the range of δ that give fidelities above the reference fidelity of F_R . While \mathcal{B}_E can be numerically calculated, it requires considerable computational cost. To overcome this limitation of \mathcal{B} , we now introduce an alternative measure η_Q that also incorporates the fidelity and sensitivity of a given control scheme $Q(t)$. We define this measure by

$$\eta_Q = \sqrt{c_1 (1 - F)^2 + c_2 (S)^2}, \quad (6.32)$$

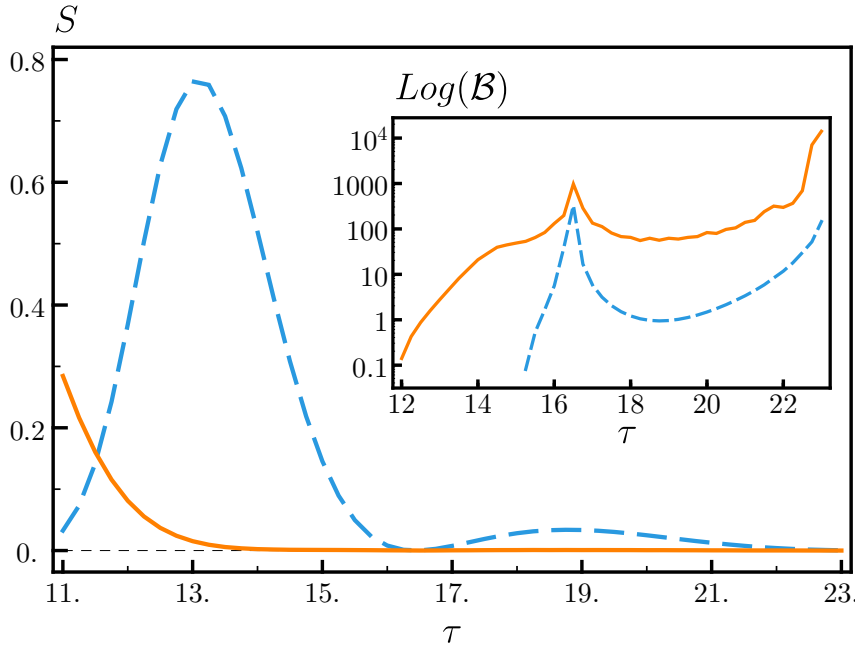


FIGURE 6.2: Sensitivity S versus transport time $\tau = \omega_0 t_f$; STA (dashed-blue), eSTA (solid-orange). Inset: Error bound \mathcal{B} with log scale versus τ ; STA (dashed-blue), eSTA (solid-orange). Same parameters as in Fig 6.1.

where $1 - F$ is the infidelity of a given transport scheme $Q(t)$, S is the corresponding sensitivity and c_1 and c_2 are chosen constant weights. We use the infidelity and sensitivity since they are both quantities that we wish to minimise, making Eq. (6.32) a natural measure of deviation from perfect control with fidelity $F = 1$ and sensitivity $S = 0$. For $c_1 = 1$ and $c_2 = 0$ we recover the infidelity (infidelity version of Fig. 6.1), and for $c_1 = 0$ and $c_2 = 1$ we recover the sensitivity (Fig. 6.2). The further η_Q is away from zero, the higher the infidelity and sensitivity. In Fig. 6.3 η_Q is shown using $c_1 = 1$ and $c_2 = 1$ for the transport times considered, where we can immediately see that the STA scheme breaks down quickly for $\tau < 16$. We have seen this previously from Fig. 6.2 and Fig. 6.1, but the advantage here is that a single quantity can be used to identify high fidelity and low sensitivity schemes. Note that the constants c_1 and c_2 can be chosen to ensure that $1 - F$ and S are evaluated on a useful scale for a given problem.

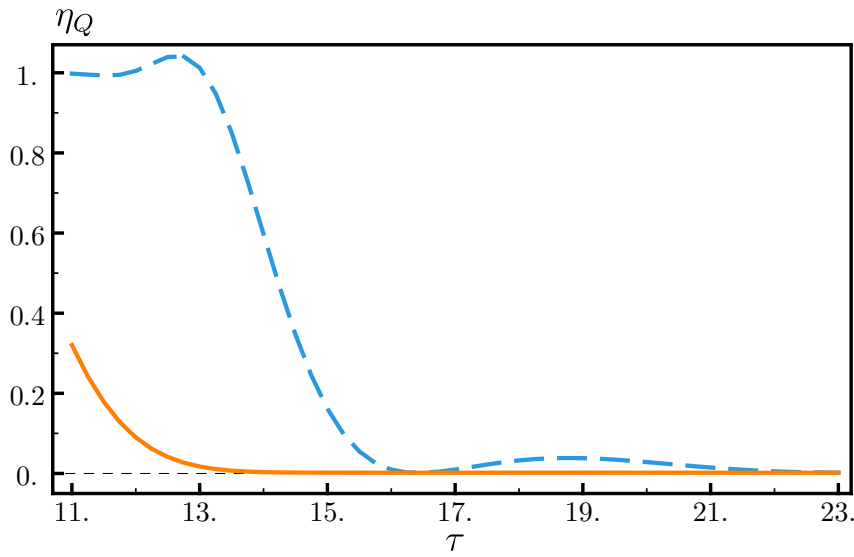


FIGURE 6.3: Plot of η_Q versus transport time τ , STA (dashed-blue) and eSTA (solid orange).

6.6 Classical comparison

For transport of two equal masses in a one dimensional trap, it is known that if there is minimal motional squeezing of the wavepacket during transport then the dynamics of the corresponding classical system agree very well with the dynamics of the quantum system [66]. We now investigate if eSTA transport trajectory calculated for the quantum system also improves the corresponding classical system. In Fig. 6.4 we use $\vec{\lambda}$ calculated for the quantum system with the classical system (solid orange), and both schemes overlap almost exactly for the physical parameters considered.

Note that an alternative method to optimise $Q(t)$ (but a computationally more expensive strategy than applying eSTA), is to first numerically optimise the corresponding classical system and then implement the resulting protocols on the quantum system. To optimise $\vec{\lambda}$ in the classical setting, we calculate the gradient with respect to the classical energy excitation and perform a simple line search in the direction of the gradient to find the first fidelity maximum.

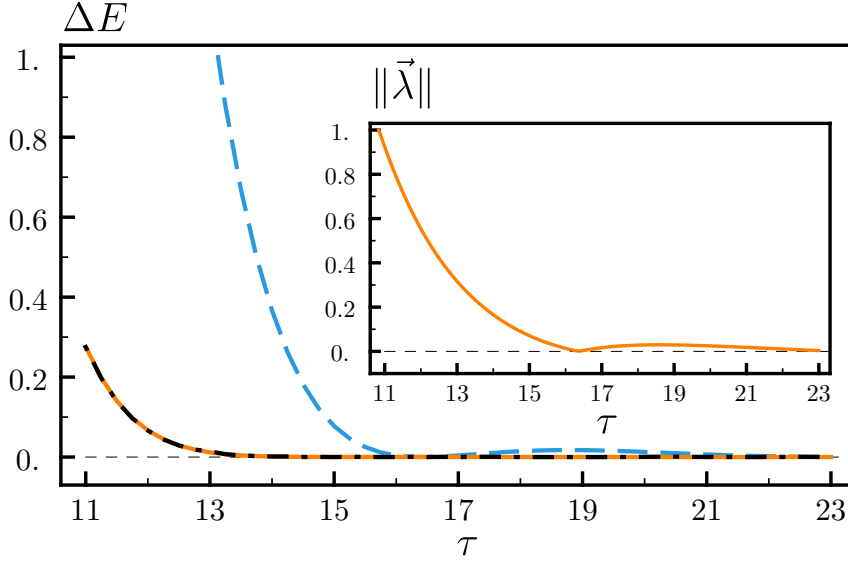


FIGURE 6.4: Classical lattice transport of two ions including Coulomb interaction with same parameters as Fig 6.1 STA (dashed-blue), eSTA (solid-orange) and numerically optimised (dot-dashed black). Inset: Norm of $\vec{\lambda}$ calculated using eSTA (solid orange) and norm of $\vec{\lambda}$ calculated numerically (dashed black).

The classical energy excitation is just the Hamiltonian, with

$$E(\vec{\lambda}, t_f) = \mathcal{H} \left[q_0(t_f) + \Delta Q(\vec{\lambda}, t_f) \right]. \quad (6.33)$$

We approximate the gradient by

$$\nabla E(\vec{0}, t_f) \approx \frac{1}{\delta} \left[E(\vec{\lambda}, t_f) - E(\vec{0}, t_f) \right], \quad (6.34)$$

where we choose δ by halving an initial guess until the numerical derivative is unchanged in the sixth significant figure. The line search was extended beyond the first maximum to investigate the fidelity landscape, and for these parameters only a single maximum was found for each t_f during this search. In Fig. 6.4 the classical excitation of system is shown for the STA (dashed blue) numerically calculated gradient search (dot-dashed black).

The inset of Fig. 6.4 shows the norms of $\vec{\lambda}$, for the numerical gradient search

case (dashed black) and eSTA for the quantum system (solid orange), with the norms being very similar for the physical parameters considered here.

6.7 Conclusion

In this Chapter we have used eSTA to construct improved lattice transport schemes. We have shown that eSTA produces control schemes with both high fidelity and strong robustness against systematic amplitude noise. The systematic error bound \mathcal{B} from Chapter 4 was discussed and evaluated, and a further performance measure η_Q was introduced. Finally, the eSTA scheme was shown to also give good results for the corresponding classical Hamiltonian.

Chapter 7

Summary and Outlook

In this thesis we have introduced the eSTA formalism and applied it to a number of quantum systems to achieve fast and robust quantum control schemes. We now summarise the main topics of the preceding chapters and give an outlook on possible avenues of future research.

7.1 Summary

In this section the previous chapters are summarised, concluding with an overview of the key properties of eSTA.

Enhanced Shortcuts to Adiabaticity: In Chapter 3 we presented an analytic technique to extend STA quantum control methods to problems beyond their current scope. The eSTA formalism uses STA solutions for a known system, together with time-dependent perturbation theory, to construct solutions to problems that do not have STA solutions. We demonstrated the effectiveness of eSTA using several examples, relevant to many current quantum technologies. We first considered a system with finite dimension, namely population inversion without the rotating wave approximation. Using an STA scheme already optimised for systematic errors in the Rabi frequency, an eSTA scheme was constructed that gave improved fidelity. We then applied eSTA to the transport of a neutral atom in a Gaussian potential, and found improved fidelity for a range of trap depths. Finally we used eSTA to design improved schemes for the

transport of two Coulomb interacting ions in a Gaussian trap, and again showed the improvement offered by eSTA for a range of trap depths.

Robustness of enhanced Shortcuts to Adiabaticity: By examining the robustness of the eSTA control schemes, in Chapter 4 we found that eSTA protocols can result in higher fidelity and improved robustness against several types of systematic and noise errors. We demonstrated these improvements using the practical setting of atom transport in an optical lattice potential, near a quantum speed limit [76].

We provided a general heuristic argument that the eSTA schemes should result in higher fidelities and improved stability compared with the original STA schemes. We also provided strong numerical evidence of this claim, by considering noise and systematic errors in the lattice potential. We quantified the increase in robustness by defining new measures beyond the standard sensitivity measure, such as an eSTA-specific evaluation tool C_Q that allows possible control functions to be evaluated without full numerical treatment, and a practical error bound \mathcal{B} that combines fidelity and sensitivity such that eSTA and STA control functions can be compared quantitatively.

Improved anharmonic trap expansion through eSTA: The main result of Chapter 5 was a generalisation of the original eSTA derivation in Chapter 3, that naturally leads to an alternative eSTA method. This alternative eSTA method allows the removal of an assumption of the original eSTA method, at the expense of calculating an additional Hessian term. Both eSTA methods were applied to two examples of one-particle anharmonic trap expansion, expansion of a Gaussian trap and expansion of a lattice potential. The resulting eSTA schemes resulted in both higher fidelity and improved robustness against systematic amplitude error, over the corresponding STA schemes.

Lattice transport of two ions via eSTA: In Chapter 6 we applied eSTA to transport of two Coulomb-interacting ions in a lattice potential. We first derived an approximate STA Hamiltonian from which we could calculate the

eSTA scheme. We found that eSTA resulted in much higher fidelities than the STA scheme and that the eSTA scheme had much improved robustness against systematic lattice amplitude error than the corresponding STA scheme.

Summary of eSTA properties: We now present a general summary of eSTA, where we highlight several advantages that make the eSTA formalism a useful tool for quantum control. The derivation of eSTA is analytic, meaning that the resulting control schemes can offer physical insight into a given control problem and that they can be chosen to satisfy any necessary experimental constraints. It is expected that eSTA control schemes will have enhanced robustness against noise, which is a critically important attribute in practical experimental settings. There is significant freedom in choosing how to parameterise the eSTA control scheme, allowing the design of experimentally feasible schemes (such as those with a fixed bandwidth or with certain symmetries). There are many future possible applications of eSTA, since many systems can be approximated by systems with existing STA solutions but do not have STA solutions themselves. We now explore some of these future possible applications of eSTA.

7.2 Outlook

In this outlook we will consider possible future applications of eSTA.

Counterdiabatic driving: Counterdiabatic driving has a natural extension using eSTA, since the instantaneous eigenstates from the counterdiabatic scheme can be used to construct eSTA. We start with a system with a Hamiltonian $H = H_0 + \mu H_1$, where H_0 is a system that has a counterdiabatic scheme such that $H_0 + H_{CD}$ achieves the required state transfer and μ is a parameter that we assume to be small. Then we can construct an improved control scheme for H using the known states from $H_{CD} = i\hbar \sum_n (\langle \partial_t \phi_n | \phi_n \rangle - \langle \phi_n | \partial_t \phi_n \rangle \langle \phi_n |)$. Counterdiabatic driving has been applied in many settings, from faster STIRAP

to control of many body systems. Hence there are many opportunities to use counterdiabatic driving as a starting point and then apply the eSTA formalism.

Open quantum systems: Another area where eSTA can have applications is open quantum systems. For example, suppose an open quantum system has the Lindblad form $\frac{\partial}{\partial t}\rho(t) = [\mathcal{L}_0(t) + \mu\mathcal{L}_1(t)]\rho(t)$ where $\mathcal{L}_0 = -\frac{i}{\hbar}[H_0, \rho(t)]$. If there exist an STA technique for \mathcal{L}_0 and we are able to write the time evolution operator in terms of known solutions, then we can use eSTA to construct improved control schemes for $\mathcal{L}_0(t) + \mu\mathcal{L}_1(t)$. Note that in this setting the maximal attainable fidelity may be less than one for a given \mathcal{L}_1 , due to dissipation. Thus in this setting, the alternative approach using the Hessian approximation discussed in Chapter 5 will be a more appropriate eSTA method to use in an open system context.

Numerical optimisation: Finding optimal control schemes numerically can be computationally expensive, and it is often advantageous to initialise the problem with a control scheme that is close to an optimal scheme. This allows faster convergence to an optimal scheme and one can use knowledge of the approximately optimal scheme to streamline the optimisation process. For example, if the approximate optimal scheme has a certain symmetry, it may be possible to reduce the number of control parameters by assuming the optimal scheme will also have this symmetry. While STA can be used as a starting point for such optimisation, eSTA may offer a competitive advantage. While eSTA will have generally a higher fidelity, crucially we also expect eSTA to have increased robustness (as discussed in Chapter 4). This improved robustness can be a major advantage for practical implementation of control schemes.

Many body quantum systems: Designing control schemes for many body quantum systems is an area of active research, in particular for state preparation and implementing quantum neural networks and machine learning. STA have been used to design control schemes in many-body systems, for example spin chain systems such as the Ising model [172], the LMG model [46] and the

Heisenberg spin chain [153]. Using STA to control many body systems can require approximations to be made, and in principle there is scope for eSTA to improve existing STA state preparation schemes. Inverse engineering and FAQUAD have been used to speed up quantum perceptrons in an Ising model [173]. It would be interesting to see if eSTA could provide a way to speed up and improve robustness in designing quantum perceptrons.

Classical systems: STA have been applied to classical systems [33, 34, 174], and using classical time-dependent perturbation theory there is scope to apply eSTA to a variety of classical systems. Again, the key advantage eSTA can offer is improved fidelity and robustness without a large computational cost. Note that when there is correspondence between a classical and quantum system, one could calculate eSTA in either setting and use the resulting control scheme on either system. For example, in Chapter 6 we calculated eSTA in the quantum system and showed that the resulting eSTA scheme worked very well on the corresponding classical system. This approach could be very useful when calculating eSTA in one setting is significantly easier than in the other setting. Another interesting possibility would be to calculate eSTA for a many body quantum system by using a semi-classical or classical approximation to the full quantum system.

Given the broad applicability of STA methods, we expect that there will be many applications of eSTA in the future, across a wide variety of quantum systems.

Bibliography

- [1] J. P. Dowling and G. J. Milburn, *Philos. Trans. Royal Soc. A* **361**, 1655 (2003).
- [2] D. Dong, C. Wu, C. Chen, B. Qi, I. R. Petersen, and F. Nori, *Sci. Rep.* **6**, 36090 (2016).
- [3] C. L. Degen, F. Reinhard, and P. Cappellaro, *Rev. Mod. Phys.* **89**, 035002 (2017).
- [4] J. Werschnik and E. K. U. Gross, *J. Phys. B: At. Mol. Opt. Phys.* **40**, R175 (2007).
- [5] N. Khaneja, T. Reiss, C. Kehlet, T. Schulte-Herbrüggen, and S. J. Glaser, *J. Magn. Reson.* **172**, 296 (2005).
- [6] S. van Frank, A. Negretti, T. Berrada, R. Bücker, S. Montangero, J.-F. Schaff, T. Schumm, T. Calarco, and J. Schmiedmayer, *Nat Commun* **5**, 4009 (2014).
- [7] S. J. Glaser, U. Boscain, T. Calarco, C. P. Koch, W. Köckenberger, R. Kosloff, I. Kuprov, B. Luy, S. Schirmer, T. Schulte-Herbrüggen, D. Sugny, and F. K. Wilhelm, *Eur. Phys. J. D* **69**, 279 (2015).
- [8] J. Preskill, *Quantum* **2**, 79 (2018).
- [9] N. V. Vitanov, A. A. Rangelov, B. W. Shore, and K. Bergmann, *Rev. Mod. Phys.* **89**, 015006 (2017).

-
- [10] E. Torrontegui, S. Ibáñez, S. Martínez-Garaot, M. Modugno, A. del Campo, D. Guéry-Odelin, A. Ruschhaupt, X. Chen, and J. G. Muga, in *Advances In Atomic, Molecular, and Optical Physics*, Vol. 62, edited by E. Arimondo, P. R. Berman, and C. C. Lin, Advances in Atomic, Molecular, and Optical Physics (Academic Press, Jan. 2013), pp. 117–169.
- [11] D. Guéry-Odelin, A. Ruschhaupt, A. Kiely, E. Torrontegui, S. Martínez-Garaot, and J. G. Muga, *Rev. Mod. Phys.* **91**, 045001 (2019).
- [12] S. H. Hauck, G. Alber, and V. M. Stojanović, *Phys. Rev. A* **104**, 053110 (2021).
- [13] S. H. Hauck and V. M. Stojanović, *Phys. Rev. Applied* **18**, 014016 (2022).
- [14] Laidler, Keith J., *Can. J. Chem.* **72**, 936 (1994).
- [15] C. Kittel and H. Kroemer, *Thermal physics* (W. H. Freeman, 1980).
- [16] M. Born and V. Fock, *Z. Physik* **51**, 165 (1928).
- [17] T. Kato, *J. Phys. Soc. Jpn.* **5**, 435 (1950).
- [18] J. E. Avron and A. Elgart, *Comm. Math. Phys.* **203**, 445 (1999).
- [19] M. V. Berry, *Philos. Trans. Royal Soc. A* **392**, 45 (1984).
- [20] B. Simon, *Phys. Rev. Lett.* **51**, 2167 (1983).
- [21] M. S. Sarandy and D. A. Lidar, *Phys. Rev. A* **71**, 012331 (2005).
- [22] A. Galindo and P. Pascual, *Quantum mechanics II*, Theoretical and Mathematical Physics (Springer Berlin Heidelberg, 1991).
- [23] A. Messiah, *Quantum mechanics* (Dover Publications, New York, USA, 2014).
- [24] D. Comparat, *Phys. Rev. A* **80**, 012106 (2009).
- [25] J.-F. Schaff, P. Capuzzi, G. Labeyrie, and P. Vignolo, *New J. Phys.* **13**, 113017 (2011).

-
- [26] M. Demirplak and S. A. Rice, *J. Chem. Phys.* **129**, 154111 (2008).
- [27] M. V. Berry, *J. Phys. A: Math. Theor.* **42**, 365303 (2009).
- [28] B. Bransden and C. Joachain, *Quantum mechanics* (Prentice Hall, 2000).
- [29] S. Deffner, *New J. Phys.* **18**, 012001 (2015).
- [30] T. Sägesser, R. Matt, R. Oswald, and J. P. Home, *New J. Phys.* **22**, 073069 (2020).
- [31] X. Chen, R.-L. Jiang, J. Li, Y. Ban, and E. Y. Sherman, *Phys. Rev. A* **97**, 013631 (2018).
- [32] J. Li, K. Sun, and X. Chen, *Sci Rep* **6**, 38258 (2016).
- [33] S. González-Resines, D. Guéry-Odelin, A. Tobalina, I. Lizuain, E. Torrontegui, and J. G. Muga, *Phys. Rev. Applied* **8**, 054008 (2017).
- [34] A. Patra and C. Jarzynski, *New J. Phys.* **19**, 125009 (2017).
- [35] X.-J. Lu, J. G. Muga, X. Chen, U. G. Poschinger, F. Schmidt-Kaler, and A. Ruschhaupt, *Phys. Rev. A* **89**, 063414 (2014).
- [36] X.-J. Lu, M. Palmero, A. Ruschhaupt, X. Chen, and J. G. Muga, *Phys. Scr.* **90**, 074038 (2015).
- [37] A. Levy, A. Kiely, J. G. Muga, R. Kosloff, and E. Torrontegui, *New J. Phys.* **20**, 025006 (2018).
- [38] P. Kaufmann, T. F. Gloger, D. Kaufmann, M. Johanning, and C. Wunderlich, *Phys. Rev. Lett.* **120**, 010501 (2018).
- [39] T. Ruster, C. Warschburger, H. Kaufmann, C. T. Schmiegelow, A. Walther, M. Hettrich, A. Pfister, V. Kaushal, F. Schmidt-Kaler, and U. G. Poschinger, *Phys. Rev. A* **90**, 033410 (2014).
- [40] G. Ness, C. Shkedrov, Y. Florshaim, and Y. Sagi, *New J. Phys.* **20**, 095002 (2018).

-
- [41] Y.-X. Du, Z.-T. Liang, Y.-C. Li, X.-X. Yue, Q.-X. Lv, W. Huang, X. Chen, H. Yan, and S.-L. Zhu, *Nat. Comm.* **7**, 12479 (2016).
- [42] J.-F. Schaff, X.-L. Song, P. Capuzzi, P. Vignolo, and G. Labeyrie, en, *EPL* **93**, 23001 (2011).
- [43] M. Demirplak and S. A. Rice, *J. Phys. Chem. A* **107**, 9937 (2003).
- [44] J. G. Muga, X. Chen, S. Ibáñez, I. Lizuain, and A. Ruschhaupt, *J. Phys. B: At. Mol. Opt. Phys.* **43**, 085509 (2010).
- [45] H. Saberi, T. Opatrný, K. Mølmer, and A. del Campo, *Phys. Rev. A* **90**, 060301 (2014).
- [46] S. Campbell, G. De Chiara, M. Paternostro, G. M. Palma, and R. Fazio, *Phys. Rev. Lett.* **114**, 177206 (2015).
- [47] G. Vacanti, R. Fazio, S. Montangero, G. M. Palma, M. Paternostro, and V. Vedral, *New J. Phys.* **16**, 053017 (2014).
- [48] S. Ibáñez, X. Chen, E. Torrontegui, J. G. Muga, and A. Ruschhaupt, *Phys. Rev. Lett.* **109**, 100403 (2012).
- [49] D. Sels and A. Polkovnikov, en, *Proc. Natl. Acad. Sci.* **114**, E3909 (2017).
- [50] P. W. Claeys, M. Pandey, D. Sels, and A. Polkovnikov, *Phys. Rev. Lett.* **123**, 090602 (2019).
- [51] G. Passarelli, R. Fazio, and P. Lucignano, *Phys. Rev. A* **105**, 022618 (2022).
- [52] Z. Yin, C. Li, J. Allcock, Y. Zheng, X. Gu, M. Dai, S. Zhang, and S. An, *Nat. Commun.* **13**, 188 (2022).
- [53] S. Iram, E. Dolson, J. Chiel, J. Pelesko, N. Krishnan, Ö. Güngör, B. Kuznets-Speck, S. Deffner, E. Ilker, J. G. Scott, and M. Hinczewski, *Nat. Phys.* **17**, 135 (2021).
- [54] S. Deffner, C. Jarzynski, and A. del Campo, *Phys. Rev. X* **4**, 021013 (2014).

-
- [55] S. Masuda and K. Nakamura, *Philos. Trans. Royal Soc. A* **466**, 1135 (2010).
- [56] E. Torrontegui, S. Martínez-Garaot, A. Ruschhaupt, and J. G. Muga, *Phys. Rev. A* **86**, 013601 (2012).
- [57] S. Martínez-Garaot, M. Palmero, J. G. Muga, and D. Guéry-Odelin, *Phys. Rev. A* **94**, 063418 (2016).
- [58] A. Patra and C. Jarzynski, *Phys. Rev. Research* **3**, 013087 (2021).
- [59] H. R. Lewis and P. G. L. Leach, *J. Math. Phys.* **23**, 2371 (1982).
- [60] H. R. Lewis and W. B. Riesenfeld, *J. Math. Phys.* **10**, 1458 (1969).
- [61] J. L. Reid, *J. Phys. A: Math. Gen.* **15**, 2751 (1982).
- [62] E. Torrontegui, X. Chen, M. Modugno, S. Schmidt, A. Ruschhaupt, and J. G. Muga, *New J. Phys.* **14**, 013031 (2012).
- [63] B. Khantoul, A. Bounames, and M. Maamache, *Eur. Phys. J. Plus* **132**, 258 (2017).
- [64] Ermakov, V. P., *Universita Izvestia Kiev, Series III* **9**, 1 (1880).
- [65] V. P. Ermakov, *Appl. Anal. Discrete Math* **2**, 123 (2008).
- [66] H. A. Fürst, M. H. Goerz, U. G. Poschinger, M. Murphy, S. Montangero, T. Calarco, F. Schmidt-Kaler, K. Singer, and C. P. Koch, *New J. Phys.* **16**, 075007 (2014).
- [67] C. Monroe, D. M. Meekhof, B. E. King, W. M. Itano, and D. J. Wineland, *Phys. Rev. Lett.* **75**, 4714 (1995).
- [68] D. J. Wineland, M. Barrett, J. Britton, J. Chiaverini, B. DeMarco, W. M. Itano, B. Jelenković, C. Langer, D. Leibfried, V. Meyer, T. Rosenband, and T. Schätz, *Philos. Trans. Royal Soc. A* **361**, 1349 (2003).
- [69] R Blatt and D. Wineland, *Nature* **453**, 1008 (2008).

-
- [70] R. Reichle, D. Leibfried, R. B. Blakestad, J. Britton, J. D. Jost, E. Knill, C. Langer, R. Ozeri, S. Seidelin, and D. J. Wineland, *Fortschritte der Phys.* **54**, 666 (2006).
- [71] W. K. Hensinger, *Nature* **592**, 190 (2021).
- [72] X. Chen, A. Ruschhaupt, S. Schmidt, A. del Campo, D. Guéry-Odelin, and J. G. Muga, *Phys. Rev. Lett.* **104**, 063002 (2010).
- [73] S. Bize, P. Laurent, M. Abgrall, H. Marion, I. Maksimovic, L. Cacciapuoti, J. Grünert, C. Vian, F. P. dos Santos, P. Rosenbusch, P. Lemonde, G. Santarelli, P. Wolf, A. Clairon, A. Luiten, M. Tobar, and C. Salomon, *J. Phys. B: At. Mol. Opt. Phys.* **38**, S449 (2005).
- [74] W. Rohringer, D. Fischer, F. Steiner, I. E. Mazets, J. Schmiedmayer, and M. Trupke, *Sci. Rep.* **5**, 9820 (2015).
- [75] S. Deng, P. Diao, Q. Yu, A. del Campo, and H. Wu, *Phys. Rev. A* **97**, 013628 (2018).
- [76] N. Peter, T. Groh, W. Alt, C. Robens, D. Meschede, A. Negretti, S. Montangero, T. Calarco, A. Alberti, and M. R. Lam, *Phys. Rev. X* **11**, 011035 (2021).
- [77] E. Torrontegui, S. Ibáñez, X. Chen, A. Ruschhaupt, D. Guéry-Odelin, and J. G. Muga, *Phys. Rev. A* **83**, 013415 (2011).
- [78] X. Chen, E. Torrontegui, D. Stefanatos, J.-S. Li, and J. G. Muga, *Phys. Rev. A* **84**, 043415 (2011).
- [79] A. Ruschhaupt, X. Chen, D. Alonso, and J. G. Muga, *New J. Phys.* **14**, 093040 (2012).
- [80] W. Press, *Numerical recipes in c: the art of scientific computing* (Cambridge University Press, Cambridge Cambridgeshire New York, 1992).
- [81] C. Cohen-Tannoudji, B. Diu, and F. Laloë, *Quantum mechanics, volume 1: Basic concepts, tools, and applications* (Wiley, 2019).

-
- [82] M. Suzuki, *Proc. Jpn. Acad. B* **69**, 161 (1993).
- [83] A. M. Childs, Y. Su, M. C. Tran, N. Wiebe, and S. Zhu, *Phys. Rev. X* **11**, 011020 (2021).
- [84] R. Karplus and J. Schwinger, *Phys. Rev.* **73**, 1020 (1948).
- [85] R. P. Feynman, *Phys. Rev.* **84**, 108 (1951).
- [86] R. F. Snider, *J. Math. Phys.* **5**, 1580 (1964).
- [87] R. M. Wilcox, *J. Math. Phys.* **8**, 962 (1967).
- [88] M. Suzuki, *J. Math. Phys.* **26**, 601 (1985).
- [89] W. P. Schleich et al., *Appl. Phys. B* **122**, 130 (2016).
- [90] B. T. Torosov, E. S. Kyoseva, and N. V. Vitanov, *Phys. Rev. A* **92**, 033406 (2015).
- [91] S. S. Ivanov and N. V. Vitanov, *Phys. Rev. A* **92**, 022333 (2015).
- [92] B. T. Torosov and N. V. Vitanov, *Phys. Rev. A* **90**, 012341 (2014).
- [93] S. van Frank, M. Bonneau, J. Schmiedmayer, S. Hild, C. Gross, M. Cheneau, I. Bloch, T. Pichler, A. Negretti, T. Calarco, and S. Montangero, *Sci. Rep.* **6**, 1 (2016).
- [94] P. Doria, T. Calarco, and S. Montangero, *Phys. Rev. Lett.* **106**, 190501 (2011).
- [95] A. Ruschhaupt and J. G. Muga, *J. Mod. Opt.* **61**, 828 (2014).
- [96] A. Kiely and A. Ruschhaupt, *J. Phys. B: At. Mol. Opt. Phys.* **47**, 115501 (2014).
- [97] F. Impens and D. Guéry-Odelin, *Sci. Rep.* **9**, 1 (2019).
- [98] R. Corgier, S. Amri, W. Herr, H. Ahlers, J. Rudolph, D. Guéry-Odelin, E. M. Rasel, E. Charron, and N. Gaaloul, *New J. Phys.* **20**, 055002 (2018).
- [99] H. L. Mortensen, J. J. W. H. Sørensen, K. Mølmer, and J. F. Sherson, *New J. Phys.* **20**, 025009 (2018).

-
- [100] S. Martínez-Garaot, A. Ruschhaupt, J. Gillet, T. Busch, and J. G. Muga, *Phys. Rev. A* **92**, 043406 (2015).
- [101] A. Kiely, J. P. L. McGuinness, J. G. Muga, and A. Ruschhaupt, *J. Phys. B: At. Mol. Opt. Phys.* **48**, 075503 (2015).
- [102] X. Chen and J. G. Muga, *Phys. Rev. A* **86**, 033405 (2012).
- [103] A. Benseny, A. Kiely, Y. Zhang, T. Busch, and A. Ruschhaupt, *EPJ Quantum Technol.* **4**, 1 (2017).
- [104] A. Kiely, A. Benseny, T. Busch, and A. Ruschhaupt, *J. Phys. B: At. Mol. Opt. Phys.* **49**, 215003 (2016).
- [105] S. An, D. Lv, A. del Campo, and K. Kim, *Nat. Commun.* **7**, 1 (2016).
- [106] T. Wang, Z. Zhang, L. Xiang, Z. Jia, P. Duan, W. Cai, Z. Gong, Z. Zong, M. Wu, J. Wu, L. Sun, Y. Yin, and G. Guo, *New J. Phys.* **20**, 065003 (2018).
- [107] T. Wang, Z. Zhang, L. Xiang, Z. Jia, P. Duan, Z. Zong, Z. Sun, Z. Dong, J. Wu, Y. Yin, and G. Guo, *Phys. Rev. Applied* **11**, 034030 (2019).
- [108] J. Zhang, J. H. Shim, I. Niemeyer, T. Taniguchi, T. Teraji, H. Abe, S. Onoda, T. Yamamoto, T. Ohshima, J. Isoya, and D. Suter, *Phys. Rev. Lett.* **110**, 240501 (2013).
- [109] J. Kölbl, A. Barfuss, M. S. Kasperczyk, L. Thiel, A. A. Clerk, H. Ribeiro, and P. Maletinsky, *Phys. Rev. Lett.* **122**, 090502 (2019).
- [110] S. Longhi, *Laser Photonics Rev.* **3**, 243 (2009).
- [111] T.-Y. Lin, F.-C. Hsiao, Y.-W. Jhang, C. Hu, and S.-Y. Tseng, *Opt. Express* **20**, 24085 (2012).
- [112] H.-C. Chung, K.-S. Lee, and S.-Y. Tseng, *Opt. Express* **25**, 13626 (2017).
- [113] J. Deng, Q.-h. Wang, Z. Liu, P. Hänggi, and J. Gong, *Phys. Rev. E* **88**, 062122 (2013).

-
- [114] D. Guéry-Odelin, J. G. Muga, M. J. Ruiz-Montero, and E. Trizac, *Phys. Rev. Lett.* **112**, 180602 (2014).
- [115] J. Scheuer, X. Kong, R. S. Said, J. Chen, A. Kurz, L. Marseglia, J. Du, P. R. Hemmer, S. Montangero, T. Calarco, B. Naydenov, and F. Jelezko, *New J. Phys.* **16**, 093022 (2014).
- [116] P. London, P. Balasubramanian, B. Naydenov, L. P. McGuinness, and F. Jelezko, *Phys. Rev. A* **90**, 012302 (2014).
- [117] G. D. Fuchs, V. V. Dobrovitski, D. M. Toyli, F. J. Heremans, and D. D. Awschalom, *Sci.* **326**, 1520 (2009).
- [118] S. Ibáñez, Y.-C. Li, X. Chen, and J. G. Muga, *Phys. Rev. A* **92**, 062136 (2015).
- [119] S. Kuhr, W. Alt, D. Schrader, M. Müller, V. Gomer, and D. Meschede, *en, Sci.* **293**, 278 (2001).
- [120] J. Beugnon, C. Tuchendler, H. Marion, A. Gaëtan, Y. Miroshnychenko, Y. R. P. Sortais, A. M. Lance, M. P. A. Jones, G. Messin, A. Browaeys, and P. Grangier, *en, Nat. Phys.* **3**, 696 (2007).
- [121] C. Muldoon, L. Brandt, J. Dong, D. Stuart, E. Brainis, M. Himsworth, and A. Kuhn, *New J. Phys.* **14**, 073051 (2012).
- [122] A. Walther, F. Ziesel, T. Ruster, S. T. Dawkins, K. Ott, M. Hettrich, K. Singer, F. Schmidt-Kaler, and U. Poschinger, *Phys. Rev. Lett.* **109**, 080501 (2012).
- [123] R. Bowler, J. Gaebler, Y. Lin, T. R. Tan, D. Hanneke, J. D. Jost, J. P. Home, D. Leibfried, and D. J. Wineland, *Phys. Rev. Lett.* **109**, 080502 (2012).
- [124] M. Palmero, E. Torrontegui, D. Guéry-Odelin, and J. G. Muga, *Phys. Rev. A* **88**, 053423 (2013).

-
- [125] M. Palmero, R. Bowler, J. P. Gaebler, D. Leibfried, and J. G. Muga, *Phys. Rev. A* **90**, 053408 (2014).
- [126] N. Wu, A. Nanduri, and H. Rabitz, *Phys. Rev. B* **91**, 041115(R) (2015).
- [127] L. Allen and J. H. Eberly, *Optical resonance and two-level atoms* (Dover Publications, New York, USA, 1987).
- [128] A. Acín, I. Bloch, H. Buhrman, T. Calarco, C. Eichler, J. Eisert, D. Esteve, N. Gisin, S. J. Glaser, F. Jelezko, S. Kuhr, M. Lewenstein, M. F. Riedel, P. O. Schmidt, R. Thew, A. Wallraff, I. Walmsley, and F. K. Wilhelm, *New J. Phys.* **20**, 080201 (2018).
- [129] M. Abdelhafez, D. I. Schuster, and J. Koch, *Phys. Rev. A* **99**, 052327 (2019).
- [130] J. Kelly, R. Barends, B. Campbell, Y. Chen, Z. Chen, B. Chiaro, A. Dunsworth, A. G. Fowler, I.-C. Hoi, E. Jeffrey, A. Megrant, J. Mutus, C. Neill, P. J. J. O'Malley, C. Quintana, P. Roushan, D. Sank, A. Vainsencher, J. Wenner, T. C. White, A. N. Cleland, and J. M. Martinis, *Phys. Rev. Lett.* **112**, 240504 (2014).
- [131] S. Machnes, E. Assémat, D. Tannor, and F. K. Wilhelm, *Phys. Rev. Lett.* **120**, 150401 (2018).
- [132] C. Whitty, A. Kiely, and A. Ruschhaupt, *Phys. Rev. Research* **2**, 023360 (2020).
- [133] L. Qi, J. Chiaverini, H. Espinós, M. Palmero, and J. G. Muga, en, *EPL* **134**, 23001 (2021).
- [134] R. Gutiérrez-Jáuregui and A. Asenjo-García, *Phys. Rev. Research* **4**, 013080 (2022).

-
- [135] A. H. Karamlou, J. Braumüller, Y. Yanay, A. Di Paolo, P. M. Harrington, B. Kannan, D. Kim, M. Kjaergaard, A. Melville, S. Muschinske, B. M. Niedzielski, A. Vepsäläinen, R. Winik, J. L. Yoder, M. Schwartz, C. Tahan, T. P. Orlando, S. Gustavsson, and W. D. Oliver, *Npj Quantum Inf.* **8**, 1 (2022).
- [136] I. Bloch, J. Dalibard, and W. Zwerger, *Rev. Mod. Phys.* **80**, 885 (2008).
- [137] C. Schneider, M. Enderlein, T. Huber, and T. Schaetz, en, *Nat. Photonics* **4**, 772 (2010).
- [138] R. B. Linnet, I. D. Leroux, M. Marciante, A. Dantan, and M. Drewsen, *Phys. Rev. Lett.* **109**, 233005 (2012).
- [139] Q. Zhang, J. G. Muga, D. Guéry-Odelin, and X. Chen, en, *J. Phys. B: At. Mol. Opt. Phys.* **49**, 125503 (2016).
- [140] X.-J. Lu, A. Ruschhaupt, and J. G. Muga, *Phys. Rev. A* **97**, 053402 (2018).
- [141] X.-J. Lu, A. Ruschhaupt, S. Martínez-Garaot, and J. G. Muga, en, *Entropy* **22**, 262 (2020).
- [142] E. B. Davies, *Commun.Math. Phys.* **15**, 277 (1969).
- [143] E. B. Davies, *Commun.Math. Phys.* **19**, 83 (1970).
- [144] A. Kiely, *EPL* **134**, 10001 (2021).
- [145] T. Yu, L. Diósi, N. Gisin, and W. T. Strunz, *Phys. Rev. A* **60**, 91 (1999).
- [146] E. A. Novikov, *JTEP* **20**, 1290 (1965).
- [147] A. del Campo, J. Goold, and M. Paternostro, *Sci. Rep.* **4**, 6208 (2014).
- [148] A. del Campo, A. Chenu, S. Deng, and H. Wu, in *Thermodynamics in the quantum regime: Fundamental aspects and new directions*, edited by F. Binder, L. A. Correa, C. Gogolin, J. Anders, and G. Adesso (Springer International Publishing, Cham, 2018), pp. 127–148.

-
- [149] J. Li, T. Fogarty, S. Campbell, X. Chen, and T. Busch, *New J. Phys.* **20**, 015005 (2018).
- [150] K. Bergmann, N. V. Vitanov, and B. W. Shore, *J. Chem. Phys.* **142**, 170901 (2015).
- [151] S. Masuda and S. A. Rice, *J. Phys. Chem. A* **119**, 3479 (2015).
- [152] B. Juliá-Díaz, E. Torrontegui, J. Martorell, J. G. Muga, and A. Polls, *Phys. Rev. A* **86**, 063623 (2012).
- [153] A. Kiely and S. Campbell, *New J. Phys.* **23**, 033033 (2021).
- [154] S. Martínez-Garaot, E. Torrontegui, X. Chen, M. Modugno, D. Guéry-Odelin, S.-Y. Tseng, and J. G. Muga, *Phys. Rev. Lett.* **111**, 213001 (2013).
- [155] Y.-C. Li, X. Chen, J. G. Muga, and E. Y. Sherman, *New J. Phys.* **20**, 113029 (2018).
- [156] K. Takahashi, *Phys. Rev. A* **95**, 012309 (2017).
- [157] C. Whitty, A. Kiely, and A. Ruschhaupt, *Phys. Rev. A* **105**, 013311 (2022).
- [158] E. Torrontegui, X. Chen, M. Modugno, A. Ruschhaupt, D. Guéry-Odelin, and J. G. Muga, *Phys. Rev. A* **85**, 033605 (2012).
- [159] X.-J. Lu, X. Chen, J. Alonso, and J. G. Muga, *Phys. Rev. A* **89**, 023627 (2014).
- [160] J.-F. Schaff, X.-L. Song, P. Vignolo, and G. Labeyrie, *Phys. Rev. A* **82**, 033430 (2010).
- [161] S. Deng, A. Chenu, P. Diao, F. Li, S. Yu, I. Coulamy, A. del Campo, and H. Wu, *Sci. Adv.* **4**, eaar5909 (2018).
- [162] S. Masuda, K. Nakamura, and A. del Campo, *Phys. Rev. Lett.* **113**, 063003 (2014).

-
- [163] X. Zhou, S. Jin, and J. Schmiedmayer, *New J. Phys.* **20**, 055005 (2018).
- [164] R. A. Williams, J. D. Pillet, S. Al-Assam, B. Fletcher, M. Shotter, and C. J. Foot, *Opt. Express* **16**, 16977 (2008).
- [165] T. C. Li, H. Kelkar, D. Medellin, and M. G. Raizen, *Opt. Express* **16**, 5465 (2008).
- [166] J. Tao, Y. Wang, Y. He, and S. Wu, *Opt. Express* **26**, 14346 (2018).
- [167] S. Al-Assam, R. A. Williams, and C. J. Foot, *Phys. Rev. A* **82**, 021604 (2010).
- [168] L. Fallani, C. Fort, J. E. Lye, and M. Inguscio, *Opt. Express* **13**, 4303 (2005).
- [169] J. L. Ville, T. Bienaimé, R. Saint-Jalm, L. Corman, M. Aidelsburger, L. Chomaz, K. Kleinlein, D. Perconte, S. Nascimbène, J. Dalibard, and J. Beugnon, *Phys. Rev. A* **95**, 013632 (2017).
- [170] D. Kielpinski, C. Monroe, and D. J. Wineland, *Nature* **417**, 709 (2002).
- [171] Q. Zhang, X. Chen, and D. Guéry-Odelin, *Phys. Rev. A* **92**, 043410 (2015).
- [172] T. Hatomura, *J. Phys. Soc. Jpn.* **86**, 094002 (2017).
- [173] Y. Ban, X. Chen, E. Torrontegui, E. Solano, and J. Casanova, *Sci. Rep.* **11**, 5783 (2021).
- [174] M. Okuyama and K. Takahashi, *J. Phys. Soc. Jpn.* **86**, 043002 (2017).